CNWRA *A center of excellence in earth sciences and engineering*

A Division of Southwest Research Institute®
6220 Culebra Road • San Antonio, Texas, U.S.A. 78228-5166
(210) 522-5160 • Fax (210) 522-5155

August 28, 2003
Contract No. NRC–02–02–012
Account No. 20.06002.01.091

U.S. Nuclear Regulatory Commission
ATTN: Mr. Jeffrey Pohle
Division of Waste Management
TWFN, Mail Stop 7-D13
Washington, DC 20555

SUBJECT: Thermal Effects on Flow KTI Intermediate Milestone 06002.01.091.330: Approach for and Status of Evaluating Model/Parameter Uncertainty—Letter Report

Dear Mr. Pohle:

Enclosed please find the report titled "Status Report for Multiphase Numerical Simulation." This technical document fulfills the requirements for the subject milestone, which is due August 29, 2003.

As agreed with you, the scope of this report is limited to presenting results of two sets of sensitivity analyses performed on heater experiments conducted at different scales (laboratory and field). Interpretations of the results provide insights into which properties and conceptual models are most appropriate for representing heat and mass transfer through partially saturated fractured porous media. The laboratory-scale analyses highlight the importance of assigning appropriate property values to several key parameters. The choice of conceptual model for matrix-fracture interactions had an important effect on evolution of temperature and saturation in the laboratory-scale test; however, all conceptual models that were examined had some success in capturing key features observed during the tests. Analyses of the field-scale test provided greater insight on the choice of the matrix-fracture interaction conceptual model. Finally, both sets of sensitivity analyses confirmed that partial success, in terms of agreement between selected observations and model results, could be achieved for almost any choice of property values or conceptual model.

If you have any questions, please contact Ronald Green at 210-522-5305 or me at 210-522-5151.

Sincerely yours,

Asadul H. Chowdhury, Manager
Mining, Geotechnical, and Facility Engineering

AHC/ph
Enclosure
cc:

D. DeMarco	K. Stablein	B. Jagannath	W. Patrick	Record Copy B, IQS
B. Meehan	D. Brooks	J. Firth	B. Sagar	Letter only:
E. Whitt	T. McCartin	J. Peckenpaugh	R. Fedors	M. Leach
W. Reamer	P. Justus	D. Esh	S. Painter	CNWRA Directors
L. Campbell	J. Greeves	R. Codell	C. Manepally	CNWRA Element Mgrs.
A. Campbell	J. Danna	G. Hatchett	G. Walter	P. Maldonado
J. Bradbury	M. Nataraja	T. Kobetz		
J. Schlueter				

Washington Office • Twinbrook Metro Plaza #210
12300 Twinbrook Parkway • Rockville, Maryland 20852-1606

STATUS REPORT FOR MULTIPHASE NUMERICAL SIMULATION

Prepared for

U.S. Nuclear Regulatory Commission
Contract NRC–02–02–012

Prepared by

R. Green
S. Painter
B. Fratesi
C. Manepally
G. Walter

Center for Nuclear Waste Regulatory Analyses
San Antonio, Texas

August 2003

CONTENTS

Section			Page
FIGURES			v
TABLES			ix
ACKNOWLEDGMENTS			xi
EXECUTIVE SUMMARY			xiii
1	INTRODUCTION		1-1
	1.1	Background	1-1
	1.2	Objective and Scope	1-1
	1.3	Technical Agreements	1-2
2	MATHEMATICAL SETTING		2-1
	2.1	Formulation of Dual Continua Model	2-2
	2.2	Relative Permeability Functions	2-3
	2.3	Active Fracture Model	2-5
	2.4	Summary of Options for Modifying Matrix-Fracture Interaction	2-6
3	NUMERICAL SOLUTION		3-1
4	EXPERIMENTAL TEST RESULTS		4-1
	4.1	Laboratory-Scale Heater Test	4-1
	4.2	Drift-Scale Heater Test	4-2
5	NUMERICAL MODEL DEVELOPMENT		5-1
	5.1	Laboratory-Scale Heater Test	5-1
	5.2	Drift-Scale Heater Test	5-1
6	MODEL RESULTS		6-1
	6.1	Laboratory-Scale Heater Test Model Results	6-1
	6.2	Drift-Scale Heater Test Model Results	6-6
7	DISCUSSION		7-1
	7.1	Laboratory-Scale Experiment	7-1
	7.2	Field-Scale Experiment	7-2
	7.3	General Conclusions	7-2
	7.4	Future Analyses	7-3
8	REFERENCES		8-1
APPENDIX A			
APPENDIX B			
APPENDIX C			
APPENDIX D			
APPENDIX E			
APPENDIX F			
APPENDIX G			

FIGURES

Figure		Page
4-1	Laboratory-Scale Experiment Schematic	4-2
4-2	Schematic of Laboratory-Scale Experiment Drift	4-2
4-3	Thermocouple Locations in Test 1 (a) and Test 2 (b) of the Laboratory-Scale Experiment	4-4
4-4	Measured Laboratory-Scale Experiment Temperatures for the Matrix Continuum, Perpendicular (A) and Parallel (B) to the Heated Drift	4-5
4-5	Saturation Measured at the Mid-Plane (Left) and Edge Plane (Right) of the Laboratory-Scale Experiment	4-6
4-6	Location of the Exploratory Studies Facility Drift-Scale Heater Experiment	4-7
4-7	Plan-View Layout of Principal Components of the Drift-Scale Heater Test	4-8
5-1	Numerical Grid for the Laboratory-Scale Heater Test	5-2
5-2	Numerical Grid for the Drift-Scale Heater Test	5-3
5-3	Close-Up View of the Numerical Grid for the Drift-Scale Heater Test	5-3
5-4	Drift-Scale Heater Test Heat Loads for the Canisters (a) and Wing Heaters (b)	5-7
6-1	Simulated Laboratory-Scale Experiment Temperatures for the Matrix Continuum, Perpendicular to the Heated Drift	6-6
6-2	Simulated Laboratory-Scale Experiment Temperatures for the Matrix Continuum, Parallel to the Heated Drift	6-6
6-3	Simulated Matrix Saturation for the Mid-Plane (Left) and Edge Plane (Right) of the Laboratory-Scale Experiment with the Active Fracture Model and $\gamma = 0.4$ (lst156)	6-7
6-4	Simulated Matrix Saturation for the Mid-Plane (Left) and Edge Plane (Right) of the Laboratory-Scale Experiment with Reduced Fracture Relative Permeability	6-7
6-5	Simulated Matrix Saturation for the Mid-Plane (Left) and Edge Plane (Right) of the Laboratory-Scale Experiment with Area Modifier, $A_{mod} = 0.01$ (lst163)	6-8
6-6	Simulated Matrix Saturation for the Mid-Plane (Left) and Edge Plane (Right) of the Laboratory-Scale Experiment with Area Modifier, $A_{mod} = 0.01$ (lst157)	6-8
6-7	Simulated Matrix Saturation for the Mid-Plane (Left) and Edge Plane (Right) of the Laboratory-Scale Experiment with Area Modifier, $A_{mod} = 0.1$ (lst162)	6-9
6-8	Simulated Matrix Saturation for the Mid-Plane (Left) and Edge Plane (Right) of the Laboratory-Scale Experiment with Matrix Permeability Decreased by 10 Times	6-9
6-9	Simulated Matrix Saturation for the Mid-Plane (Left) and Edge Plane (Right) of the Laboratory-Scale Experiment with A = 0.001	6-11
6-10	Simulated Matrix Saturation for the Mid-Plane (Left) and Edge Plane (Right) of the Laboratory-Scale Experiment with an Active Fracture Model, the van Genuchten α	6-11
6-11	Simulated Matrix Saturation for the Mid-Plane (Left) and Edge Plane (Right) of the Laboratory-Scale Experiment with No Active Fracture Model (lst173)	6-12
6-12	Simulated Matrix Saturation for the Mid-Plane (Left) and Edge Plane (Right) of the Laboratory-Scale Experiment with No Active Fracture Model and Fracture	6-12
6-13	Simulated Fracture Saturation for the Laboratory-Scale Experiment at Four Planes Located at 0.01, 0.15, 0.23, and 0.25 m (Left to Right)...(lst184)	6-13

FIGURES (continued)

Figure		Page
6-14	Simulated Fracture Saturation for the Laboratory-Scale Experiment at Four Planes Located at 0.01, 0.15, 0.23, and 0.25 m (Left to Right)...(lst176)	6-13
6-15	Simulated Fracture Saturation for the Laboratory-Scale Experiment at Four Planes Located at 0.01, 0.15, 0.23, and 0.25 m (Left to Right)...(lst163)	6-14
6-16	Simulated Matrix Saturations for the Field-Scale Experiment Site Under Ambient Conditions	6-17
6-17	Contour Plot of Simulated Matrix Temperature for the Field-Scale Experiment After 3 Months (Top), I Year (Middle), and 4 Years (Bottom) of Heating	6-21
6-18	Contour Plot of Simulated Matrix Temperature for the Field-Scale Experiment with A_{mod} = 0.001 (ds127)	6-22
6-19	Contour Plot of Simulated Matrix Saturation for the Field-Scale Experiment with Drift-Wall Heat Source Reduced by 30 Percent (ds112)	6-23
6-20	Contour Plot of Simulated Matrix Saturation for the Field-Scale Experiment with the van Genuchten α Decreased by 10 Times (ds124)	6-24
6-21	Contour Plot of Simulated Matrix Saturation for the Field-Scale Experiment with Matrix Permeability Increased by 10 Times (ds113)	6-25
6-22	Contour Plot of Simulated Matrix Saturation for the Field-Scale Experiment with Thermal Conductivity Decreased by 20 Percent (ds118)	6-27
6-23	Contour Plot of Simulated Matrix Saturation for the Field-Scale Experiment with A_{mod} = 0.1 (ds123)	6-28
6-24	Contour Plot of Simulated Fracture Saturation for the Field-Scale Experiment with Fracture Permeability Decreased by 100 Times	6-29
6-25	Contour Plot of Simulated Fracture Saturation for the Field-Scale Experiment with Fracture Permeability Decreased by 10 Times	6-30
6-26	Contour Plot of Simulated Fracture Saturation for the Field-Scale Experiment with Matrix Permeability Increased by 10 Times (ds113)	6-31
6-27	Contour Plot of Simulated Fracture Saturation for the Field-Scale Experiment with Thermal Conductivity Decreased by 10 Times (ds118)	6-32
6-28	Contour Plot of Simulated Fracture Saturation for the Field-Scale Experiment with the Active Fracture Model γ = 0.6 (ds121)	6-33
6-29	Contour Plot of Simulated Fracture Saturation for the Field-Scale Experiment with the Active Fracture Model γ = 0.8 (ds122)	6-34
6-30	Contour Plot of Simulated Fracture Saturation for the Field-Scale Experiment with the van Genuchten α Decreased by 10 Times (ds124)	6-35
6-31	Contour Plot of Simulated Fracture Saturation for the Field-Scale Experiment with the Active Fracture Model γ = 0.2 (ds120)	6-36
6-32	Contour Plot of Simulated Fracture Saturation for the Field-Scale Experiment with the Area Modifier A_{mod} = 0.01 (ds126)	6-37
6-33	Contour Plot of Simulated Fracture Saturation for the Field-Scale Experiment with the Area Modifier A_{mod} = 0.001 (ds127)	6-38
6-34	Comparison of Measured Temperature Versus Simulated Matrix Temperature...for the Basecase (ds108)	6-39
6-35	Comparison of Measured Temperature Versus Simulated Matrix Temperature...with Drift-Wall Heat Load Decreased by 10 Percent (ds110)	6-41

FIGURES (continued)

Figure		Page
6-36	Comparison of Measured Temperature Versus Simulated Matrix Temperature...with Drift-Wall Heat Load Decreased by 20 Percent (ds111)	6-42
6-37	Comparison of Measured Temperature Versus Simulated Matrix Temperature...with Drift-Wall Heat Load Decreased by 30 Percent (ds112)	6-43
6-38	Comparison of Measured Temperature Versus Simulated Matrix Temperature...with Fracture Permeability Decreased by 10 Times (ds115)	6-44
6-39	Comparison of Measured Temperature Versus Simulated Matrix Temperature...with Area Modifier A_{mod} = 0.001 (dsl127)	6-46
7-1	Contour Plots of Simulated Matrix Saturation	7-3
7-2	Contour Plots of Simulated Fracture Saturation	7-4

TABLES

Table		Page
3-1	Choice of Primary Variable for Different Fluid States	3-1
4-1	Evolution of Property Values for the Hydrostratigraphic Units at the Drift-Scale Heater Test	4-10
5-1	Basecase Property Values for Laboratory-Scale Model	5-4
5-2	Basecase Property Values for Field-Scale Model	5-5
6-1	Parameter Varied During the Laboratory-Scale Experiment Heating Phase Sensitivity Analyses	6-3
6-2	Summary of Laboratory-Scale Simulations Indicating Variables Modified from Basecase Values	6-3
6-3	Summary of Laboratory-Scale Experiment Sensitivity Analyses: Maximum Matrix and Fracture Saturation and Temperature	6-5
6-4	Intrinsic Fracture Permeability Values	6-15
6-5	Field-Scale Experiment Ambient Conditions Sensitivity Analyses	6-15
6-6	Parameter Varied During the Field-Scale Experiment Heating Phase Sensitivity Analyses	6-19
6-7	Summary of Variables Examined in the Field-Scale Model Sensitivity Analyses	6-19
6-8	Maximum Temperature, Fracture Saturation, and Matrix Saturation Observed During Simulations of the Field-Scale Experiment	6-20

ACKNOWLEDGMENTS

This report documents work performed by the Center for Nuclear Waste Regulatory Analyses (CNWRA) for the U.S. Nuclear Regulatory Commission (NRC) under Contract No. NRC–02–02–012. The activities reported here were performed on behalf of the NRC Office of Nuclear Material Safety and Safeguards, Division of Waste Management. The report is an independent product of the CNWRA and does not necessarily reflect the view or regulatory position of the NRC.

The authors thank D. Farrell and B. Sagar for technical and programmatic reviews of this document. The authors are thankful to P. Houston and R. Mantooth for typing the report and to C. Cudd, J. Pryor, and B. Long for providing a full range of editorial services in preparation of the final document.

QUALITY OF DATA, ANALYSES, AND COMPUTER CODES

DATA: No CNWRA-generated original data are contained in this report.

ANALYSES AND CODES: MULTIFLO code Version 1.5.2 (Lichtner and Seth, 1996; Painter, et al., 2001) software developed under CNWRA quality assurance procedures was used in all analyses reported in this document.

References:

Lichtner, P.C. and M.S. Seth. "Multiphase-Multicomponent Nonisothermal Reactive Transport in Partially Saturated Porous Media." Proceedings of the International Conference on Deep Geological Disposal of Radioactive Waste, Winnipeg, Manitoba, Canada, September 16–19, 1996. Toronto, Ontario, Canada: Canadian Nuclear Society. 1996. pp. 133–142.

Painter, S., P.C. Lichtner, and M.S. Seth. "MULTIFLO User's Manual." MULTIFLO, Version 1.5: Two-Phase Nonisothermal Coupled Thermal-Hydrologic-Chemical Flow Simulator. Rev. 3. San Antonio, Texas: CNWRA. 2001.

EXECUTIVE SUMMARY

Numerical simulation of multiphase heat and mass transfer will be an important component to demonstrate the performance of the proposed geologic high-level waste repository at Yucca Mountain, Nevada. Significant progress has been achieved in multiphase modeling of heat and mass transfer through partially saturated fractured rock during the past 25 years. There is still much uncertainty in modeling results because of the high level of complexity in the coupled multiphase heat and transport processes. Various numerical codes have been used to evaluate conceptual models and property value assignments for heat and mass transfer through partially saturated rock representative of Yucca Mountain. Although similarities exist in the conceptual models employed by each numerical code and in the databases on which the models are constructed, the variety of numerical codes, conceptual models, boundary condition prescription, and property assignment provides a wide range in simulation outcomes.

Difficulties arise when attempting to rigorously evaluate simulation results generated by different numerical codes. Contemporary quality assurance practices applied to numerical models typically entail comparing model simulations with analytical solutions. Unfortunately, analytical solutions can address only simple geometries with limited heterogenieties and limited physical process coupling. To assess the numerical codes further, a common practice is to compare, or benchmark, simulation results from different models for controlled tests. Controlled tests are desirable for the benchmark process because boundary conditions can be established and measured, property values can be reasonably determined, and the dominating physical processes can be limited and controlled to some extent. Historically, laboratory- and field-scale experiments have been used in this process.

This report documents analyses conducted by the Center for Nuclear Waste Regulatory Analyses (CNWRA) to evaluate conceptual models and key property value assignments in numerical models used to simulate heat and mass transfer processes expected at the proposed Yucca Mountain repository. MULTIFLO code Version 1.5.2 (Lichtner and Seth, 1996; Painter, et al., 2001) was used to perform all simulations. Results from two experiments have been used to make the assessments. One experiment was conducted at laboratory scale by CNWRA staff and the other was conducted by the U.S. Department of Energy at the field scale at the Exploratory Studies Facility at Yucca Mountain.

The objective of this study is to evaluate the importance and effects of conceptual model selection, boundary condition prescription, and property value assignment. Not all conceptual models, boundary conditions, or property value assignments are evaluated in this study. Past studies (Green and Painter, 2002a,b; Green, et al., 2001) have helped identify those conceptual models and property values whose selection has a potentially large impact on multiphase simulation results. A dual continua conceptual model (consisting of matrix and fracture continua) evaluated during these earlier evaluations has been accepted as appropriate and is incorporated in all simulations. Conceptual models addressed during the study considered a variety of approaches to implement matrix-fracture interactions. Properties whose values were varied include the air entry value for the fracture continuum (i.e., the van Genuchten α), fracture intrinsic permeability and porosity, matrix permeability, the active fracture model γ, and the matrix-fracture area modification value. Not all model factors evaluated at one scale (i.e., either laboratory or field) were evaluated at the other scale.

The laboratory-scale experiment was, in some ways, better characterized and controlled than the field-scale experiment. For example, the matrix and system of fractures of the laboratory-scale test medium were more uniform and better characterized than the field site. Boundary conditions for the laboratory-scale test were controlled (i.e., infiltration rate was known); however, the limited size of the laboratory-scale test resulted in heat loss through the side walls of the test cell that resulted in somewhat serious modeling uncertainty. Sensitivity modeling analyses helped minimize this uncertainty, however, complete characterization of the test cell thermal boundary conditions was not possible.

Examination of the laboratory-scale sensitivity analyses results indicated that selection of different parameter values and conceptual models captured different features observed during the laboratory-scale experimental results. Key features observed during the laboratory-scale experiment were (i) zones of high matrix saturation above and low matrix saturation below the heated drift at both the mid-plane and the edge plane of the test cell, (ii) focused flow through fracture continuum, and (iii) penetration of fracture flow into the crown of the heated drift. The results of simulations of the laboratory-scale experiment indicated that improved simulation of these features was achieved with a smaller van Genuchten α ($1.0 \times 10^{-4}\,Pa^{-1}$), decreased matrix permeability, possible increased fracture permeability, and a reduction in matrix-fracture interactions, although a specific matrix-fracture interaction conceptual model was not clearly identified. A possible exception to this broadly defined model was the successful simulation of decreased saturation below the heated drift, which was replicated in simulations with larger values for the fracture van Genuchten α parameter ($1.0 \times 10^{-3}\,Pa^{-1}$).

Some of the best discriminating evidence of heat and mass transfer observed during the laboratory-scale experiment were the unambiguous zones of increased saturation above and decreased saturation below the heated drift. The models that captured both these features were (i) active fracture model with large van Genuchten α and matrix permeability decreased by 10 times, (ii) large van Genuchten α with A_{mod} set to 0.001, and (iii) matrix permeability decreased by 10 times relative to the measured basecase values.

Temperatures measured during the field-scale experiment provided clearer evidence of the evolution of the thermal-hydrological regime than did indirect measurements of saturation. Nonetheless, as demonstrated in this study, multiple different conceptual models frequently can replicate temperature profiles; however, matching saturation is significantly more challenging. The field-scale basecase model consisted of infiltration at 3.0 mm/yr [0.12 in/yr], the active fracture model (Liu, et al., 1998) with $\gamma = 0.41$, and the property values provided in CRWMS M&O (2000b). Based on replication of temperatures measured at three boreholes (158, 160, and 162), the basecase simulation with a canister heat load reduced by 30 percent applied to the drift wall provided the best match. This simulation did not capture all salient features in the measured temperatures. In particular, simulated temperatures closest to the drift did not reflect all features exhibited in the measured temperatures. Additional adjustment of the canister heat load could reduce these differences. Also, a heat pipe simulated above the drift wall (Borehole 158) after 4 years of heating was not seen in the measured data. Simulation results indicated that zones of increased saturation form in the fracture continuum below the outer wing heaters by 3 months. By 1 year of heating, these zones increased in size and were found above and below the wing heaters. Further, a prominent dryout zone developed encompassing the combined drift-wing heater region. In addition, a prominent zone of increased fracture saturation formed beneath the full footprint of the field-scale experiment after 1 year of heating.

General observations can be drawn from the ensemble of sensitivity analyses for the two experiments conducted at different scales. The laboratory-scale analyses highlight the importance of assigning appropriate property values to several key parameters: matrix permeability, the fracture van Genuchten α (related to the air-entry value), and, most importantly, fracture permeability. The choice of conceptual model for matrix-fracture interactions had an important effect on evolution of temperature and saturation in the laboratory-scale test. However, all three choices for conceptual models had some success in capturing key features observed during the tests. Analyses of the field-scale test provided greater insight on the choice of the conceptual model for matrix-fracture interaction. Replication of temperatures measured at three boreholes was most successful when the active fracture conceptual model was selected. Finally, both sets of sensitivity analyses confirmed that partial success, in terms of agreement between selected observations and model results, could be achieved for almost any choice of property values or conceptual model. It is important to compare the model results with the complete suite of experimental results to determine the true merit of the values and conceptual models selected for representative multiphase models.

References:

CRWMS M&O. "Calibrated Properties Model." MDL–NBS–HS–000003. Rev. 00. Las Vegas, Nevada: CRWMS M&O. 2000.

Green, R.T., M.E. Hill, and S. Painter. "Progress Report for DECOVALEX III Task 2: Numerical Simulation of the Drift-Scale Heater Test at Yucca Mountain." San Antonio, Texas: CNWRA. 2001.

Green, R.T. and S. Painter. "Final Report for DECOVALEX III Task 2A: Numerical Simulation of the Drift-Scale Heater Test at Yucca Mountain." San Antonio, Texas: CNWRA. 2002a

Green, R.T. and S. Painter. "Status Report for Numerical Simulation of the Drift-Scale Heater Test at Yucca Mountain." San Antonio, Texas: CNWRA. 2002b

Lichtner, P.C. and M.S. Seth. "Multiphase-Multicomponent Nonisothermal Reactive Transport in Partially Saturated Porous Media." Proceedings of the International Conference on Deep Geological Disposal of Radioactive Waste, Winnipeg, Manitoba, Canada, September 16–19, 1996. Toronto, Ontario, Canada: Canadian Nuclear Society. 1996. pp. 133–142.

Liu, H.H., C. Doughty, and G.S. Bodvarsson. "An Active Fracture Model for Unsaturated Flow and Transport in Fractured Rock." *Water Resources Research.* Vol. 34, No. 10. pp. 633–2,646. 1998.

Painter, S., P.C. Lichtner, and M.S. Seth. "MULTIFLO User's Manual." MULTIFLO, Version 1.5: Two-Phase Nonisothermal Coupled Thermal-Hydrologic-Chemical Flow Simulator. Rev. 3. San Antonio, Texas: CNWRA. 2001.

1 INTRODUCTION

1.1 Background

Numerical simulation of multiphase heat and mass transfer will be an important components to demonstrate the performance of the proposed geologic high-level waste repository at Yucca Mountain, Nevada. Significant progress has been achieved in multiphase modeling of heat and mass transport through partially saturated fractured rock during the past 25 years. Uncertainty remains in modeling results for the Yucca Mountain site, however, because of the high level of complexity in the coupled multiphase heat and transport processes.

Numerical codes (or variations of the codes) frequently used for Yucca Mountain related multiphase analyses are TOUGH2 (Pruess, et al., 1999), NUFT (Nitao, 1998), FEHM (Zyvolowski, et al.,1999), and MULTIFLO (Lichtner and Seth, 1996; Painter, et al., 2001). However, due to the complexity of these codes, those groups conducting multiphase modeling of Yucca Mountain typically use only one of the available codes for their analyses. These codes have been used to evaluate various conceptual models and property value assignments for modeling heat and mass transfer through partially saturated rock. Similarities exist in the conceptual models employed by each numerical code and in the databases upon which the models are constructed.

Difficulties arise when attempting to rigorously evaluate simulation results generated by different numerical codes. Contemporary quality assurance practices applied to numerical models typically entail comparing model simulations with analytical solutions. Unfortunately, analytical solutions can address only simple geometries with limited physical process couplings. To assess the numerical codes further, a common practice is to compare, or benchmark, simulation results from different models developed for controlled tests. Controlled tests are desirable for the benchmark process because boundary conditions can be established and measured, property values can be reasonably determined, and the dominating physical processes can be limited and controlled to some extent. Historically, laboratory- and field-scale experiments have been used in this process.

1.2 Objective and Scope

This report documents analyses conducted by the Center for Nuclear Waste Regulatory Analyses (CNWRA) to evaluate conceptual models and key property value assignments in numerical models used to simulate heat and mass transfer processes expected at the proposed Yucca Mountain repository. MULTIFLO code Version 1.5.2 (Lichtner and Seth, 1996; Painter, et al., 2001) was used to perform all simulations. Results from two experiments have been used to make the assessments. One experiment was conducted at laboratory scale by CNWRA staff and one was conducted by the U.S. Department of Energy (DOE) at the Exploratory Studies Facility at Yucca Mountain. The laboratory-scale experiment consists of two tests: the first of 4 months and the second of 7 months. The field-scale experiment at the Exploratory Studies Facility is the Drift-Scale Heater Test. The Drift-Scale Heater Test consists of a 4-year heating phase followed by a 4-year cooling phase. The heating phase is complete. The cooling phase started in January 2002.

The objective of this study is to evaluate the importance and effect of conceptual model selection, boundary condition prescription, and property value assignment. Past studies (Green and Painter, 2002a,b; Green, et al., 2001) has helped identify those conceptual models and property values whose selection have a potentially significant impact on multiphase model simulation results. A dual continua conceptual model (consisting of matrix and fracture continua) evaluated during these earlier studies has been accepted as appropriate and incorporated in all simulations.

Conceptual models addressed during this study considered a variety of approaches to implement an active fracture model that is an inherent attribute of dual continua models. Properties whose value assignments were varied include the air entry value for the fracture continuum (i.e., the van Genuchten α), fracture intrinsic permeability and porosity, matrix permeability, the active fracture model γ, fracture relative permeability factor γ, the area modification value, and thermal conductivity. These parameters were chosen for analysis, in part, because they are not directly measurable. The active fracture model, the fracture relative permeability factor, and the area modification factor, are different conceptual models used to specify matrix-fracture interactions. Not all model factors evaluated at one scale (i.e., either laboratory or field) were evaluated at the other scale. For example, infiltration at the surface boundary was varied only for the field-scale test. Results from these analyses provide greater insight into identifying those factors that have potentially significant effects on the simulations.

1.3 Technical Agreements

DOE is conducting the Drift-Scale Heater Test to provide insight on heat and mass transfer processes through fractured porous media. Two DOE and U.S. Nuclear Regulatory Commission (NRC) technical agreements were generated on the topic of the bulkhead losses in the Drift-Scale Heater Test and model uncertainty. Bulkhead losses and model uncertainty are evaluated in this study.

Agreement TEF.2.01: "Consider measuring losses of mass and energy through the bulkhead of the drift-scale heater test and provide the technical basis for any decision or method decided upon (include the intended use of the results of the drift-scale heater test such as verifying assumptions in FEP exclusion arguments or providing support for TSPA models). The DOE should analyze uncertainty in the fate of thermally mobilized water in the drift-scale heater test and evaluate the effect this uncertainty has on conclusions drawn from the drift-scale heater test results. The DOE position is that measuring mass and energy losses through the bulkhead of the drift-scale heater test is not necessary for the intended use of the drift-scale heater test results. The drift-scale heater test results are intended for validation of models of thermally-driven coupled processes in the rock, and measurements are not directly incorporated into TSPA models. Results of the last two years of data support the validation of drift-scale heater test coupled-process models and the current treatment of mass and energy loss through the bulkhead. The DOE will provide the NRC a white paper on the technical basis for the DOE understanding of heat and mass losses through the bulkhead and their effects on the results by April 2001. This white paper will include the DOE technical basis for its decision regarding measurements of heat and mass losses through the drift-scale heater test bulkhead. This white paper will address uncertainty in the fate of thermally mobilized water in the drift-scale heater test and also the effect this uncertainty has on conclusions drawn from the drift-scale heater test

results. The NRC will provide comments on this white paper. The DOE will provide analyses of the effects of this uncertainty on the uses of the drift-scale heater test in response to NRC comments."

The Drift-Scale Heater Test results were to be used to validate models of thermally-driven coupled processes in the rock. However, the unmonitored neat and mass loss through the bulkhead led to concern by NRC on how the Drift-Scale Heater Test results could be used to support a license application. DOE agreed in a teleconference prior to the NRC letter of March 11, 2003,[1] that parameter values from the Drift-Scale Heater Test could not be used to develop parameter values for other hydrological or thermohydrological models in the unsaturated zone. Furthermore, DOE agreed in the teleconference that the Drift-Scale Heater Test cannot be used as support for the conclusion that no water will seep into drifts. DOE noted that it was evaluating reasonableness of the Phillips (1996) solution for preferential flow breaching the dryout zone and will present results to support completion of TEF.2.08.

Thus, DOE does not have any measurements or experiments to support its conclusion that water will not preferentially breach the dryout zone, nor any supporting data for its matrix-fracture interaction characterization under nonisothermal conditions. Without measurements or supporting model results, evaluating the uncertainty of the DOE thermo-hydrological models takes on a larger emphasis.

Agreement TEF.2.12: "Provide the Unsaturated Zone Flow and Transport PMR, Rev. 00, ICN 02, documenting the resolution of issues on page 5 of the OI 8 presentation. The DOE will provide the Unsaturated Zone Flow and Transport PMR (TDR–NBS–HS–000002) Rev. 00 ICN 02 to the NRC in February 2001. It should be noted, however, that not all of the items listed on page 5 of the DOE's Open Item 8 presentation at this meeting are included in that revision. The DOE will include all the items listed on page 5 of the DOE's Open Item 8 presentation in Rev. 02 of the Unsaturated Zone Flow and Transport PMR, scheduled to be available in FY2002."

The primary focus of this agreement is model uncertainty in process models used to support other process models and to support the Total System Performance Assessment Model. In particular for Agreement TEF.2.12, DOE was to consider model uncertainty including (i) types of model uncertainty, (ii) flow conceptualization in ambient conditions, (iii) flow conceptualization inthermal conditions, (iv) fracture flow in ambient and thermal conditions, (v) matrix-fracture interaction model evolution, (vi) discrete fracture description, and (vii) reduction of model uncertainty. Agreement TEF.2.12 is not considered complete.

[1]Schlueter, J.R. "Thermal Effects on Flow Agreement 2.01; Status: Complete." Letter (March 11) to J.D. Ziegler, Office of License Application and Strategy, DOE. Washington, DC: NRC. 2003.

2 MATHEMATICAL SETTING

MULTIFLO code Version 1.5.2 (Lichtner and Seth, 1996; Painter, et al., 2001) was used in the analyses reported in this document. MULTIFLO is a general code for simulating multiphase, multicomponent, transport processes in nonisothermal systems with chemical reactions and phase changes.

The MULTIFLO code consists of two sequentially coupled submodules: Mass and Energy Transport (METRA) and General Electrochemical Migration (GEM). METRA solves mass balance equations for water and air, as well as, an energy balance equation. GEM solves mass balance equations for multicomponent reactive transport of solute species. Only transport of air, water, and heat was simulated in these analyses; therefore, only the METRA submodule was used in these analyses.

METRA represents multiphase flow through three dimensions, although zero, one, or two dimensions are also possible. Single-phase (i.e., all liquid or all gas) or two-phase systems can be simulated. The equation of state for water in METRA allows temperatures in the 1–800 °C [33–1,472 °F] range and pressures below 165 bars. A complete description of the mathematical basis for METRA is found in Painter, et al., 2001. The code will be referred to as MULTIFLO in this document for convenience.

MULTIFLO incorporates a dual continua conceptual model with the matrix and the fractures as the two continua. The dual continua model formulation is similar to the dual permeability model formulation used in recent U.S. Department of Energy (DOE) numerical simulations (CRWMS M&O, 2000c). Differences between the two conceptualizations vary, depending upon the specific manner in which each model is implemented. The dual continua model and dual permeability model conceptualizations provide separate continua for the matrix and the fractures. The two continua are coupled throughout the model domain by functions for the transfer of mass and heat between the fractures and matrix. Use of a dual continua model increases the complexity of the numerical model used in the simulations, but offers the potential to realistically partition flow between matrix and fractures.

Different conceptual models are available for heat and mass transfer between the matrix and fracture continua. In the first option, this transfer is modified by reducing the interfacial area between the matrix and fracture continua. Both heat and mass transfer are affected when this option is invoked. Heat transfer is not modified in the other two options. In the second option, a constant reduction factor is applied to the relative permeability function that describes fracture-to-matrix flow. The active fracture model by Liu, et al. (1998), is the third option. In the second and third options, only the liquid flow from fractures to matrix is affected; gas and heat flows are unaffected as are all flows from the matrix to the fractures.

The following sections summarize the development of matrix-fracture approaches in MULTIFLO. The use of different relative permeability functions for fracture-to-matrix flow, combined with an interfacial modification factor provides considerable flexibility to test different conceptualizations of matrix-fracture interaction. Formulation of relative permeability is included because it provides the foundation for the active fracture model.

2.1 Formulation of Dual Continua Model

Matrix block size is a key parameter in formulation of the dual continua model. Fracture-matrix distances (in each dimension) are related, but not equivalent, to model block dimensions. The model block dimension, d, is the distance between the center of the matrix block and the center of the fracture defining the edge of the model block. For the case where the element is a cube, $d = l/2 + \delta/2$ where l is the length of the matrix block and δ is the fracture aperture. Fracture aperture is calculated using model block size, matrix block size, and fracture porosity. Model block size directly affects two model properties: (i) the interfacial area between the matrix and fracture continua in a dual continua model and (ii) the gradients that drive heat and mass between the two continua. In particular, increasing model block size reduces the specific area available for heat and mass transfer between the matrix and fracture continua and increases the distance in which changes in pressure and temperature occur, thereby reducing their respective gradients.

The specific interfacial area (area per unit volume) between the two continua, A_{fm}, is defined using matrix block dimensions, l_i, where $i = x$, y, and z. For two dimensions, the specific interfacial area is defined by (Lichtner and Seth, 1996; Painter, et al., 2001).

$$A_{fm} = 2(1-\varepsilon_f)\left[\frac{1}{l_x}+\frac{1}{l_z}\right] \tag{2-1}$$

which, for a cubic block geometry in two dimensions (i.e., $l_x = l_z$), becomes

$$A_{fm} = 4\left(\frac{1-\varepsilon_f}{l}\right) \tag{2-2}$$

where ε_f is fracture porosity. MULTIFLO provides an option to reduce the interaction between the matrix and fracture by reducing the specific interfacial area. This modification is incorporated using a dimensionless area modification factor, A_{mod}, to allow a reduction, but not an increase, in the interfacial area between the matrix and fracture continua.

In the MULTIFLO implementation of the dual continua model, the relative permeability functions for flow from matrix to the fractures may be specified independently from the relative permeability for the fracture continuum. When $P_{lm} > P_{lf}$, liquid flow is from the matrix to the fracture continuum and is modeled as

$$q_l = \frac{k_{\text{harmonic}} k_{rl,m\rightarrow f}}{\mu_l} \frac{P_{lm} - P_{lf}}{d} \tag{2-3}$$

where q is flux, P is pressure, μ is viscosity, and the m, f, l, and r subscripts denote matrix, fracture, liquid, and relative. Liquid-phase relative permeability, k_{rl}, is taken to be the upstream

value in this case. For $P_{lm} > P_{lf}$, the upstream value is for the matrix. Fracture permeability is expressed as intrinsic. The harmonic mean for liquid permeability is expressed as

$$k_{harmonic} = \frac{(1+\delta)k_f\, k_m}{1k_f + \delta k_m} \tag{2-4}$$

For $P_{lf} > P_{lm}$, liquid flow is from the fracture to the matrix and is defined by

$$q_l = \frac{k_{\text{harmonic}} k_{rl,f\to m}}{\mu_l} \frac{P_{lf} - P_{lm}}{d} \tag{2-5}$$

where $k_{rl,f\to m}$ is the relative permeability for fracture-to-matrix flow.

An analogous form of Eqs. (2-3) or (2-5) defines mass flow of gas between the matrix and fracture continua.

$$q_g = \frac{k_{\text{harmonic}} k_{rg}}{\mu_g} \frac{P_{gf} - P_{gm}}{d} \tag{2-6}$$

where the *g* subscript denotes gas.

Note that for gas flow between the matrix and fracture continua, the upstream relative permeability is always used.

Analogous to mass flow are expressions and relationships for heat flow. Heat flow across the matrix fracture interface is defined

$$q_{\text{heat}} = k_{\text{harmonic}} \frac{T_f - T_m}{d} \tag{2-7}$$

Note that heat transfer and mass transfer across the matrix-fracture interface are coupled processes, but each responds to its respective driving forces calculated for the same distance, *d*. Gradients that drive mass and heat transfer are decreased when the block dimensions are increased (i.e., the differences in pressure or temperature between the two continua remain the same for each model element while the distance inwhich the difference occurs increases with an increased block size, thereby reducing the gradients).

2.2 Relative Permeability Functions

Spatially variable values for absolute rock permeability (variable in three spatial directions) and media characteristic curves for relative permeability and capillary pressure can be specified in MULTIFLO. Capillary saturation relations provided in MULTIFLO are based on either van Genuchten (1980), linear, or Brooks-Corey (Brooks and Corey, 1966) functions.

Liquid-phase relative permeability, k_{rl}, is calculated using the Mualem relationship (Mualem, 1976).

$$k_{rl} = \sqrt{s_l^{eff}} \left\{ 1 - \left[1 - \left(s_l^{eff} \right)^{1/\lambda} \right]^{\lambda} \right\}^2 \tag{2-8}$$

Saturation is related to the capillary pressure, P_c, by the van Genuchten relationship (van Genuchten, 1980)

$$s_l^{eff} = \left[1 + \left(\alpha |P_c| \right)^m \right]^{-\lambda} \tag{2-9}$$

where effective liquid saturation, s_l^{eff}, is defined by

$$s_l^{eff} = \frac{s_l - s_l^r}{s_l^o - s_l^r} \tag{2-10}$$

and where *r* and *o* denote residual and maximum saturations. The symbols α and λ are the van Genuchten parameters. λ is related to *m* in Eq. (2-9) by $\lambda = 1 - 1/m$.

The gas-phase relative permeability, k_{rg}, is defined in terms of k_{rl}

$$k_{rg} = 1 - k_{rl} \tag{2-11}$$

Alternatively, the Brooks-Corey functions could be used to define liquid- and gas-phase relative permeability (Brooks and Corey, 1966)

$$k_{rl} = s_*^4 \tag{2-12}$$

and

$$k_{rg} = \left(1 - s_*^2 \right) \left(1 - s_* \right)^2 \tag{2-13}$$

where saturation, s_*, is defined by

$$s_* = \frac{s_l - s_l^r}{1 - s_l^r - s_g^r} \tag{2-14}$$

Note that for the Brooks-Corey functions $k_{rl} + k_{rg} \neq 1$, except for $s_* = 0$.

The linear relations for liquid- and gas-phase relative permeability are defined

$$k_{rl} = s_{lin} \tag{2-15}$$

and

$$k_{rg} = 1 - k_{rl} \tag{2-16}$$

where saturation, s_{lin}, is defined by

$$s_{lin} = \frac{s_l - s_l^r}{1 - s_l^r} \tag{2-17}$$

MULTIFLO provides the user with the option to directly reduce the fracture-to-matrix relative permeability function by a constant factor. This reduction is incorporated by multiplying the relative permeability function by a relative permeability reduction factor, η,

$$k_{rl,f \rightarrow m} = \eta k_{rl,f} \tag{2-18}$$

This application attenuates liquid flow from the fracture continuum to the matrix continuum, but allows heat and gas flow to flow unimpeded.

2.3 Active Fracture Model

The active fracture model for unsaturated flow through fractured rocks proposed by Liu, et al. (1998) can also be implemented in MULTIFLO. The active fracture model is based on the hypothesis that only a portion of connected fractures actively conduct water. The hypothesis stipulates that (i) all connected fractures are active if the system is fully saturated, (ii) all fractures are inactive if the system is at residual saturation, and (iii) the fraction of fractures that are active is related to water flux through the fractures. Liu, et al. (1998), proposed that the fraction of active fractures be a power function of effective water saturation in connected fractures. The liquid-phase relative permeability function for flow within the fracture system defined in Eq. (2-8) is modified to (Liu, et al., 1998)

$$k_{rl} = \left(s_l^{\text{eff}}\right)^{\frac{1+\gamma}{2}} \left\{1 - \left[1 - \left(s_l^{\text{eff}}\right)^{\frac{1-\gamma}{\lambda}}\right]^{\lambda}\right\}^2 \tag{2-19}$$

where the van Genuchten relationship between effective saturation and capillary pressure in Eq. (2-9) is modified to (Liu, et al., 1998)

$$s_l^{\text{eff}} = \left[1 + \left(\alpha |P_c|\right)^{\frac{m}{1-\gamma}}\right]^{-\lambda} \tag{2-20}$$

where γ is a positive constant depending on the properties of the fracture network. Relative permeability for fracture-to-matrix flow is specified as (Liu, et al., 1998).

$$k_{rlf\to m} = \left(s_l^{\text{eff}}\right)^{\frac{3}{2}(1+\gamma)}\left\{1-\left[1-\left(s_l^{\text{eff}}\right)^{\frac{1-\gamma}{\lambda}}\right]^{\lambda}\right\}^2 \tag{2-21}$$

The gas-phase relative permeability function is defined as the complement to the liquid-phase relative permeability.

$$k_{rg} = 1 - k_{rl} \tag{2-22}$$

An alternative would be to define k_{rg} by the Brooks-Corey function. Values for k_{rg}, k_{rl}, and P_c for the active fracture model are linearly interpolated from specified values of saturation included as a look-up table in MULTIFLO code Version 1.5.2.

2.4 Summary of Options for Modifying Matrix-Fracture Interaction

The three options for modifying the matrix-fracture interaction are

- Reducing interfacial area. In this option, A_{mod} is specified <1. The reduction in interfacial areas applies to all flows in both directions (fracture-to-matrix and matrix-to-fractures). The relative permeability for fracture to matrix flow is specified as the upstream (fracture) value $k_{rl,f\to m} = k_{rl,f}$.

- Constant relative permeability reduction factor. In this option, $A_{\text{mod}} = 1$ and $k_{rlf\to m} = \eta k_{rl,f}$ where $\eta < 1$. This option reduces liquid flow from matrix to fractures, but leaves all other fluxes unmodified.

- Active fracture model. In this case, $A_{\text{mod}} = 1$, fracture-to-matrix relative permeability $k_{rlf\to m}$ is specified by Eq. (2-20), fracture capillary pressures from Eq. (2-19), and fracture relative permeability from Eq. (2-18). All other fluxes are left unmodified.

3 NUMERICAL SOLUTION

Mass and Energy Transport (METRA) is based on a fully implicit formulation using a variable substitution approach. Space discretization is based on a block-centered grid using an integrated finite-volume difference scheme. This approach is suitable for structured and unstructured grid with arbitrary interblock grids connectivity and any polygon block boundary. Flow through fractured media may be represented by the dual continua model or by using an equivalent continuum medium in which the dual continuum is represented by an equivalent single continuum (Pruess and Narasimhan, 1985; Klavetter and Peters, 1986).

Three primary variables are required to describe a two-phase, nonisothermal system consisting of two species, water and air. The chosen primary variables are listed in Table 3-1, where P_l is the liquid pressure for a pure liquid system and P_g represents the total gas pressure for a two-phase or pure gas-phase system. X_a denotes the mole fraction of air with partial pressure P_a, s_g denotes gas saturation, and T denotes temperature. Note that gas saturation is related to liquid saturation by $s_g + s_l = 1$.

Three primary equations are solved by the METRA code: (i) total mass balance, (ii) air mass balance, and (iii) energy balance. The three equations are simultaneously solved for each grid block by the tridiagonal Thomas algorithm for one-dimensional systems and, optionally, by the WATSOLV package (van der Kwaak, et al., 1995). The WATSOLV package is based on a preconditioning step using incomplete factorization accelerated by employing generalized minimum residual or biconjugate gradient stabilized procedures suitable for both two-dimensional and three-dimensional systems (van der Kwaak, et al., 1995).

Table 3-1. Choice of Primary Variable for Different Fluid States

Fluid State	Primary Variables
Single-phase liquid	P_l, X_a, T
Two phase	P_g, P_a, s_g
Single-phase gas	P_g, P_a, T

4 EXPERIMENTAL TEST RESULTS

Results from two experiments are used to evaluate conceptual models and property values assigned to MULTIFLO simulations of multiphase heat and mass transfer through partially fractured porous media. One experiment consists of two tests conducted at the laboratory scale at the Center for Nuclear Regulatory Analyses (CNWRA). The second experiment is the Drift-Scale Heater Test conducted in the Exploratory Studies Facility at Yucca Mountain. The spatial scale is of the order of 1 m [3.28 ft] for the laboratory experiment and 50 m [164 ft] for the field-scale experiment. Descriptions of the experiments are followed by results from the tests. Details of the Drift-Scale Heater Test are provided in numerous publications [see CRWMS M&O (1997a,b), for example]. Details of the laboratory-scale test are included in the following section.

4.1 Laboratory-Scale Heater Test

The laboratory-scale heater experiment was conducted at CNWRA. Two related tests, Tests 1 and 2, were conducted as part of the experiment to observe moisture redistribution around a heat source located in a partially saturated fractured, porous medium. The assembly of the apparatus was the same for both experiments. The experimental apparatus was a 1.2 × 1.2 × 0.6 m [3.9 × 3.9 × 2.0 ft] test cell assembled with solid rectangular (0.05 × 0.05 × 0.60 m [0.16 × 0.16 × 2.0 ft] cast concrete blocks [Figure 4-1]. A 0.15-m [0.5 ft] diameter drift is located in the center of the test cell [Figure 4-2]. The spaces between the blocks were intended to mimic horizontal and vertical fractures. Fracture hydraulic properties were not measured. The concrete blocks were fabricated from a mixture of bentonite clay, barite, and portland cement. The concrete blocks had the following measured property values: permeability of 2.0×10^{-17} m^2 [2.1×10^{-16} ft^2] , total porosity of 0.50, thermal conductivity of 0.5 W/m-K (dry) and 1.0 W/m-K (wet), and van Genuchten α of 6.36 10^{-7} Pa^{-1} and n of 0.7619 (Green, et al., 1995). The van Genuchten α and n are fitting parameters for the moisture retention curve. Saturations of two samples of the concrete were measured at 0.15 and 0.20 prior to Test 1.

A 0.15-m [0.5-ft] long, 0.019-m [0-75 in] diameter cylindrical cartridge heater was placed horizontally in the cylindrically shaped {0.15-m [0.5-ft] diameter} drift centrally located in the test cell. The cartridge heater was set at approximately 142 watts in both tests, calculated from measurements of 80 volts at the power source and 1.78 amps and 44.4 ohms through the heater. The cartridge heater, which was placed on a small pedestal approximately 0.015 m [0.6 in] above the floor of the drift during Test 1 and was placed directly on the concrete blocks forming the base of the drift during Test 2.

Water was infiltrated through a 0.30-m [1.0 ft] long, 0.025-m [1.0 in] diameter porous ceramic hollow cylinder placed over the centrally located fracture at the top of the test cell to simulate the natural sources of water (i.e., infiltration and condensed water that originated from vaporized rock water). Tap water from a carbonate aquifer was pumped at a rate of 1L/day (equivalent to approximately one drop every 2 seconds) into the porous cylinder.

Test 1 ran for a total of 140 days, 5 days of heating only followed by 125 days of heating and infiltration, culminating with 10 days of infiltration during a ramp-down of the heat source. Test 2 ran for a total of 215 days, again with 5 days of heating only followed by 167 days of constant heating and infiltration but this test ended with 43 days of infiltration during a ramp-down of the heat source. The heat source was incrementally and linearly decreased during Test 2 from

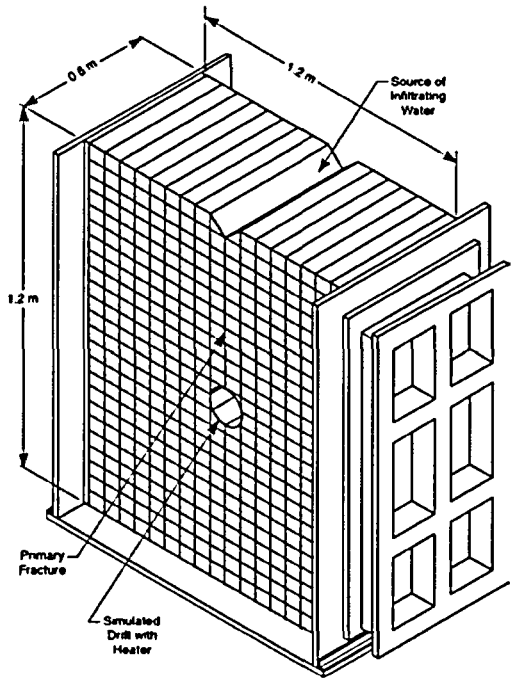

Figure 4-1. Laboratory-Scale Experiment Schematic [1 m = 3.28 ft]

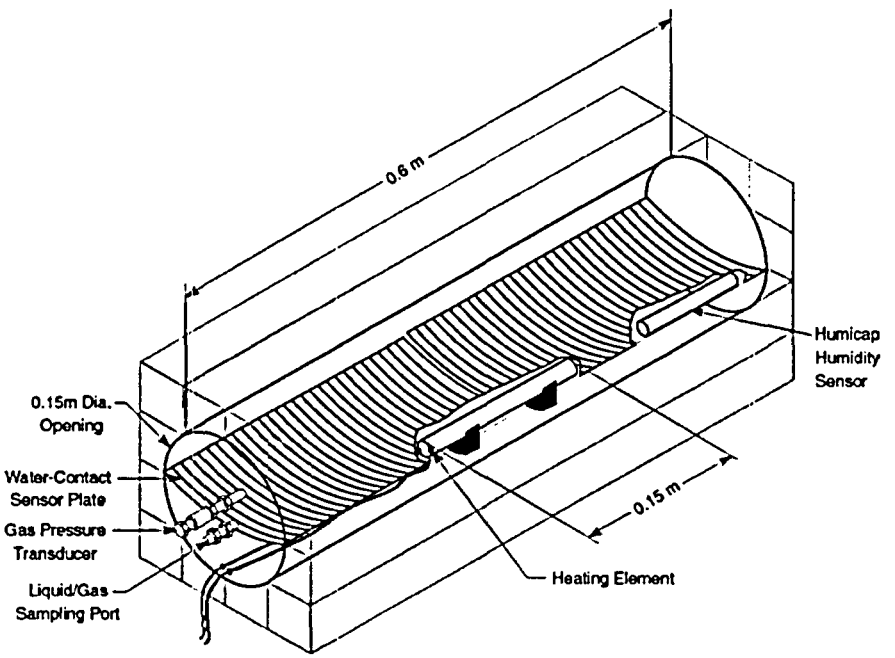

Figure 4-2. Schematic of Laboratory-Scale Experiment Drift [1 m = 3.28 ft]

142 watts at day 167 to 36.8 watts at day 215, at which time the experiment was terminated. There was a brief power outage for approximately 20 hours at day 153 of Test 2.

Temperature was measured in the media of the test cell using 100 thermocouples strategically placed along the vertically oriented fracture that was coplanar to the axis of the drift (referred to as the primary fracture) and in additional fractures throughout the test cell in Test 1. The 100 thermocouples were repositioned in only two vertically oriented planes in Test 2, one plane in the primary fracture and the second in one-half of a plane perpendicular to the primary fracture in the middle of the test cell. The locations of thermocouple placement in the primary fracture for Tests 1 and 2 are illustrated in Figure 4-3. A greater density of temperature measurements in the primary fracture was provided by the thermocouple placement in Test 2. With this instrumentation, liquid flow at locations initially above boiling could be detected using thermocouples when downward moving water depressed the temperature to below boiling. This same technique was used during the field-scale Fran Ridge Large Block Test (Wilder, et al., 1998) to detect liquid flowing down fractures. Temperature measurements were taken once or twice daily during Test 1 and hourly during Test 2. Temperatures measured during Test 2 in the planes perpendicular and parallel relative to the heated drift are illustrated in Figure 4-4.

Saturations of the test matrix at the onset of Test 1 (0.15 to 0.20) and the conclusion of Test 2 (Figure 4-5) were measured. However, saturations at the conclusion of Test 1 and the start of Test 2 were not measured and had to be inferred. Initial saturations assigned to Test 2 were modified to achieve the best agreement between simulations and matrix saturation measured at the conclusion of Test 2 and matrix temperatures measured throughout the test. An initial matrix saturation of 0.30 was determined to provide the best agreement during the analyses.

Insight into the nature of flow through the fractures of the laboratory-scale experiment was gained when the test assembly was disassembled at the conclusion of Test 1 and prior to Test 2. During inspection of the blocks, coatings of aragonite and calcite precipitates were detected on fracture selected fracture surfaces. It is interpreted that the precipitates could have been deposited either during evaporation or from retrograde precipitation (e.g., precipitation that increases with an increase in temperature) during the time when water was infiltrated into the test cell. Irrespective of which process led to formation of the precipitate, the presence of these minerals identified which fractures experiences flow during the heating phase of Test 1. Based on this interpretation, fracture flow was restricted to a zone that emanated from the source area of infiltration at the porous cylinder and expanded laterally in a parabolic shape as it flowed downward and eventually extended to a width of approximately 0.15 m [0.5 ft] beyond the sides of the drift.

4.2 Drift-Scale Heater Test

The Drift-Scale Heater Test is being conducted in the Exploratory Studies Facility Thermal Test Facility (Alcove 5) located in the Topopah Spring middle nonlithophysal (Tptpmn or tsw34) unit, within the horizon of the proposed Yucca Mountain repository (CRWMS M&O, 1997a). The tsw34 unit is approximately 30- through 40-m [100- through 130-ft] thick at the location of the Drift-Scale Heater Test. It is overlain by the Topopah Spring upper lithophysal (Tptpul or tsw33) and underlain by the Topopah Spring lower lithophysal (Tptpll or tsw35) units. Alcove 5 is at Construction Station 28 + 27 (a coordinate system in meters following the axis of the Exploratory Studies Facility and originating at the North Portal), just past the bend from the North Ramp to the Main Drift (as shown in Figure 4-6, taken from CRWMS M&O, 1997a).

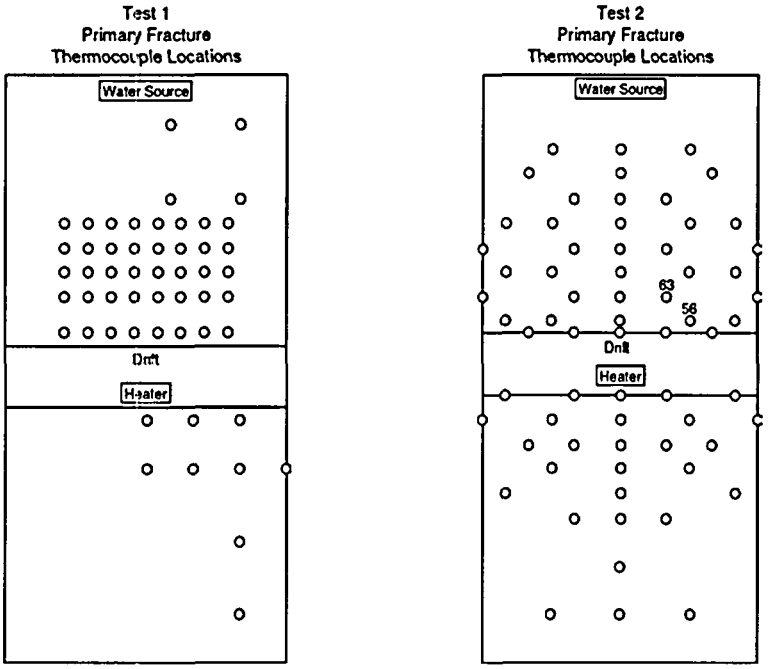

Figure 4-3. Thermocouple Locations in Test 1 (a) and Test 2 (b) of the Laboratory-Scale Experiment

A plan-view schematic of the principal components of the Drift-Scale Heater Test is shown in Figure 4-7. The 5-m [16.4-ft] diameter, 47.5-m [155.8-ft] long heated drift is closed at the east end by a thermal bulkhead. Approximately 12.5 m [41.0 ft] of the west end of the heated drift is lined with cast-in-place concrete ground support. The heated drift diameter was expanded to 5.6 m [18.4 ft] along this section to allow for the concrete ground support. Concrete inverts with a thickness of 1.2 m [3.9 ft] at the drift mid-plane were placed along the entire floor of the heated drift to provide a flat surface. Thermal sources for the heated drift consist of 9 canister heaters, placed end to end on the floor of the heated drift, and 50 wing heaters (25 on either side), emplaced in horizontal boreholes drilled into the sidewalls of the heated drift approximately 0.25 m [0.9 ft] below the springline. The wing heaters are spaced 1.83 m [6.0 ft] apart. Each wing heater has two segments, both 5-m [16.4-ft] long, with a larger power output from the outer segment. The inner wing heater segment is separated from the heated drift by a space of 1.5 m [4.9 ft].

The Drift-Scale Heater Test block was characterized prior to the onset of heating. On-site characterization of the local geology, *in situ* hydrology, and local rock mass quality were supplemented with laboratory tests of thermal-hydrological-mechanical-chemical properties. Characterization data collected from the single-heater test block [Tsang, et al. (1999); Blair, et al. (1998); Tsang and Birkholzer (1999)] were incorporated. The ensemble of these data provides the characterization of the Drift-Scale Heater Test block and model parameters are compared with results from previous nonthermal test studies by Brechtel, et al., 1995; Birkholzer and Tsang, 1997, 2000; and CRWMS M&O, 1997a, 1998a). The most current property values

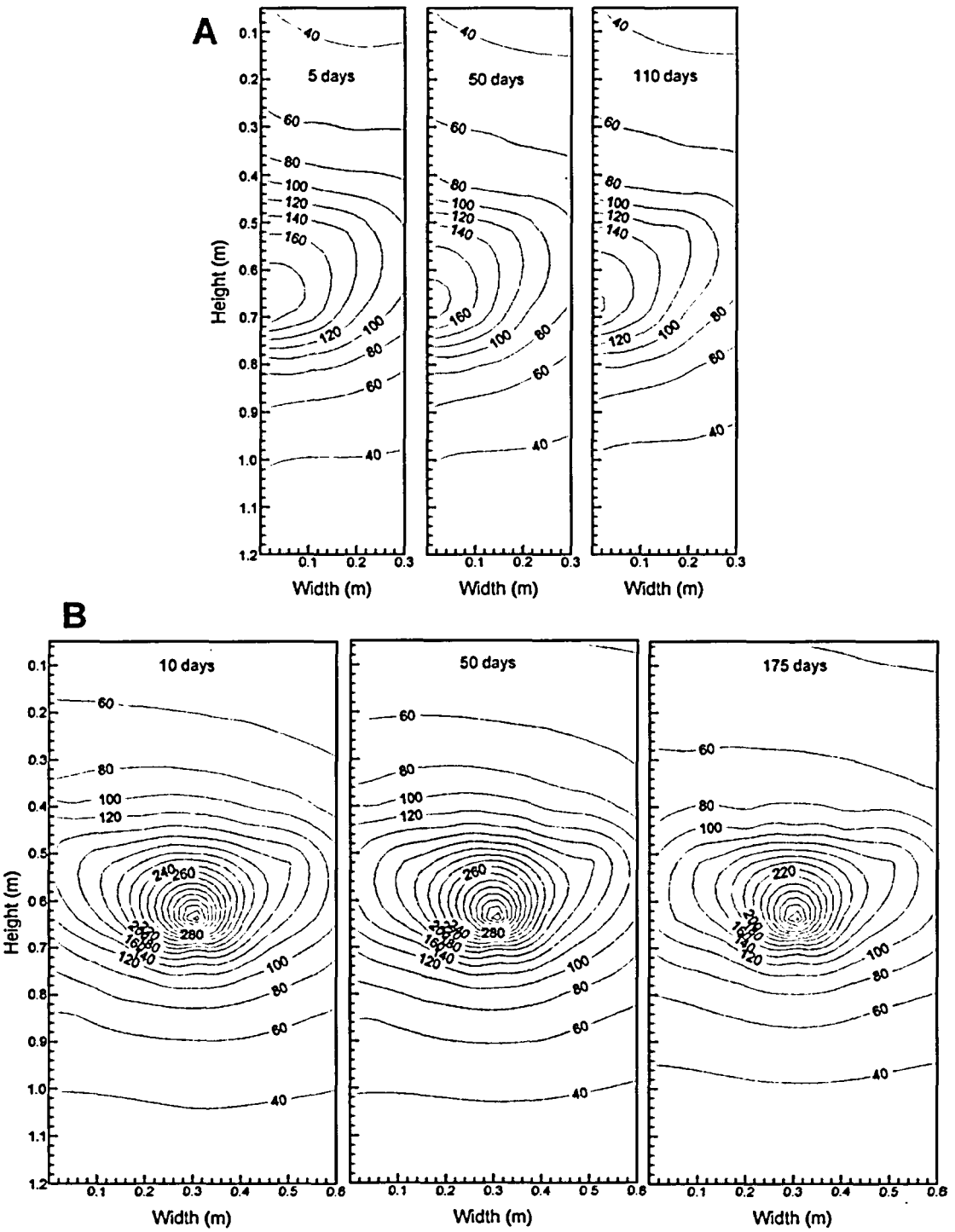

Figure 4-4. Measured Laboratory-Scale Experiment Temperatures for the Matrix Continuum, Perpendicular (A) and Parallel (B) to the Heated Drift {1 m [3.28 ft]}

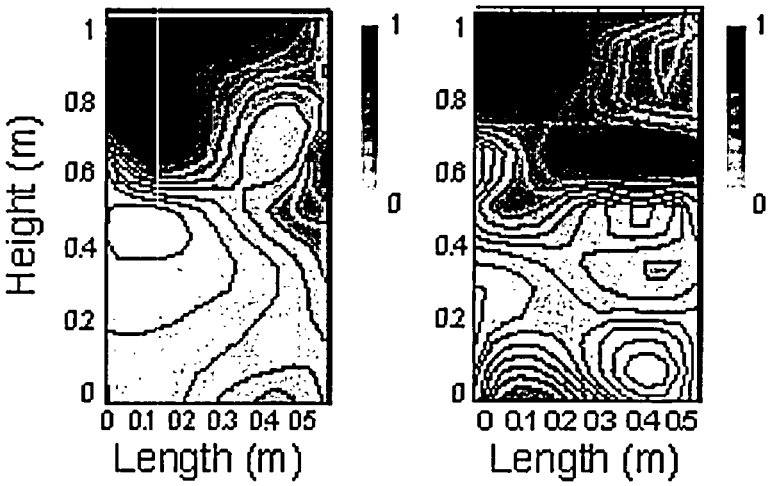

Figure 4-5. Saturation Measured at the Mid-Plane (Left) and Edge Plane (Right) of the Laboratory-Scale Experiment [1 m = 3.28 ft]

for the field-scale test site are from CRWMS M&O (2000b). Selected property values are summarized in Table 4-1. (Note that fracture permeability is expressed in terms of bulk values. Bulk fracture permeability can be calculated by multiplying the intrinsic values by the fracture porosity.) Included in Table 4-1 are property values from earlier references dating back to 1993. The data have been tabulated into nine groups. Similar data are combined into groups, with the most recent data listed first in the table.

A review of fracture porosity values cited in the technical literature indicates that prior to 2000, porosity values assigned to the tsw34 ranged from 1.24×10^{-4} to 1.46×10^{-4}. In the site-scale unsaturated-zone model for Total System Performance Assessment–Viability Assessment (Bodvarsson, et al., 1997), two-dimensional porosities were calculated for units exposed in the Experimental Studies Facility (i.e., tsw33 and tsw34). The two-dimensional fracture porosity was calculated from the rock face as the total fracture area (aperture times trace length) divided by the area enclosing the traces. One-dimensional porosities were derived from boreholes for the underlying unit (i.e., tsw35). The one-dimensional fracture porosity was calculated from borehole core samples as a product of the aperture and frequency, assuming all fractures are continuous.

Fracture porosity values cited after 1999 were based on a combination of porosity data derived from gas tracer tests conducted in the Experimental Studies Facility and porosity estimates based on the geometry of fracture networks (CRWMS M&O, 2000a). Gas tracer tests were performed in the Experimental Studies Facility to obtain estimates of the effective fracture porosity for the tsw34 hydrostratigraphic layer. Fracture porosities, estimated from the tracer tests, ranged from 0.006 to 0.02. These values were also consistent with those estimated from the Experimental Studies Facility seepage test results (CRWMS M&O, 2000a). Based on these

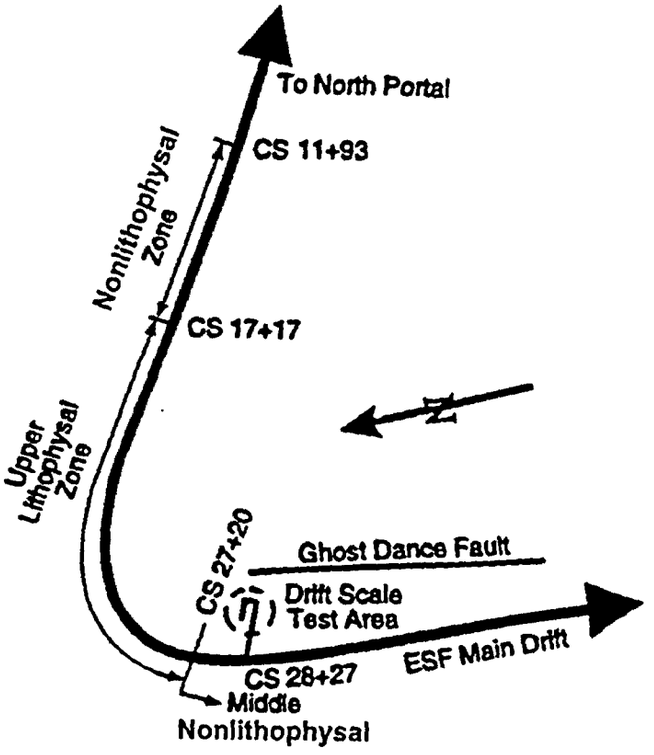

(a) Plan View

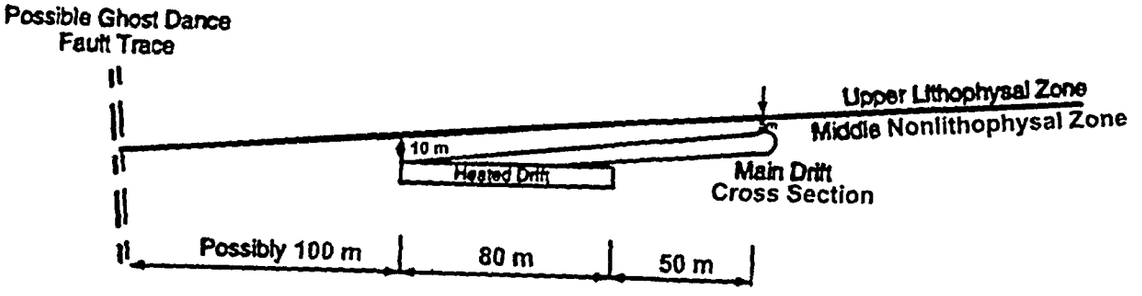

Reference Only
(SCALE APPROXIMATE)

(b) Profile View

Figure 4-6. Location of the Exploratory Studies Facility Drift-Scale Heater Experiment [1 m = 3.28 ft]

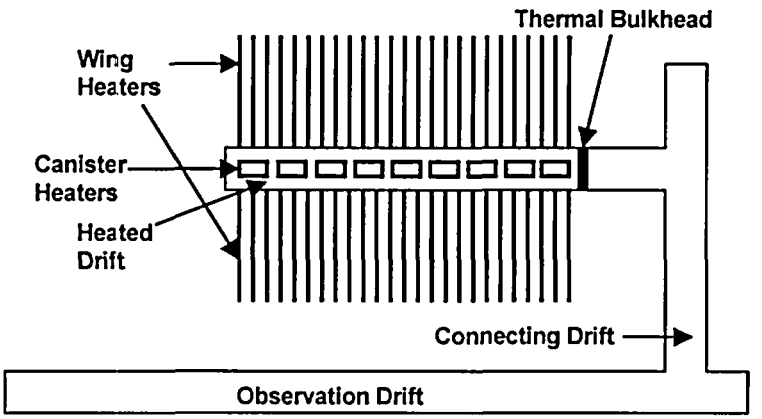

Figure 4-7. Plan-View Layout of Principal Components of the Drift-Scale Heater Test

results, an approximate average value of 0.01 was determined in CRWMS M&O (2000a) to be a reasonable estimate for fracture porosity for the tsw34.

Gas tracer test data were not available for hydrostratigraphic layers other than tsw34. Alternative approaches, similar to the one-dimensional and two-dimensional fracture porosity described previously, were used to estimate fracture porosity for other layers. However, the values were determined using a modified procedure (CRWMS M&O, 2000a). The large degree of uncertainty encountered in porosity measurements was cited as the basis for this modification in the one-dimensional and two-dimensional fracture porosity estimates. The porosity value for the tsw34, based on analyses of the gas tracer tests, was used to scale the fracture porosity for the other units. All of these values are on the order of 0.01, the value assigned to the tsw34. The scaling scheme resulted in an increase of porosity by two orders of magnitude (10^{-4} to 10^{-2}) for both the tsw33 and tsw35 units. This scaling scheme was used to estimate fracture porosities in the absence of more rigorous approaches or supporting data. These estimates are to be updated when gas tracer test data are available.

The design thermal load for the Drift-Scale Heater Test was 68.0 kW for the canister heaters and 143.0 kW for the cumulative wing heaters (85.8 kW at the outer wing heater and 57.2 kW for the inner wing heaters) for a total of 211 kW (CRWMS M&O, 1998c). The Drift-Scale Heater Test has experienced decreased heat loads from the levels of the design heat loads since energizing in December 1997 (Figure 4-7). At the time of energizing, the canister heat load was approximately 52.8 kW, and the cumulative wing heater heat load was approximately 137 kW (CRWMS M&O, 1998d). These power levels decreased immediately after heating started. The canister heat load increase from days 244 to 270 is attributed to a modification in the access drift and heater drift (outside the thermal bulkhead) ventilation system. The wing heaters also experienced an increase in heat load soon after day 244; however, this increase followed a rather precipitous decrease in the heater load from approximately 133 kW at day 185 to less

than 130 kW by day 244 (CRWMS M&O, 1998b). The cause of this dramatic heat load decrease is attributed to the loss of power to wing heater 29. Measured heater load values continued to decrease to approximately 52.3 kW for the canisters and to slightly more than 130 kW for the wing heaters by day 480 (CRWMS M&O, 1999a) and to approximately 51.5 kW for the canisters and 128.2 kW for the wing heaters by day 700 (CRWMS M&O, 1999b). After 800 days of heating, both the canister and wing heaters were incrementally decreased on five occasions to ensure that measured drift wall temperatures did not exceed 200 °C [392 °F].

Table 4-1. Evolution of Property Values for the Hydrostratigraphic Units at the Drift-Scale Heater Test								
Layer	Matrix Permeability (m^2)*	Matrix Porosity	Matrix van Genuchten α	Fracture Permeability (m^2)*	Fracture Porosity	Fracture van Genuchten α	Active Fracture Parameter γ	Thermal Conductivity Dry, Wet (W/m-K)†
tsw33‡§‖	3.08×10^{-17}	0.154	2.13×10^{-05}	5.50×10^{-13}	6.60×10^{-03}	1.46×10^{-03}	0.41	0.79, 1.68
tsw34‡§‖	4.07×10^{-18}	0.110	3.86×10^{-06}	2.76×10^{-13}	1.00×10^{-02}	5.16×10^{-04}	0.41	1.56, 2.33
tsw35‡§‖	3.04×10^{-17}	0.131	6.44×10^{-06}	1.29×10^{-12}	1.10×10^{-02}	7.39×10^{-04}	0.41	1.20, 2.02
tsw33¶	2.30×10^{-17}	0.154	1.81×10^{-05}	7.70×10^{-13}	—	1.60×10^{-03}	—	—
tsw34¶	7.50×10^{-19}	0.110	3.69×10^{-06}	3.40×10^{-13}		6.80×10^{-04}		
tsw35¶	3.10×10^{-17}	0.131	6.41×10^{-06}	9.00×10^{-13}		1.00×10^{-03}		
tsw33#	4.07×10^{-18}	0.089	1.02×10^{-06}	9.84×10^{-10}	1.46×10^{-04}	8.36×10^{-04}	—	1.67, 2.10
tsw34#								
tsw35#								
tsw33**††	1.15×10^{-17}	0.135	6.76×10^{-06}	2.63×10^{-11}	1.05×10^{-04}	1.78×10^{-04}	—	—
tsw34**††	4.07×10^{-18}	0.089	1.02×10^{-06}	6.76×10^{-12}	1.24×10^{-04}	9.77×10^{-05}		
tsw35**††	1.55×10^{-17}	0.115	3.31×10^{-06}	3.80×10^{-12}	3.29×10^{-04}	1.10×10^{-04}		
tsw33‡‡	2.30×10^{-17}	0.154	6.57×10^{-06}	—	—	—	—	—
tsw34‡‡	1.50×10^{-18}	0.110	6.40×10^{-07}					
tsw35‡‡	7.00×10^{-18}	0.130	2.73×10^{-06}					
tsw33§§	2.00×10^{-17}	—	6.60×10^{-06}	4.00×10^{-12}	—	—	—	—
tsw34§§	4.00×10^{-18}		6.40×10^{-07}	4.00×10^{-12}				
tsw35§§	2.30×10^{-17}		2.70×10^{-06}	4.00×10^{-12}				
tsw33‖	4.00×10^{-18}	0.130	2.00×10^{-06}	Fracture properties were not defined explicitly but were added to the rock matrix characteristic curves through the equivalent continuum approximation. This approach assumes that the capillary pressure of the equivalent continuum is equal to that of the matrix until the threshold saturation is exceeded, then fracture flow, described by a linear relationship between capillary pressure and saturation, dominates that matrix contribution to flow.			—	—
tsw34‖	5.00×10^{-18}	0.140	1.33×10^{-06}					
tsw35‖	N/A							

Table 4-1. Evolution of Property Values for the Hydrostratigraphic Units at the Drift-Scale Heater Test (continued)

Layer	Matrix Permeability (m^2)*	Matrix Porosity	Matrix van Genuchten α	Fracture Permeability (m^2)*	Fracture Porosity	Fracture van Genuchten α	Active Fracture Parameter γ	Thermal Conductivity Dry, Wet (W/m-K)†
tsw33[¶¶] tsw34[¶¶] tsw35[¶¶]	—	—	—	—	—	—	—	1.73 (average)
tsw33[##] tsw34[##] tsw35[##]	2.40×10^{-17} 2.40×10^{-17} 2.40×10^{-17}	—	3.00×10^{-06} 3.00×10^{-06} 3.00×10^{-06}	4.60×10^{-09} 4.60×10^{-09} 4.60×10^{-09}	—	—	—	—

*Note: [1m = 3.28 ft]
†Note: [13.87 W/m-K = 1B/ft-hr-°F]
‡CRWMS M&O. "Multiscale Thermohydrologic Model." ANL–EBS–MD–000049. Rev. 00 ICN 02. Las Vegas, Nevada: CRWMS M&O. 2001.
§CRWMS M&O. "Calibrated Properties Model." MDL–NBS–HS–000003. Rev. 00. Las Vegas, Nevada: CRWMS M&O. 2000.
‖CRWMS M&O. "Thermal Tests Thermal-Hydrological Analyses/Model Report." ANL–NBS–TH–000001. Rev. 00 ICN 01. Las Vegas, Nevada: CRWMS M&O. 2000.
¶Brodsky, N.S., C.L. Howard, R.S. Taylor, and J.T. George. "Field Thermal Conductivity Measurements of the Topopah Spring Lower Lithophysal Units." Proceedings of the 10th International High-Level Radioactive Waste Management Conference, Las Vegas, Nevada, March 30—April 3,2003. La Grange Park, Illinois: American Nuclear Society. 2003.
#CRWMS M&O. "Single Heater Test Final Report." BAB000000–01717–5700–00005. Rev. 00 ICN 1. Las Vegas, Nevada: CRWMS M&O. 1999.
**CRWMS M&O. "Total System Performance Assessment—Viability Assessment (TSPA-VA) Analyses Technical Basis Document." B00000000–01717–4301–00002. Rev. 01. Las Vegas, Nevada: CRWMS M&O. 1998.
††Bodvarsson, G.S., T.M. Bandurraga, and Y.S. Wu, eds. "The Site-Scale Unsaturated Zone Model of Yucca Mountain, Nevada, for the Viability Assessment." LBNL–40376. Berkeley, California: Lawrence Berkeley National Laboratory. 1997.
‡‡Flint, L.E. "Characterization of Hydrogeologic Units Using Matrix Properties, Yucca Mountain, Nevada." U.S. Geological Survey Water Resources Investigations Report 97-4243. 1998.
§§Bodvarsson, G.S. and T.M. Bandurraga, eds. "Development and Calibration of the Three-Dimensional Site-Scale Unsaturated Zone of Yucca Mountain, Nevada." LBNL–39315. Berkeley, California: Lawrence Berkeley National Laboratory. 1996.
‖‖Wittwer, C.S., G. Chen, G.S. Bodvarsson, M. Chornack, A.L. Flint, L.E. Flint, E. Kwicklis, and R. Spengler. "Preliminary Development of the LBL/USGS Three-Dimensional Site-Scale Model of Yucca Mountain, Nevada." LBL–37356. Berkeley, California: Lawrence Berkeley National Laboratory. 1995.
¶¶Ryder, E.E., R.E. Finley, J.T. George, C.K. Ho, R.S. Longenbaugh, and J.R. Connolly. "Bench-Scale Experimental Determination of the Thermal Diffusivity of Crushed Tuff." SAND94–2320. Albuquerque, New Mexico: Sandia National Laboratories. 1996.
##Wilson, M.L., J.H. Gauthier, R.W. Barnard, G.E. Barr, H.A. Dockery, E. Dunn, R.R. Eaton, D.C. Guerin, N. Lu, M.J. Martinez, R. Nelson, C.A. Rautman, T.H. Robey, B. Ross, E.E. Ryder, A.R. Schenker, S.A. Shannon, L.H. Skinner, W.G. Halsey, J. Gansemer, L.C. Lewis, A.D. Lamont, I.R. Triay, A. Meijer, and D.E. Morris. "Total System Performance Assessment for Yucca Mountain—SNL Second Iteration (TSPA–1993)." SAND93–675. Albuquerque, New Mexico: Sandia National Laboratories. 1993.

5 NUMERICAL MODEL DEVELOPMENT

5.1 Laboratory-Scale Heater Test

The laboratory-scale test cell was numerically modeled in three dimensions. Symmetry along two planes justified modeling one-fourth of the test cell. The model grid consisting of slightly more than 10,000 elements for each continuum is illustrated in Figure 5-1. Material properties were assumed uniform throughout the test cell and assigned values from actual measurements for the concrete matrix (Green, et al., 1995) and from estimates for the fractures. Hydraulic properties used in the numerical model are assumed to represent the fractures of the intact test cell after assembly. External boundaries were specified as no fluid flow, but allowed some heat flow (loss). Thermal properties assigned to the boundaries to effect heat loss were determined by matching numerically predicted temperatures with observed temperatures at 5 and 10 days of heating (i.e., prior to effects from infiltration) and at 110 days (i.e., the effects of both heating and infiltration were included). The drift was modeled as a highly permeable fractured medium and was assigned a thermal conductivity value of 10 W/m-K to indirectly account for radiative heat transfer through the air space. The initial matrix saturation was set to 30 percent. Initial temperature was specified to be 20 °C [68 °F]. Basecase laboratory-scale heater test model properties are summarized in Table 5-1.

The cartridge heat source was set at 142 watts, calculated from measurements of 80 volts at the power source and 1.78 amps and 44.4 ohms through the heater. A source of water was introduced at a rate of 1 L/day (equivalent to approximately one drop every 2 seconds) into the fracture continuum at the top of the model.

5.2 Drift-Scale Heater Test

The Drift-Scale Heater Test was numerically simulated with a three-dimensional model. The three-dimensional model was assembled with a series of fourteen vertically oriented two-dimensional cross sections, seven that intersected the drift and seven located beyond the terminus of the drift. Two planes of vertical symmetry were assumed, one aligned with the axis of the heater drift and one that intersected the axis of the heater drift mid-distance between the bulkhead and the terminus of the heated drift. Therefore, one-fourth of the Drift-Scale Heater Test was included in the numerical model. The modeled area extended 200 m [656 ft] in the vertical direction with the center of the heated drift placed at the center of the numerical model and 100 m [328 ft] perpendicular to the drift center in the horizontal direction.

The two-dimensional grid with 1,123 nodes in the planes intersecting the drift and 1,175 nodes in the planes beyond the drift terminus is illustrated in Figure 5-2. A close-up of the two-dimensional grid in the vicinity of the heated drift is shown in Figure 5-3, which illustrates the finer mesh resolution in areas expected to experience large temperature, saturation, and pressure gradients. The three-dimensional model, therefore, had 16,068 nodes in each continua for a total of 32,136 nodes. The model domain was modeled as three hydrostratigraphic units, tsw33, tsw34, and tsw35 of the Topopah Spring welded unit. The principal components to the Drift-Scale Heater Test are located within the tsw34 unit. Basecase field-scale heater test model properties are summarized in Table 5-2 (CRWMS M&O, 2000b).

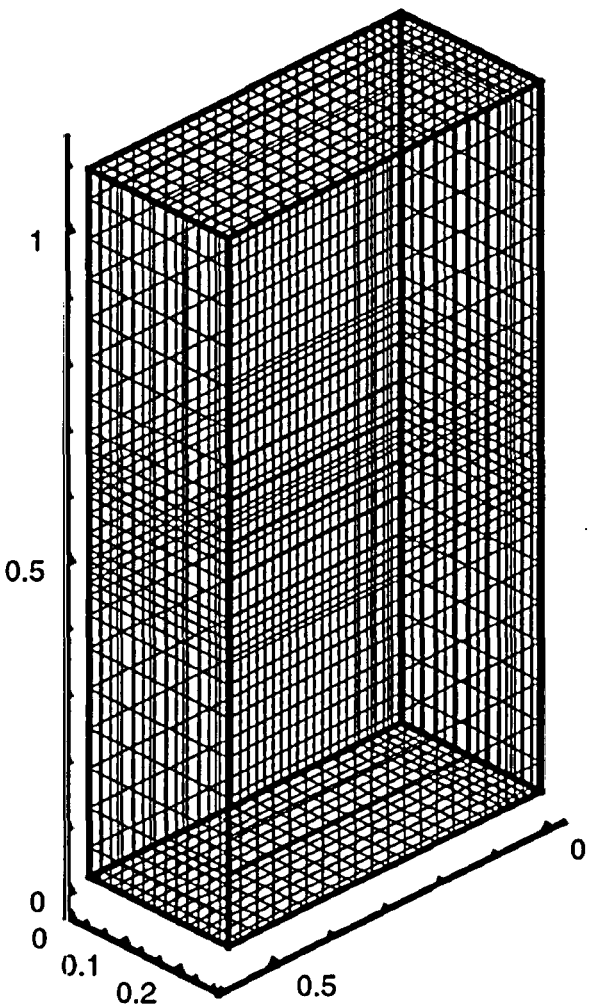

Figure 5-1. Numerical Grid for the Laboratory-Scale Heater Test

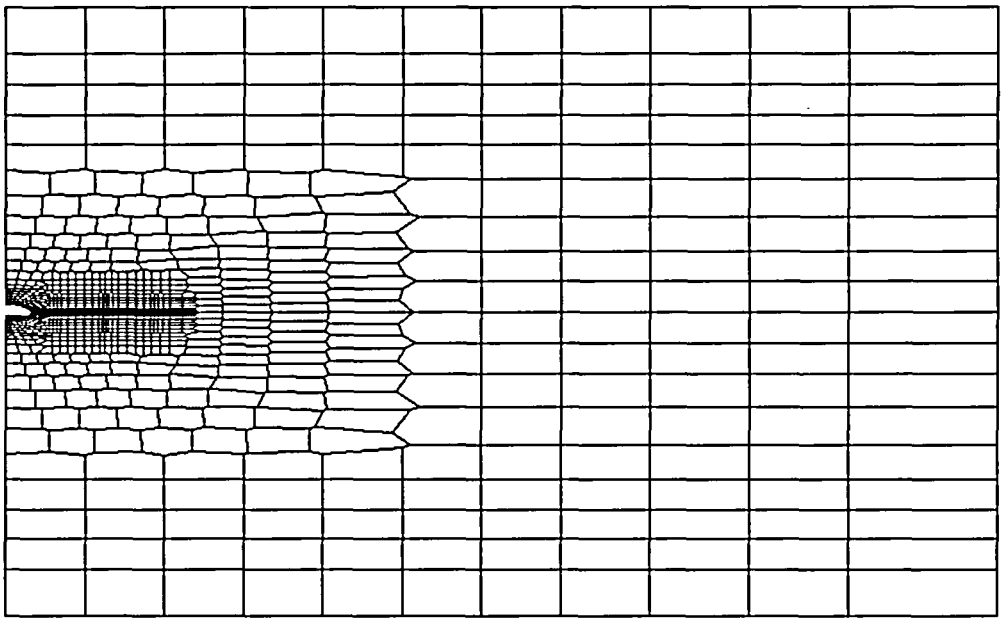

Figure 5-2. Numerical Grid for the Drift-Scale Heater Test

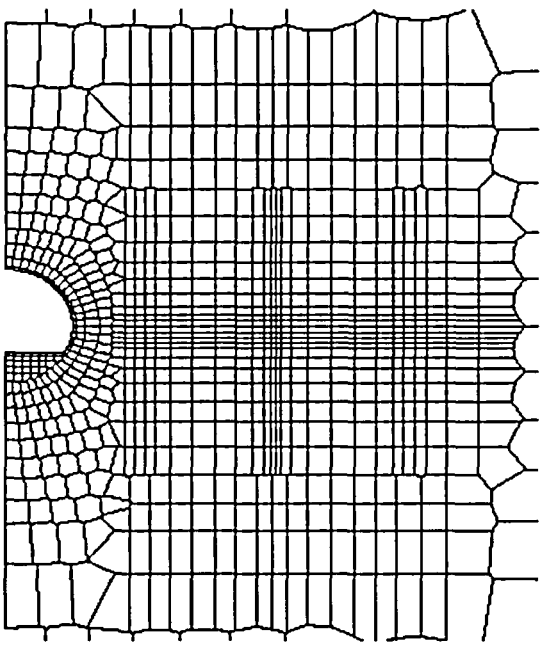

Figure 5-3. Close-Up View of the Numerical Grid for the Drift-Scale Heater Test

Table 5-1. Basecase Property Values for Laboratory-Scale Model		
Property	**Value**	**Source**
Matrix permeability [m^2]	2.0×10^{-17} [2.2×10^{-16} ft^2]	M*
Matrix porosity [-]	0.5	M
Matrix s_r [-]	0.05	E†
Matrix α [Pa^{-1}]	6.36×10^{-7}	M
Matrix m [-]	0.3717	M
Fracture permeability [m^2]	1.0×10^{-10} [1.1×10^{-9} ft^2]	E
Fracture porosity [-]	0.01	E
Fracture s_r [-]	0.01F	E
Fracture α [Pa^{-1}]	1.00×10^{-3}	E
Fracture m [-]	0.800	E
Thermal conductivity [dry] [W/m-k]	0.50	M
Thermal conductivity [wet] [W/m-k]	1.00	M
Rock specific heat [J/kg-K]	840	M
Rock density [kg/m^3]	1600 [100 lb/ft^2]	M
Area modifier A_{mod} [-]	1.0	E
Active fracture model γ [-]	0.4	E
*Measured †Estimated		

The vertical boundaries of the field-scale model were specified as adiabatic (i.e., no heat transfer) with no fluid flow. The top boundary was prescribed as a mixed boundary with specified flux. The mixed boundary condition at the top allowed gas and heat transport in or out of the model while maintaining pressure and temperature as specified. The water flux at the top boundary was introduced into the fracture continuum. The bottom boundary was prescribed as a gravity drainage boundary with specified pressure, temperature, and saturation. The heater drift was not explicitly included in the model; instead, the heater drift wall was modeled as a Dirichlet boundary, and heat from the floor canisters was applied directly to the heater drift walls. The effect of the Dirichlet boundary at the heater drift wall allowed the removal of sensible heat transported by water vapor. Heat removal from the drift wall by either conduction or radiation was not explicitly included in the simulation. The wing heaters were assigned the same hydraulic properties as the adjoining rock (tsw34).

Table 5-2. Basecase Property Values for Field-Scale Model				
Property	**Source**	**tsw33**	**tsw34**	**tsw35**
Matrix permeability [m^2]	M*	3.08×10^{-17} [3.31×10^{-16} ft^2]	4.07×10^{-18} [4.38×10^{-17} ft^2]	3.04×10^{-17} [3.27×10^{-16} ft^2]
Matrix porosity [-]	M	0.154	0.110	0.131
Matrix s_r [-]	M	0.12	0.19	0.12
Matrix α [Pa^{-1}]	M	2.13×10^{-5}	3.86×10^{-6}	6.44×10^{-6}
Matrix m [-]	M	0.298	0.291	0.236
Fracture permeability [m^2]	M	5.50×10^{-13} [5.92×10^{-12} ft^2]	2.76×10^{-13} [2.97×10^{-12} ft^2]	1.29×10^{-12} [1.39×10^{-11} ft^2]
Fracture porosity [-]	M	0.0066	0.010	0.011
Fracture s_r	E†	0.01	0.01	0.01
Fracture α [Pa^{-1}]	M	1.46×10^{-3}	5.16×10^{-4}	7.39×10^{-3}
Fracture m [-]	M	0.608	0.608	0.611
Thermal conductivity [dry] [W/m-k]	M	0.79	1.56	1.20
Thermal conductivity [wet] [W/m-k]	M	1.68	2.33	2.02
Rock specific heat [J/kg-K]	M	882	948	900
Rock density [kg/m^3]	M	2,510 [156 lb/ft^3]	2,530 [157 lb/ft^3]	2,540 [158 lb/ft^3]
Area modifier A_{mod} [-]	E	1.0	1.0	1.0
Active fracture model γ [-]	E	0.4	0.4	0.4
*Measured †Estimated				

The temperature was specified as 22 [71.6] and 24 °C [75.2 °F] at the top and bottom boundaries for a geothermal gradient of 0.01 °C/m [0.005 °F/ft]. A static gas pressure difference of 1,920 Pa between the top and bottom boundaries was specified to impose a gas gradient consistent with ambient conditions. This pressure is equivalent to a 200-m [656-ft] tall column of air at standard pressure and temperature. Gas pressures of 88,920 Pa at the bottom and 87,000 Pa at the top gave a gas pressure at the Drift-Scale Heater Test horizon of slightly less than 88,000 Pa, consistent with observed gas pressures and gas pressure gradients (Bodvarsson, et al., 1997).

Heat was introduced into the model at the drift wall and at the inner and outer wing heaters. The drift cavity was not explicitly included in the model to avoid difficulties associated with representing the air space within the drift, radiative and convective heat transfer between the heater canisters and the drift wall, and the physics of heat and mass transfer at the drift-cavity/drift-wall boundary. The disadvantage to this simplification is that coupled thermal-hydrological processes at the drift wall cannot be directly or easily investigated using this model. The heat source levels were applied uniformly according to surface area to the drift boundary elements at the 5-m [16.4-ft] diameter drift wall and to the elements at the top of the invert. The 50 cylindrical wing heaters were not individually represented in the numerical model, but both the inner and outer wing heaters were represented as individual rectangular slabs, thereby smearing the heat deposition in the y-direction of the model. The 4.49-m [14.7-ft] long inner wing heater was set 1.67 m [5.5 ft] from the drift wall. The 4.59-m [15.1-ft] long outer heater was separated from the inner heater by 0.66 m [2.2 ft]. These dimensions are consistent with those provided in the as-built report (CRWMS M&O, 1998d), with the exception of the wing heater thickness. The wing heaters were modeled as 0.25-m [0.8-ft] thick, rather than the reported diameter of 0.024 m [0.94 in], because of constraints on mesh resolution. The increased thickness of the wing heaters will distort the resulting thermal-hydrological regime in the region close to the heat source; however, the effect should be negligible beyond a few tens of centimeters.

Model heat loads were designed to resemble the major features of the measured heat loads (Figure 4-7). The model thermal loads were ramped up to their starting power levels during a period of approximately 4.2 hours to avoid stability problems. The measured cumulative heat load for the canister heaters was approximated to remain constant at 52.0 kW until day 800 of heating (Figure 5-4a). The canister heat was then linearly ramped down to 44 kW by day 1,000 and held at that heat load until day 1,200, at which time the heat load was linearly ramped down to 38 kW by day 1,500. In a similar fashion, the heat load for the wing heaters was linearly ramped down from a starting cumulative heat load of 136.5 kW at day 1 to 129 kW at day 800. This heat load was then linearly ramped down to 108 kW by day 1,000 and held constant at 108 kW until day 1,200, at which time the heat load was linearly ramped down to 91 kW at day 1,500. At all times, 40 percent of the cumulative wing heater heat load was assigned to the inner heater and 60 percent was assigned to the outer wing heater.

(a)

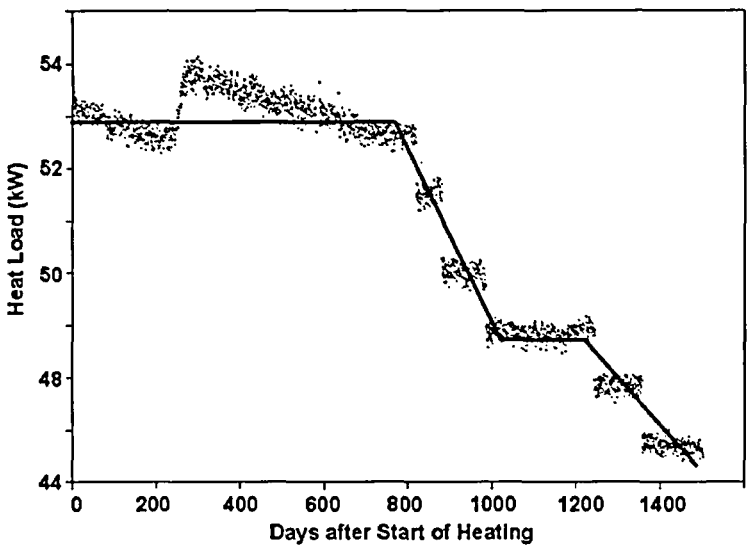

(b)

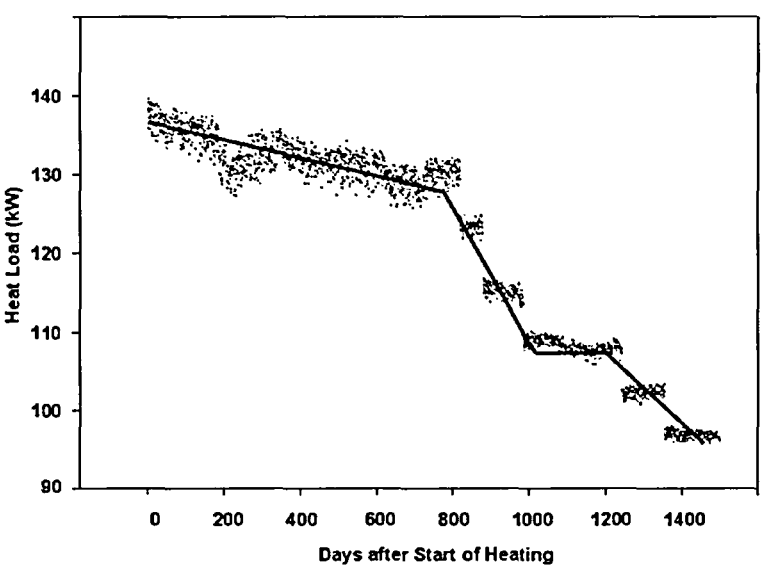

Figure 5-4. Drift-Scale Heater Test Heat Loads for the Canisters (a) and Wing Heaters (b)

6 MODEL RESULTS

Sensitivity analyses were performed on the laboratory- and field-scale experiments to assess pretest, ambient conditions and to evaluate the heating phases of the tests. The analyses provided insight as to which conceptual models and property values have an impact on the simulation of multiphase heat and mass transfer through partially saturated fractured rock. The specific analyses for the two scales of experiments were different. For example, sensitivity analyses to evaluate pretest, ambient conditions of the laboratory-scale test were essentially a single process in which both ambient and heating phase analyses were conducted simultaneously. It was not possible to assign appropriate thermal boundary conditions (i.e., thermal conductivity and specific heat) to the boundaries under pretest isothermal conditions alone. Therefore, additional simulation in the presence of the heat source was needed to establish its thermal boundary conditions. After all boundary conditions, property values, and heat and mass sources were determined, the heating phase of the laboratory-scale heater was simulated. A second difference between the two sets of analyses was that multiple parameters were varied during sensitivity analysis of the laboratory-scale experiment compared with only one parameter at a time varied during analysis of the field-scale experiment.

Sensitivity analyses were performed for the field-scale experiment in two stages. The effect of changes in boundary conditions and property values on ambient saturation was first evaluated. Ambient matrix saturation was selected as the key state variable to evaluate the appropriateness of the pretest conditions for the conceptual and numerical models used to simulate the Drift-Scale Heater Test. This selection was made because of the sensitivity of saturation to changes in model design and the ability to directly measure matrix saturation on core and grab samples collected at the site. A matrix saturation of 0.92 in the tsw34 was initially designated the target saturation. This target saturation is close to the value of 0.924 measured on samples collected at the Drift-Scale Heater Test (CRWMS M&O, 2000c). Most challenging in these analyses was evaluation of the coupled relationship among infiltration, ambient saturation, and fracture permeability. Block size, which is a function of fracture spacing and affects bulk fracture permeability, was also varied in this analyses. In particular, it was not possible to simulate a steady-state matrix saturation of 0.92 for the basecase properties and an infiltration rate of 3.0 mm/yr [0.12 in/yr]. It was determined to increase the target saturation to approximately 0.96–0.97 instead of decreasing infiltration.

The field-scale experiment was sufficiently large that model boundaries were set at a reasonable distance so that thermal boundary effects were avoided. Ambient conditions were replicated by simulating the test volume in the absence of heating until steady-state conditions were achieved. Evaluating the model under ambient conditions facilitated determination of prescribed boundary conditions (most importantly the surface infiltration) and property values. Thermal boundary conditions were not critical for the field-scale model because the model dimensions were sufficiently large to obviate thermal boundary effects. Once initial conditions were established, the effect of changes to boundary conditions and property values on evolution of the heating phase of the field-scale test was evaluated.

6.1 Laboratory-Scale Heater Test Model Results

Dynamic modeling using transient, nonisothermal simulations was conducted to establish the boundary conditions of the laboratory-scale model. This set of sensitivity analyses was critical for determination of the thermal boundaries. After the boundary conditions were established,

additional sensitivity analyses were conducted to evaluate the parameter values, which when varied, had a significant effect on the evolution of temperature and saturation in the test medium during the heating phase. Parameters varied in these analyses were fracture permeability (± 10 times, ± 100 times), matrix permeability (± 10 times), van Genuchten α (1.0×10^{-5}, 1.0×10^{-4}, 1.0×10^{-3}), active fracture model γ (0.2, 0.4, 0.6, 0.8), area modifier (0.1, 0.01, 0.001), and a reduction in the fracture to matrix relative permeability (0.1, 0.01, 0.001). The variability of values selected for analysis are within the range of natural variability and measurement error. These values are summarized in Table 6-1.

Simulation datasets using various combinations of the varied parameters are summarized in Table 6-2. Basecase parameter values are summarized in Table 5-1. Temperatures from the laboratory-scale simulations were mostly dependent on the boundary conditions. Because boundary conditions remained constant in these analyses, temperatures in all simulations for both the matrix and fracture continua were essentially the same with the exception of those with an area modifier, A_{mod}, less than 1.0. A maximum temperature difference of 44 °C [111 °F] between the matrix and fracture continua was experienced for an A_{mod} of 0.001 (lst157). Examples of temperature for the matrix continuum, which are representative of all simulations with A_{mod} equal to 1.0, are illustrated in Figures 6-1 and 6-2. Figure 6-1 is a contour plot of temperature for a vertical plane oriented perpendicular to the heated drift, and Figure 6-2 is a temperature plot for a vertical plane oriented parallel to the heated drift. Maximum matrix and fracture saturations and temperatures for the laboratory-scale analyses are presented in Table 6-3. Contour plots for temperature for all simulations are included in Appendix A in the attached compact disk for reference. Illustrations of matrix saturation at the mid-plane and the edge plane and fracture saturation in vertical planes perpendicular to the heated drift located at 0.01, 0.15, 0.23, and 0.25 m [0.033, 0.49, 0.75, and 0.82 ft] relative to the middle of the 0.30-m [1.0-ft] wide test cell for all simulations are included in Appendixes B and C in the attached compact disk for reference.

Saturations of both the matrix and fracture continua provide valuable insights. Simulated matrix saturations are of interest because they can be compared with matrix saturations measured at the conclusion of Test 2 (Figure 4-5). Simulated fracture saturations are of interest because they can be compared with anecdotal experimental observations taken at the conclusion of Test 1 and also provide critical insight on potential liquid flow into the heated drift during the heating phase.

Simulated matrix saturation varied when key input parameters were varied. Simulated matrix saturation was compared with the saturation measured at the conclusion of the experiment (Figure 4-5). The primary saturation features were more distinct at the mid-plane (Figure 4-5a). High saturation above the heated drift and a shadow of low saturation were observed below the drift in mid-plane. Less distinct saturation features were observed in the edge plane (Figure 4-5b). Some ponding above the heated drift and shedding off the side of the heated drift were observed in the edge plane. A less prominent shadow zone of low saturation formed below the heated drift at the edge.

Table 6-1. Parameter Varied During the Laboratory-Scale Experiment Heating Phase Sensitivity Analyses	
Parameter Varied	**Parameter Values**
Matrix permeability, k_{mat}	± 10 times
Fracture permeability, k_{frac}	± 10 times, ± 100 times
van Genuchten α	1.0×10^{-5}, 1.0×10^{-4}, 1.0×10^{-3}
Area modifier, A_{mod}	0.1, 0.01, 0.001
Fracture-to-matrix relative permeability reduction, η	0.1, 0.01, 0.001
Active fracture model γ	0.2, 0.4, 0.6, 0.8

Table 6-2. Summary of Laboratory-Scale Simulations Indicating Variables Modified from Basecase Values						
Simulation Descriptor	**Variables Modified**					
	A_{mod}	γ	α	η	k_{mat}	k_{frac}
lst155	1.0	—	1×10^{-4}	1.0	1.0	1.0
lst156	1.0	0.4	1×10^{-4}	1.0	1.0	1.0
lst157	0.001	—	1×10^{-4}	1.0	1.0	1.0
lst158	1.0	—	1×10^{-3}	1.0	1.0	1.0
lst159	0.001	—	1×10^{-3}	1.0	1.0	1.0
lst160	1.0	0.4	1×10^{-3}	1.0	1.0	1.0
lst161	0.1	—	1×10^{-4}	1.0	1.0	1.0
lst162	0.1	—	1×10^{-3}	1.0	1.0	1.0
lst163	0.01	—	1×10^{-4}	1.0	1.0	1.0
lst164	0.01	—	1×10^{-3}	1.0	1.0	1.0
lst165	1.0	0.2	1×10^{-4}	1.0	1.0	1.0
lst166	1.0	0.2	1×10^{-3}	1.0	1.0	1.0
lst167	1.0	—	1×10^{-4}	0.001	1.0	1.0
lst168	1.0	—	1×10^{-3}	0.001	1.0	1.0
lst169	1.0	—	1×10^{-4}	0.1	1.0	1.0

Table 6-2. Summary of Laboratory-Scale Simulations Indicating Variables Modified From Basecase Values (continued)						
Simulation Descriptor	Variables Modified					
	A_{mod}	γ	α	η	k_{mat}	k_{frac}
lst170	1.0	—	1×10^{-3}	0.1	1.0	1.0
lst171	1.0	—	1×10^{-4}	0.01	1.0	1.0
lst172	1.0	—	1×10^{-3}	0.01	1.0	1.0
lst173	1.0	—	1×10^{-4}	1.0	-10 times	1.0
lst174	1.0	—	1×10^{-4}	1.0	+10 times	1.0
lst175	1.0	—	1×10^{-4}	1.0	1.0	-100 times
lst176	1.0	—	1×10^{-4}	1.0	1.0	+100 times
lst177*	1.0	—	1×10^{-4}	1.0	1.0	1.0
lst178	1.0	—	1×10^{-4}	1.0	1.0	+10 times
lst179	1.0	—	1×10^{-5}	1.0	1.0	1.0
lst180	1.0	0.4	1×10^{-3}	1.0	-10 times	1.0
lst181	1.0	0.4	1×10^{-3}	1.0	+10 times	1.0
lst182	1.0	0.4	1×10^{-3}	1.0	1.0	-100 times
lst183	1.0	0.4	1×10^{-5}	1.0	1.0	1.0
lst184	1.0	0.6	1×10^{-4}	1.0	1.0	1.0
lst185	1.0	0.8	1×10^{-4}	1.0	1.0	1.0
lst186	1.0	0.4	1×10^{-3}	1.0	1.0	1.0
lst187	1.0	0.4	1×10^{-3}	1.0	1.0	1.0
lst188†	1.0	0.4	1×10^{-3}	1.0	1.0	1.0

*lst177 was simulated with no water source.
†lst188 was simulated with porosity reduced from 0.5 to 0.2.

Table 6-3. Summary of Laboratory-Scale Experiment Sensitivity Analyses: Maximum Matrix and Fracture Saturation and Temperature									
Run No.	Matrix Sat.*	Fracture Sat.	Matrix Temp.† (°C)‡	Fracture Temp. (°C)	Run No.	Matrix Sat.	Fracture Sat.	Matrix Temp. (°C)	Fracture Temp. (°C)
lst155	0.9982	0.179	185.1	184.6	lst172	0.9971	0.1685	186.7	186.2
lst156	0.9982	0.294	185.3	184.8	lst173	1.0000	0.3054	179.8	179.3
lst157	0.9942	0.5796	187.9	143.7	lst174	0.9183	0.0460	187.5	187.0
lst158	0.9986	0.1615	186.8	186.2	lst175	1.0000	0.8505	187.4	186.9
lst159	0.9943	0.1709	188.5	144.6	lst176	0.9945	0.0260	184.7	184.2
lst160	0.9978	0.079	186.8	186.3	lst177	0.4653	0.0449	188.3	187.8
lst161	0.9969	0.3133	185.1	180.6	lst178	0.9954	0.0702	185.0	184.5
lst162	0.9963	0.1697	186.6	182.1	lst179	0.9992	0.2942	185.3	184.8
lst163	0.9947	0.3213	186.3	167.5	lst180	1.0000	0.1457	187.0	186.5
lst164	0.9947	0.1729	187.4	168.6	lst181	0.8340	0.0000	183.6	183.1
lst165	0.9988	0.2399	185.2	184.7	lst182	1.0000	0.5571	187.4	186.8
lst166	0.9982	0.1213	186.8	186.3	lst183	0.9982	0.1792	185.1	184.6
lst167	0.9954	0.3292	185.0	184.5	lst184	0.9969	0.1129	185.0	184.5
lst168	0.9969	0.1695	186.7	186.2	lst185	0.9956	0.0448	185.0	184.5
lst169	0.9982	0.3030	184.9	184.4	lst187	0.9978	0.0795	186.8	186.3
lst170	0.9983	0.1635	186.8	186.2	lst188	0.9979	0.0799	184.2	183.7
lst171	0.9961	0.3240	185.0	184.4	—	—	—	—	—

*Sat.—Saturation
†Temp.—Temperature
‡[1 °F = 9/5 °F + 32]

Simulated matrix saturations were compared with observed saturation features. For comparisons at the mid-plane, neither invoking the active fracture model [Figure 6-3 (lst156)] nor reducing the fracture permeability function, $\eta = 0.001$, [Figure 6-4 (lst167)] effectively replicated high matrix saturation above the heater drift. A reduction in interfacial area provided relatively good simulation of high matrix saturation above the heater drift for an A_{mod} value of either 0.01 [Figure 6-5 (lst163)] or 0.001 [Figure 6-6 (lst157)]. An A_{mod} value of 0.1 resulted in slightly less increase in matrix saturation [Figure 6-7 (lst162)]. The most prominent evidence of an increase in matrix saturation was observed when matrix permeability was reduced by 10 times and with no change in matrix fracture interactions [Figure 6-8 (lst173)].

Matrix saturation observed at the edge plane (Figure 5b) at the conclusion of Test 2 provided a less coherent image than similar measurements at the mid-plane (Figure 5a). Nonetheless, simulations were evaluated relative to their ability to simulate increased saturation above and to the side of the heated drift and decreased saturation below the drift at the edge of the test cell. Most simulations incorrectly simulated increased saturation below the drift. Exceptions to this incorrect simulation were when (i) the A_{mod} was set to 0.001 and the van Genuchten α was

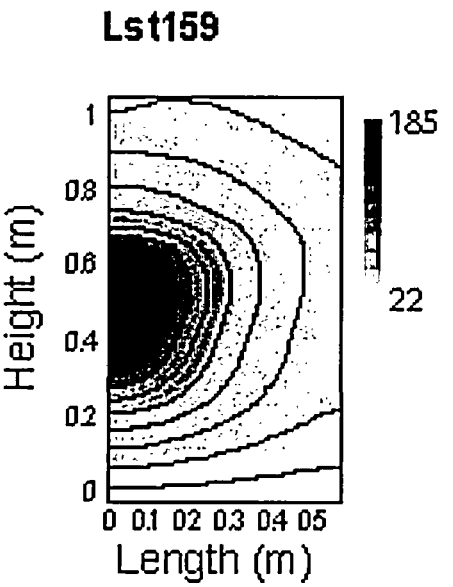

Figure 6-1. Simulated Laboratory-Scale Experiment Temperatures for the Matrix Continuum, Perpendicular to the Heated Drift. Temperature Is Provided in °C. [1 m = 3.28 ft]

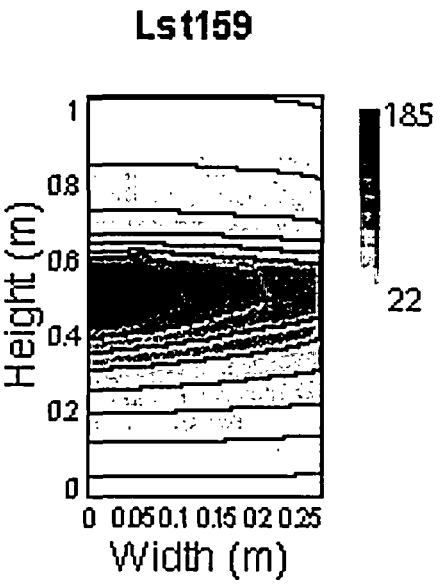

Figure 6-2. Simulated Laboratory-Scale Experiment Temperatures for the Matrix Continuum, Parallel to the Heated Drift. Temperature Is Provided in °C. [1 m = 3.28 ft]

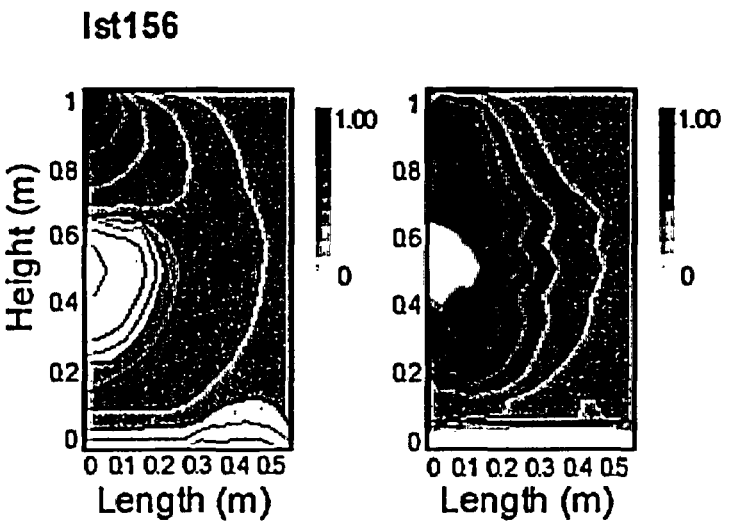

Figure 6-3. Simulated Matrix Saturation for the Mid-Plane (Left) and Edge Plane (Right) of the Laboratory-Scale Experiment with the Active Fracture Model and $\gamma = 0.4$ (lst156) [1 m = 3.28 ft]

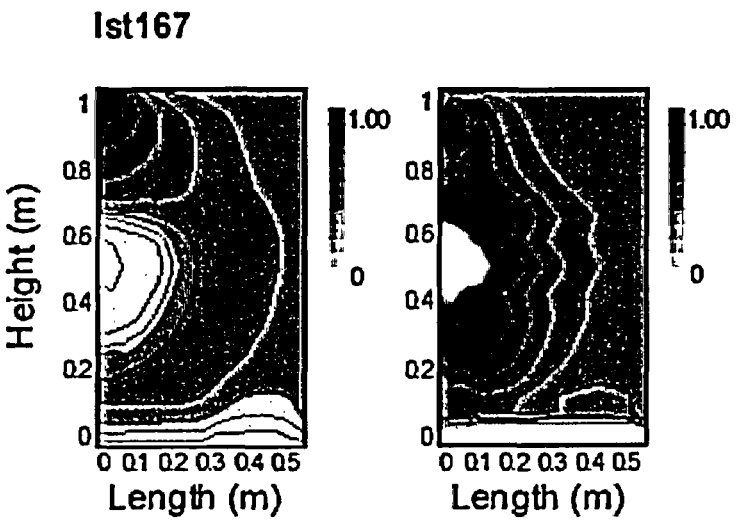

Figure 6-4. Simulated Matrix Saturation for the Mid-Plane (Left) and Edge Plane (Right) of the Laboratory-Scale Experiment with Reduced Fracture Relative Permeability, $\eta = 0.001$ (lst167) [1 m = 3.28 ft]

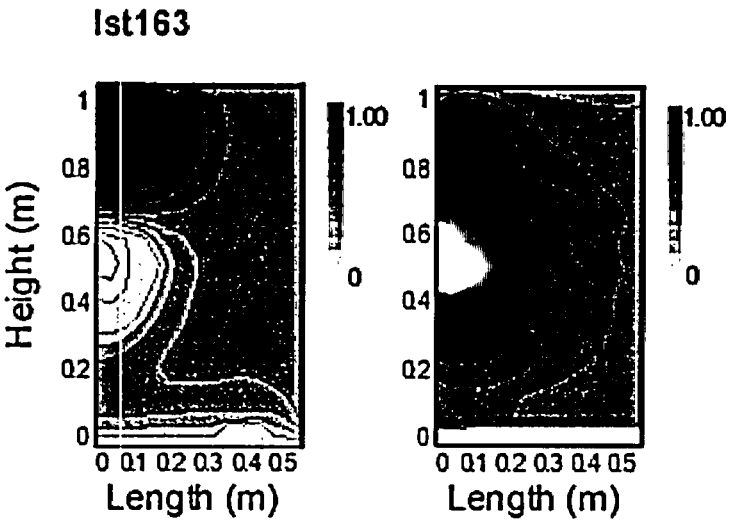

Figure 6-5. Simulated Matrix Saturation for the Mid-Plane (Left) and Edge Plane (Right) of the Laboratory-Scale Experiment with Area Modifier, A_{mod} = 0.01 (lst163) [1 m = 3.28 ft]

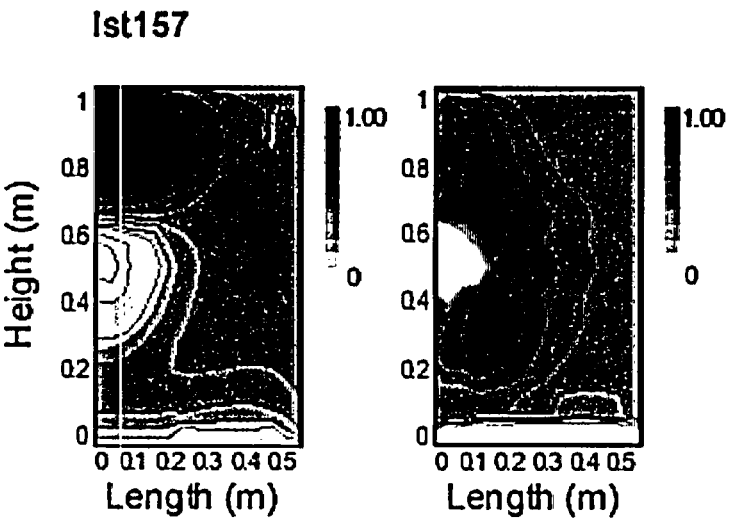

Figure 6-6. Simulated Matrix Saturation for the Mid-Plane (Left) and Edge Plane (Right) of the Laboratory-Scale Experiment with Area Modifier, A_{mod} = 0.01 (lst157) [1 m = 3.28 ft]

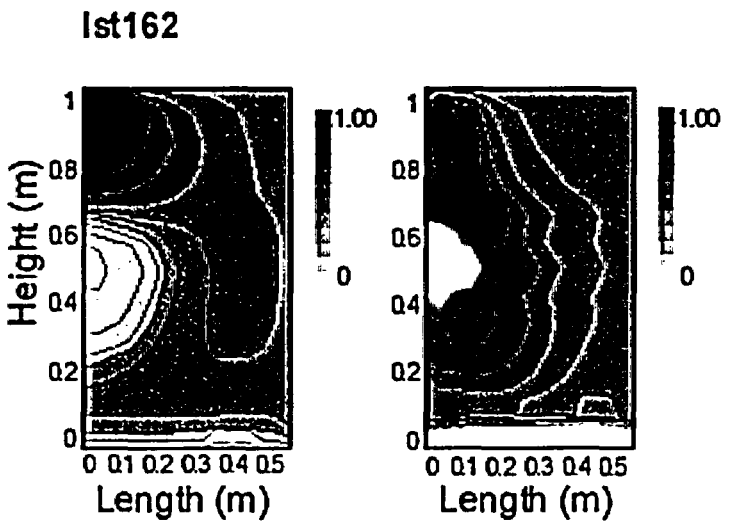

Figure 6-7. Simulated Matrix Saturation for the Mid-Plane (Left) and Edge Plane (Right) of the Laboratory-Scale Experiment with Area Modifier, A_{mod} = 0.1 (lst162) [1 m = 3.28 ft]

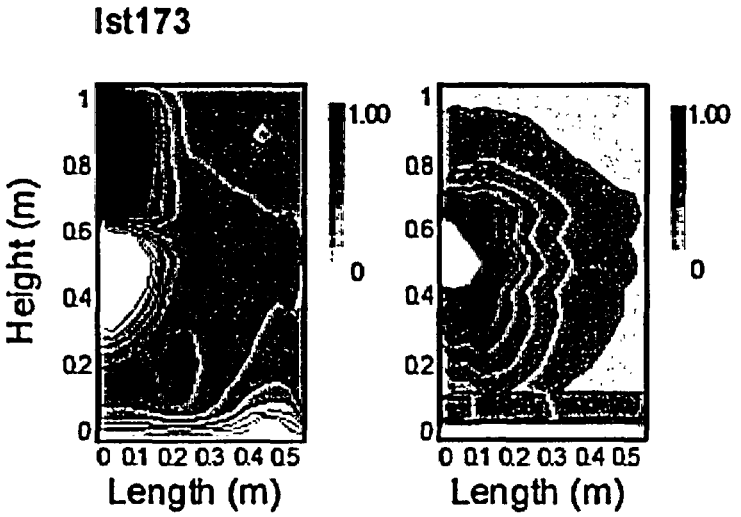

Figure 6-8. Simulated Matrix Saturation for the Mid-Plane (Left) and Edge Plane (Right) of the Laboratory-Scale Experiment with Matrix Permeability Decreased by 10 Times (lst173) [1 m = 3.28 ft]

increased by 10 times [Figure 6-9 (lst159)], (ii) an active fracture model with matrix permeability was decreased by 10 times and the van Genuchten α was increased by 10 times [Figure 6-10 (lst180)], (iii) matrix permeability was decreased by 10 times [Figure 6-11 (lst173)], and (iv) fracture permeability was increased by 100 times [Figure 6-12 (lst176)], although lst176 was not as well established. The consensus of these four simulations suggests that matrix saturation at the edge of the test cell is primarily dependent on some combination of matrix permeability and a small air-entry value associated with the fractures and that the selection of the matrix-fracture conceptual model had secondary importance. This consensus also suggests that most tested models inappropriately indicated that matrix saturation would increase below the heated drift during the heating phase, when, in fact, this process was not corroborated by the test results. Three simulations indicated increased matrix saturation above the drift and decreased saturation below the drift at the edge of the test cell. These tendencies are illustrated in Figure 6-10 (lst180), Figure 6-11 (lst173), and Figure 6-12 (lst176).

Simulated fracture saturations provided a wide range of variability in terms of saturation levels and the nature of the fracture flow. Simulated fracture saturation varied from zero for an active fracture model with matrix permeability increased by 10 times to a fracture saturation as large as 0.85 for fracture permeability decreased by 100 times. Fracture saturation simulations are illustrated as four vertical contour plots oriented perpendicular to the drift. The four plots are located at 0.01, 0.15, 0.23, and 0.25 m [0.033, 0.49, 0.75, and 0.82 ft] relative to the middle of the 0.30-m [1.0-ft] wide test cell. Most simulations demonstrate a consistency among the first three plots with the last plot reflecting the cooling effects of the test-cell side wall.

The primary features of fracture saturation were evidence of (i) vertical penetration into the crown of the drift, (ii) whether fracture flow was focused or diffuse, and (iii) whether there was ponding (i.e., elevated saturation) in the fractures either above or below the heated drift. Active fracture flow or shedding, rather than capillary-dominated flow, was observed in simulations that tended to have smaller values for the van Genuchten α parameter (i.e., $< 1.0 \times 10^{-3}\,Pa^{-1}$) [Figure 6-13 (lst184)] or increased fracture permeability [Figure 6-14 (lst176)]. Simulations that indicated diffuse flow through the fracture continuum [Figure 6-15 (lst163)] were not supported by observations made at the conclusion of Test 1, when the test cell was disassembled and focused flow in the fractures, as evidenced by precipitate deposition on fracture faces, was observed. Choice of conceptual model for matrix-fracture interactions did not appear to be a factor as to whether shedding was observed.

Focused penetration of flow through fractures into the drift crown was observed for a wide range of simulations. Similarities among these simulations were that the van Genuchten α was never as large as $1.0 \times 10^{-3}\,Pa^{-1}$ and that a type of matrix-fracture flow reduction was invoked, although the particular choice of matrix-fracture conceptual model did not seem to matter. The greatest penetration of fracture flow into the drift crown was to a depth of approximately 0.7 m [2.3 ft] in the plots, which extended approximately 0.07 m [0.23 ft] below the top of the drift crown located at 0.77 m, [2.5 ft] was observed in a number of simulations [e.g., Figure 6-13 (lst184)]. However, because the physics of flow into the drift is not accurately incorporated into this model, model results can be used to only indicate that some quantity of water flowed downward via fractures to at least the top of the drift crown.

The presence or absence of fracture flow shedding at the edge of the model (the fourth plot to the right of each fracture saturation plot series) discriminates among the simulations. Simulations that demonstrated diffuse flow in the fractures tended to smear flow throughout the fracture continua, including at the edge of the test cell [Figure 6-15 (lst 163)]. These simulations tended to have a large van Genuchten α parameter (i.e., $1.0 \times 10^{-3}\,Pa^{-1}$).

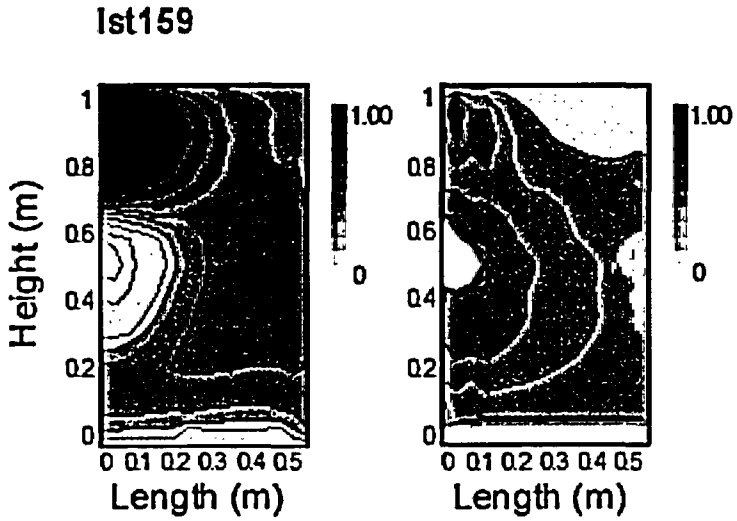

Figure 6-9. Simulated Matrix Saturation for the Mid-Plane (Left) and Edge Plane (Right) of the Laboratory-Scale Experiment with A = 0.001 and the van Genuchten α Increased by 10 Times (lst159) [1 m = 3.28 ft]

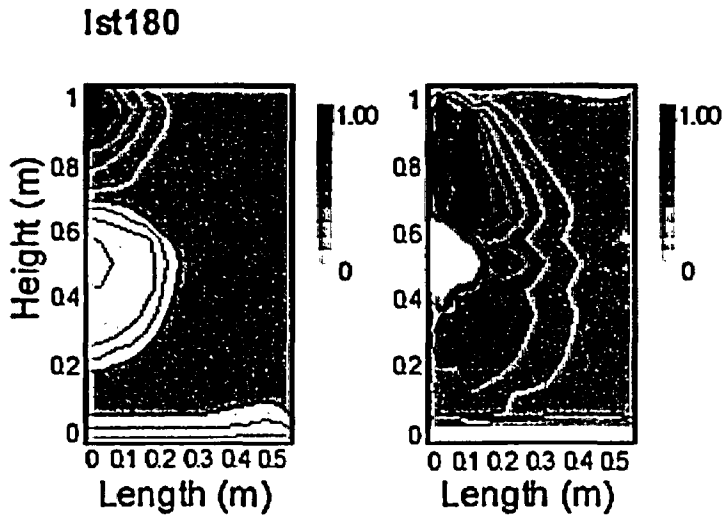

Figure 6-10. Simulated Matrix Saturation for the Mid-Plane (Left) and Edge Plane (Right) of the Laboratory-Scale Experiment with an Active Fracture Model, the van Genuchten α Increased by 10 Times, and with Matrix Permeability Decreased by 10 Times (lst180) [1 m = 3.28 ft]

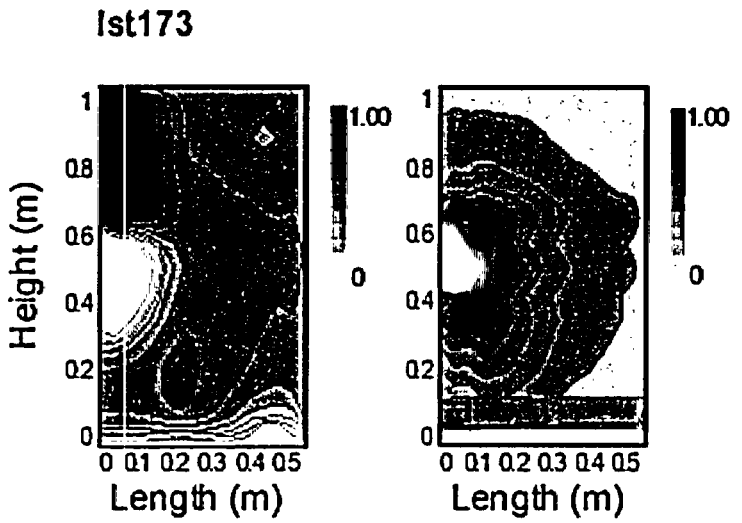

Figure 6-11. Simulated Matrix Saturation for the Mid-Plane (Left) and Edge Plane (Right) of the Laboratory-Scale Experiment with No Active Fracture Model (lst173) [1 m = 3.28 ft]

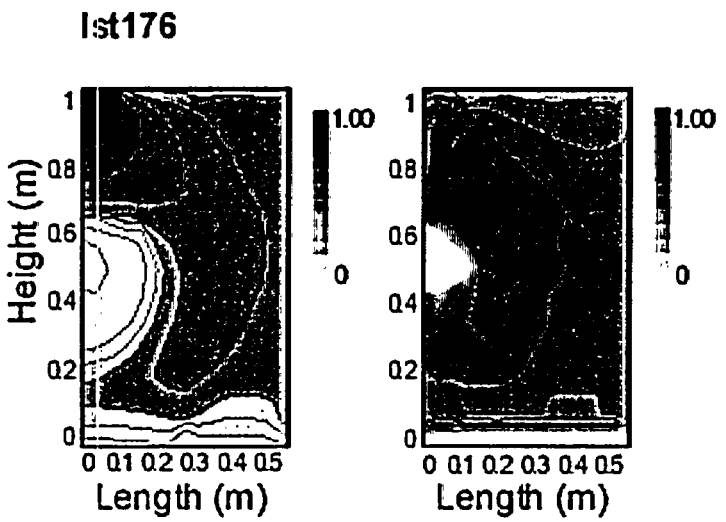

Figure 6-12. Simulated Matrix Saturation for the Mid-Plane (Left) and Edge Plane (Right) of the Laboratory-Scale Experiment with No Active Fracture Model and Fracture Permeability Increased by 100 Times (lst176) [1 m = 3.28 ft]

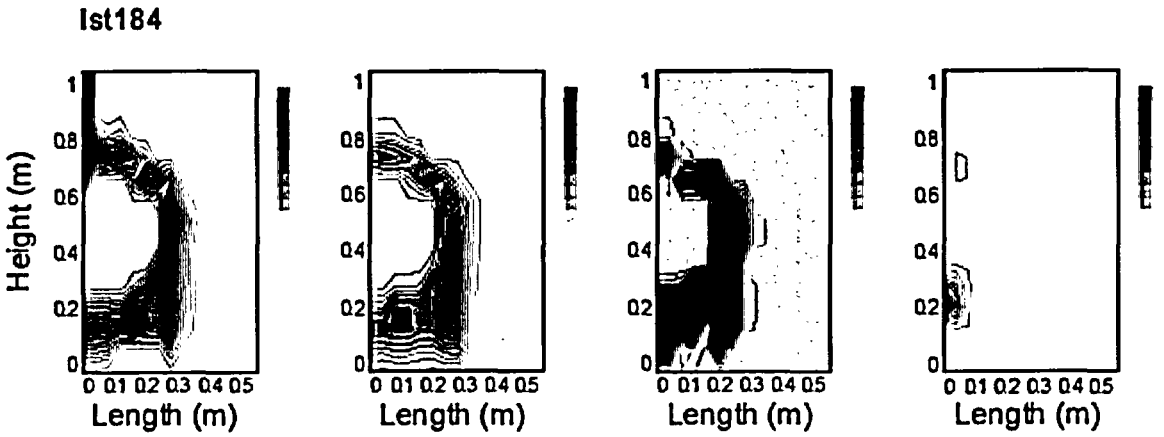

Figure 6-13. Simulated Fracture Saturation for the Laboratory-Scale Experiment at Four Planes Located at 0.01, 0.15, 0.23, and 0.25 m (Left to Right) Relative to the Middle of the 0.30-m Wide Test Cell. Simulation Includes an Active Fracture Model with $\gamma = 0.6$ (lst184). [1 m = 3.28 ft]

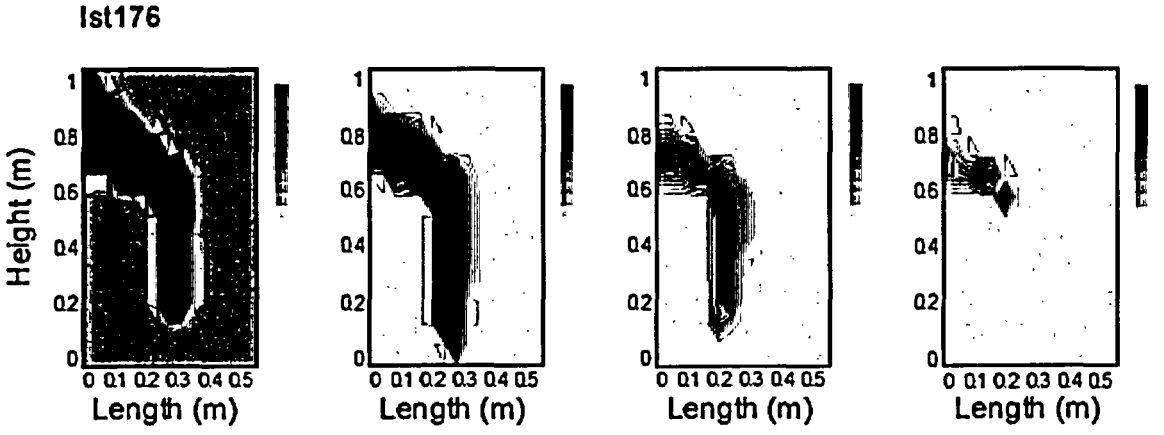

Figure 6-14. Simulated Fracture Saturation for the Laboratory-Scale Experiment at Four Planes Located at 0.01, 0.15, 0.23, and 0.25 m (Left to Right) Relative to the Middle of the 0.30-m Wide Test Cell. Simulation Has No Active Fracture Model and Fracture Permeability Increased by 100 Times (lst176). [1 m = 3.28 ft]

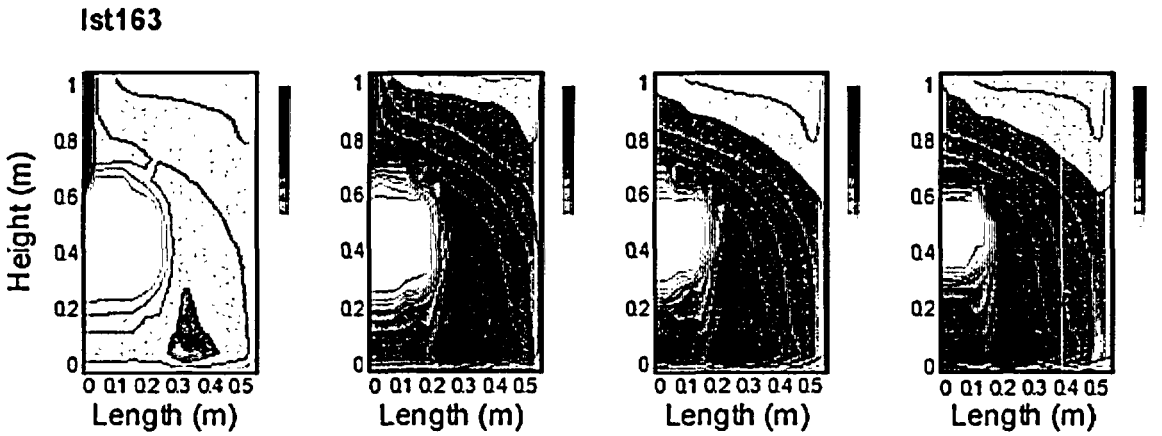

Figure 6-15. Simulated Fracture Saturation for the Laboratory-Scale Experiment at Four Planes Located at 0.01, 0.15, 0.23, and 0.25 m (Left to Right) Relative to the Middle of the 0.30-m Wide Test Cell. Simulation Includes Area Modifier, A_{mod} = 0.01 (lst163). [1 m = 3.28 ft]

6.2 Drift-Scale Heater Test Model Results

An extensive set of analyses (96 simulations) was conducted to evaluate the relationship among infiltration, fracture permeability, and matrix saturation at the field-scale test site under ambient conditions. Infiltration was varied at four values 0.3, 1.0, 3.0, and 10.0 mm/yr [0.012, 0.039, 0.12, and 0.39 in/yr]. Block size was varied at six values 0.2, 0.5, 1.0, 2.0, 5.0, and 10.0 m [0.65, 1.64, 3.8, 16.4, to 32.8 ft] . Fracture permeability was varied by increasing its value by a factor of 10 and decreasing its value by factors of 10 and 100. These values are summarized in Table 6-4. The factors evaluated for the ambient conditions (at a point 8.9 m [29.2 ft] above the center of the drift) analyses are summarized in Table 6-5. Results from these analyses are graphically illustrated in terms of block size versus saturation for different infiltrations in Figures 6-16a through d In general, ambient matrix saturation decreased with an increase up to a block size of 2 m [6.56 ft]. Further increases in block size did not have a noticeable effect on ambient matrix saturation. Increased infiltration obviously resulted in increased ambient saturations although this effect was much more pronounced for decreased fracture permeability. Infiltration rates of 3.0 and 10.0 mm/yr [0.12 and 0.39 in/yr] resulted in full matrix saturation for all block sizes when fracture permeability was decreased by a factor of 100. At increased fracture permeability (i.e., base permeability increased by a factor of 10), there was no significant difference in matrix saturation for infiltration rates increased from 1.0 to 10.0 mm/yr [0.039 to 0.39 in/yr].

Model parameters varied during the heating-phase sensitivity analyses included two parameters evaluated during the ambient conditions sensitivity analyses, namely infiltration and fracture

Table 6-4. Intrinsic Fracture Permeability Values (m^2)			
	tsw33	tsw34	tsw35
Base permeability	8.33×10^{-11} [8.96×10^{-10} ft^2]	2.76×10^{-11} [2.97×10^{-10} ft^2]	1.17×10^{-10} [1.26×10^{-9} ft^2]
Permeability × 10	8.33×10^{-10} [8.96×10^{-9} ft^2]	2.76×10^{-10} [2.97×10^{-9} ft^2]	1.17×10^{-9} [1.26×10^{-8} ft^2]
Permeability ÷ 10	8.33×10^{-12} [8.96×10^{-11} ft^2]	2.76×10^{-12} [2.97×10^{-11} ft^2]	1.17×10^{-11} [1.26×10^{-10} ft^2]
Permeability ÷ 100	8.33×10^{-13} [8.96×10^{-12} ft^2]	2.76×10^{-13} [2.97×10^{-12} ft^2]	1.17×10^{-12} [1.26×10^{-11} ft^2]

Table 6-5. Field-Scale Experiment Ambient Conditions Sensitivity Analyses							
Normal Permeability				Permeability × 10			
Run No.	Block Size (m)*	Saturation	Infiltration (mm/yr)†	Run No.	Block Size (m)*	Saturation	Infiltration (mm/yr)†
2db1	0.2	0.970	0.3	2db1	0.2	0.970	0.3
2db21	0.5	0.969	0.3	2db21	0.5	0.970	0.3
2db2	1	0.967	0.3	2db2	1	0.969	0.3
2db3	2	0.966	0.3	2db3	2	0.969	0.3
2db4	5	0.966	0.3	2db4	5	0.968	0.3
2db5	10	0.966	0.3	2db5	10	0.968	0.3
2db6	0.2	0.983	3	2db6	0.2	0.999	3
2db23	0.5	0.974	3	2db23	0.5	0.999	3
2db7	1	0.970	3	2db7	1	0.999	3
2db8	2	0.969	3	2db8	2	0.999	3
2db9	5	0.968	3	2db9	5	0.999	3
2db10	10	0.968	3	2db10	10	0.999	3
2db11	0.2	0.983	1	2db11	0.2	0.993	1
2db22	0.5	0.973	1	2db22	0.5	0.988	1
2db12	1	0.969	1	2db12	1	0.986	1
2db13	2	0.968	1	2db13	2	0.985	1
2db14	5	0.968	1	2db14	5	0.985	1
2db15	10	0.967	1	2db15	10	0.985	1
2db16	0.2	0.985	10	2db16	0.2	1.000	10
2db17	0.5	0.975	10	2db24	0.5	1.000	10
2db17	1	0.972	10	2db17	1	1.000	10

Table 6-5. Field-Scale Experiment Ambient Conditions Sensitivity Analyses (continued)							
Normal Permeability				Permeability × 10			
Run No.	Block Size (m)*	Saturation	Infiltration (mm/yr)†	Run No.	Block Size (m)*	Saturation	Infiltration (mm/yr)†
2db18	2	0.970	10	2db18	2	1.000	10
2db19	5	0.970	10	2db19	5	1.000	10
2db20	10	0.970	10	2db20	10	—	10
2db1	0.2	0.970	0.3	2db1	0.2	0.970	0.3
2db21	0.5	0.969	0.3	2db21	0.5	0.969	0.3
2db2	1	0.968	0.3	2db2	1	0.967	0.3
2db3	2	0.967	0.3	2db3	2	0.966	0.3
2db4	5	0.966	0.3	2db4	5	0.966	0.3
2db5	10	0.966	0.3	2db5	10	0.966	0.3
2db6	0.2	0.988	3	2db6	0.2	0.982	3
2db23	0.5	0.980	3	2db23	0.5	0.972	3
2db7	1	0.976	3	2db7	1	0.969	3
2db8	2	0.975	3	2db8	2	0.968	3
2db9	5	0.974	3	2db9	5	0.967	3
2db10	10	0.974	3	2db10	10	0.967	3
2db11	0.2	0.984	1	2db11	0.2	0.982	1
2db22	0.5	0.975	1	2db22	0.5	0.972	1
2db12	1	0.971	1	2db12	1	0.969	1
2db13	2	0.970	1	2db13	2	0.968	1
2db14	5	0.969	1	2db14	5	0.967	1
2db15	10	0.969	1	2db15	10	0.967	1
2db16	0.2	0.996	10	2db16	0.2	0.983	10
2db24	0.5	0.993	10	2db24	0.5	0.973	10
2db17	1	0.991	10	2db17	1	0.969	10
2db18	2	0.990	10	2db18	2	0.968	10
2db19	5	0.990	10	2db19	5	0.968	10
2db20	10	0.990	10	2db20	10	0.968	10

*[1 m = 3.28 ft]
†[1 mm/yr = 0.039 in/yr]

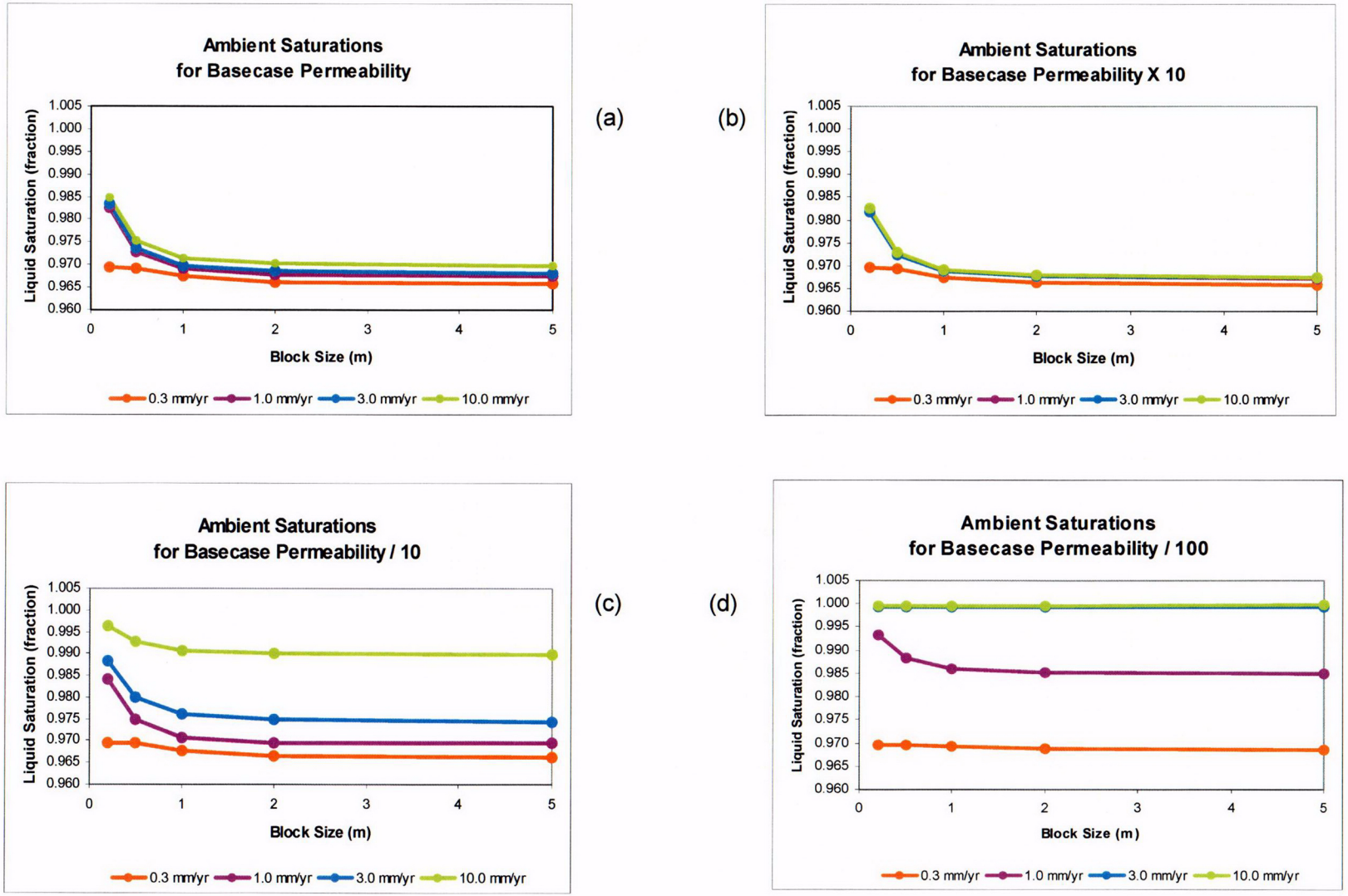

Figure 6-16. Simulated Matrix Saturations for the Field-Scale Experiment Site Under Ambient Conditions. (a) Normal Basecase Fracture Permeability, (b) Permeability Increased by 10 Times, (c) Fracture Permeability Decreased by 10 Times, and (d) Fracture Permeability Decreased by 100 Times. [1 m = 3.28 ft]

C01

permeability, and several others to determine their relative importance. Parameters varied in the heating-phase sensitivity analyses are summarized in Table 6-6. Basecase parameter values for the field-scale heater test are summarized in Table 5-2. With the exception of two simulations in which both fracture permeability and infiltration were varied, all heating phase sensitivity analyses varied only one parameter at a time.

Heat was lost through the thermal bulkhead at the end of the heated drift by conduction, radiation, and convection. Heat loss by convection was accommodated in the field-scale models by the drift-wall boundary condition. Additional heat loss through the bulkhead was implicitly included in the simulations by reducing the heat load imposed at the drift wall by variable amounts (i.e., 10 to 30 percent) to evaluate their potential effect and importance of heat loss by conduction and radiation. Moisture loss through the bulkhead was accommodated by assigning the pressure and allowing saturation to adjust.

Results from the heating-phase sensitivity analyses are graphically presented as contour plots of matrix saturation and temperature and graphs of temperature measured at three boreholes. The three boreholes are 158 (vertically up), 160 (horizontal), and 162 (vertically down) relative to the midpoint of the heated drift. Simulation temperatures are compared with measured temperatures for the same borehole locations. Test results are reported at 3 months, 1 year, and 4 years after the onset of heating. Parameter values varied during these simulations are summarized in Table 6-7. The basecase, identified as simulation ds108, had infiltration of 3.0 mm/yr [0.12 in/yr] and an active fracture model with γ set to 0.41. All other pertinent model properties are defined in Table 5-2.

The maximum temperatures achieved by the simulations are summarized in Table 6-8. Irregardless of differences in maximum temperature, the evolution of matrix temperature as illustrated in contour plots is virtually indistinguishable among the simulations. Matrix temperature contour plots at 3 months, 1 year, and 4 years are presented for the basecase (ds108) in Figure 6-17 as an example. Temperatures contour plots for the other 21 simulations are essentially the same and are included on the attached compact disk as Appendix D. Contour plots for simulated matrix saturation after 3 months, 1 year, and 4 years of heating for all field-scale experiment simulations are included on the attached compact disk as Appendix E. Contour plots for simulated fracture saturation at 3 months, 1 year, and 4 years of heating for all field-scale simulations are included on the attached compact disk as Appendix F. Graphical comparison of simulated and measured temperatures at 3 months, 1 year, and 4 years of heating for Boreholes 158, 160, and 162 are included on the attached compact disk as Appendix G.

The contour plots of simulated matrix saturation demonstrate distinguishable differences, particularly at 1 year of heating. One feature that differentiates the simulations is whether the dryout zone associated with the boiling isotherm completely coalesces the wing heaters and the heated drift at 1 year. Simulation ds127, with the area modifier A_{mod} reduced to 0.001, illustrates the simulation that has the least development of the dryout zone associated with the boiling isotherm (Figure 6-18). Other simulations, ds112 (Figure 6-19) with drift-wall heat reduced by 30 percent and ds124 (Figure 6-20) with the van Genuchten α decreased by 10 times, also demonstrate a decrease in the development of a dryout zone at 1 year of heating. Conversely, ds113 (Figure 6-21), with the matrix permeability increased by 10 times, exhibits the greatest development of a dryout zone at 1 year. Additional simulations that exhibit increased

Table 6-6. Parameters Varied During the Field-Scale Experiment Heating-Phase Sensitivity Analyses	
Parameter Varied	**Parameter Values**
Matrix permeability	+10 times
Infiltration	10.0 mm/yr [0.39 in/yr]
Fracture permeability, infiltration	k/100 at 0.3 mm/yr [0.012 in/yr], k/10 at 1.0 mm/yr [0.39 in/yr]
van Genuchten α	±10 times
Thermal conductivity K_T	-20 percent
Drift wall heat load	-10 percent, -20 percent, -30 percent
Area modifier, A_{mod}	0.1, 0.01, 0.001
Fracture relative permeability η	0.1, 0.01, 0.001
Active fracture model γ	0.2, 0.4, 0.6, 0.8

Table 6-7. Summary of Variables Examined in the Field-Scale Model Sensitivity Analyses	
Simulation Descriptor	**Variables Modified**
ds106	Decreased fracture permeability by 100 times, infiltration at 0.3 mm/yr [0.012 in/yr]
ds107	Decreased fracture permeability by 10 times, infiltration at 1.0 mm/yr [0.039 in/yr]
ds108	Basecase
ds109	Increased infiltration to 10.0 mm/yr [0.39 in/yr]
ds110	Decreased drift-wall heat source by 10 percent
ds111	Decreased drift-wall heat source by 20 percent
ds112	Decreased drift-wall heat source by 30 percent
ds113	Increased matrix permeability by 10 times
ds115	Decreased fracture permeability by 10 times
ds118	Decreased thermal conductivity by 20 percent
ds119	Active fracture model with $\gamma = 0.0$
ds120	Active fracture model with $\gamma = 0.2$
ds121	Active fracture model with $\gamma = 0.6$
ds122	Active fracture model with $\gamma = 0.8$
ds123	Increased van Genuchten α by 10 times
ds124	Decreased van Genuchten α by 10 times
ds125	Set area modifier A_{mod} to 0.1
ds126	Set area modifier A_{mod} to 0.01
ds127	Set area modifier A_{mod} to 0.001
ds128	Decreased fracture relative permeability by 10 times
ds129	Decreased fracture relative permeability by 100 times
ds130	Decreased fracture relative permeability by 1,000 times

Table 6-8. Maximum Temperature, Fracture Saturation, and Matrix Saturation Observed During Simulations of the Field-Scale Experiment									
Run No.	Temperature (°C)*			Fracture Saturation			Matrix Saturation		
	3 months	1 year	4 years	3 months	1 year	4 years	3 months	1 year	4 years
ds106	123.3	196.4	308.8	0.1900	1.0000	0.9587	0.9973	1.0000	0.9999
ds107	122.4	194.6	308.2	0.1683	0.7149	0.3586	0.9996	1.0000	0.9982
ds108	122.2	193.8	305.0	0.0861	0.1771	0.1446	0.9993	0.9996	0.9963
ds109	121.9	193.4	304.3	0.0952	0.1794	0.1478	0.9994	0.9996	0.9969
ds110	122.2	184.8	290.0	0.0862	0.1736	0.1424	0.9993	0.9996	0.9962
ds111	122.1	184.3	275.1	0.0859	0.1699	0.1380	0.9993	0.9996	0.9960
ds112	122.1	183.7	265.8	0.0856	0.1697	0.1327	0.9992	0.9996	0.9958
ds113	119.8	198.0	308.8	0.1256	0.1842	0.1449	0.9529	0.9545	1.0000
ds115	122.1	194.3	307.8	0.1943	0.7242	0.3650	0.9997	1.0000	0.9989
ds118	135.3	218.4	352.5	0.1094	0.1756	0.1406	0.9996	0.9995	0.9963
ds119	121.7	193.2	304.1	0.1776	0.2940	0.2528	0.9989	0.9994	0.9971
ds120	122.2	196.4	304.9	0.1311	1.0000	0.2007	0.9992	1.0000	0.9965
ds121	122.2	193.8	305.0	0.0493	0.1177	0.0921	0.9993	0.9997	0.9960
ds122	122.7	194.0	304.9	0.0196	0.0532	0.0651	0.9976	0.9998	0.9957
ds123	123.2	197.4	310.8	0.0920	0.1727	0.1361	0.9337	0.9426	0.9341
ds124	122.4	187.8	299.8	0.1007	0.1804	0.1477	1.0000	0.9988	0.9970
ds125	124.6	193.9	301.5	0.0459	0.1341	0.1233	0.9483	0.9651	0.9546
ds126	126.5	194.6	298.8	0.0461	0.0749	0.0908	0.8481	0.9021	0.8962
ds127	128.6	198.2	300.4	0.0435	0.0471	0.0594	0.7462	0.8266	0.9463
ds128	122.1	193.7	304.8	0.0909	0.1775	0.1448	0.9993	0.9996	0.9972
ds129	122.2	193.6	305.0	0.0864	0.1771	0.1447	0.9993	0.9996	0.9963
ds130	122.2	193.8	305.0	0.0857	1.0000	0.1447	0.9993	0.9996	0.9961
*[1 °F = 9/5 °F + 32]									

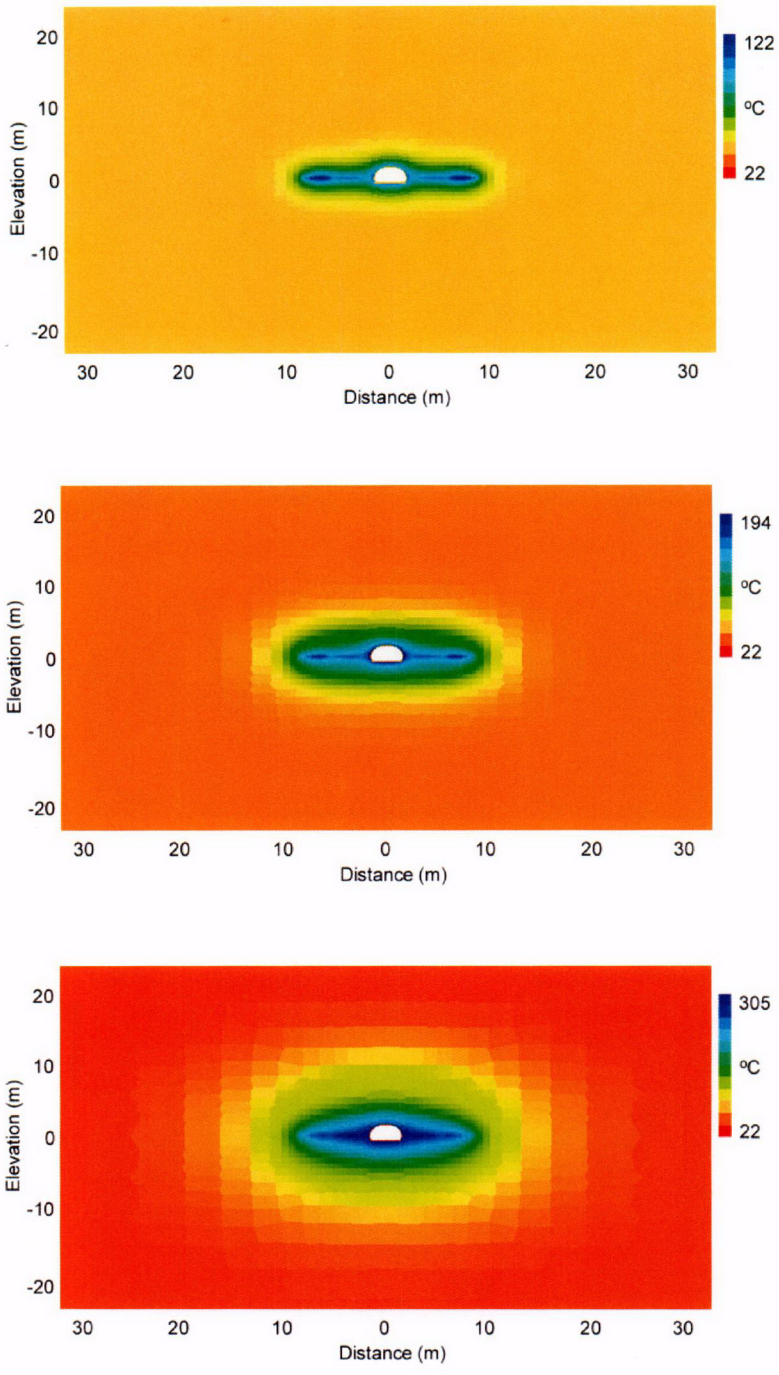

Figure 6-17. Contour Plot of Simulated Matrix Temperature for the Field-Scale Experiment After 3 Months (Top), 1 Year (Middle), and 4 years (Bottom) of Heating. This Plot Is Representative of All Field-Scale Experiment Simulations. Temperature Is Provided in °C. [1 m = 3.28 ft]

C02

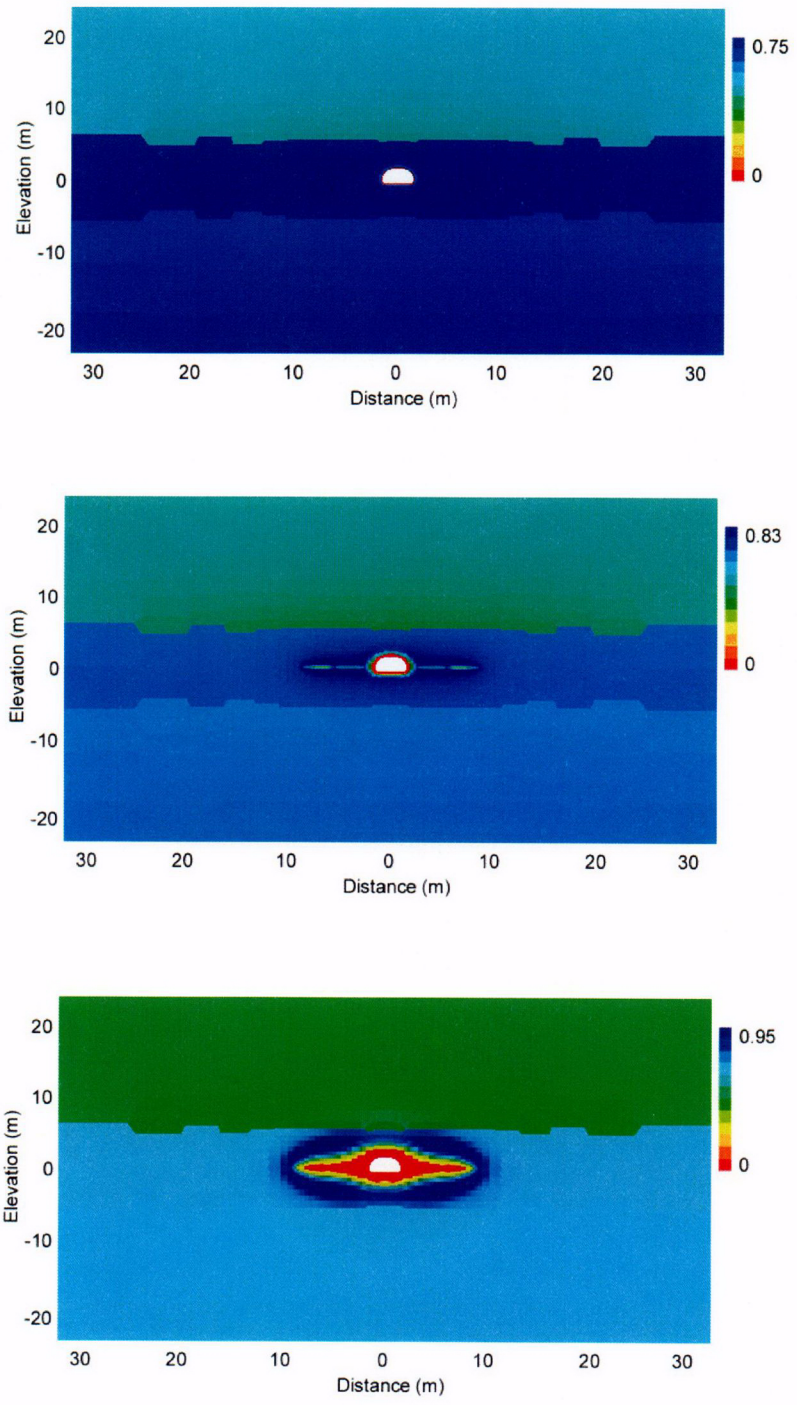

Figure 6-18. Contour Plot of Simulated Matrix Temperature for the Field-Scale Experiment with A_{mod} = 0.001 (ds127) After 3 Months (Top), 1 Year (Middle), and 4 Years (Bottom) of Heating [1 m = 3.28 ft]

C03

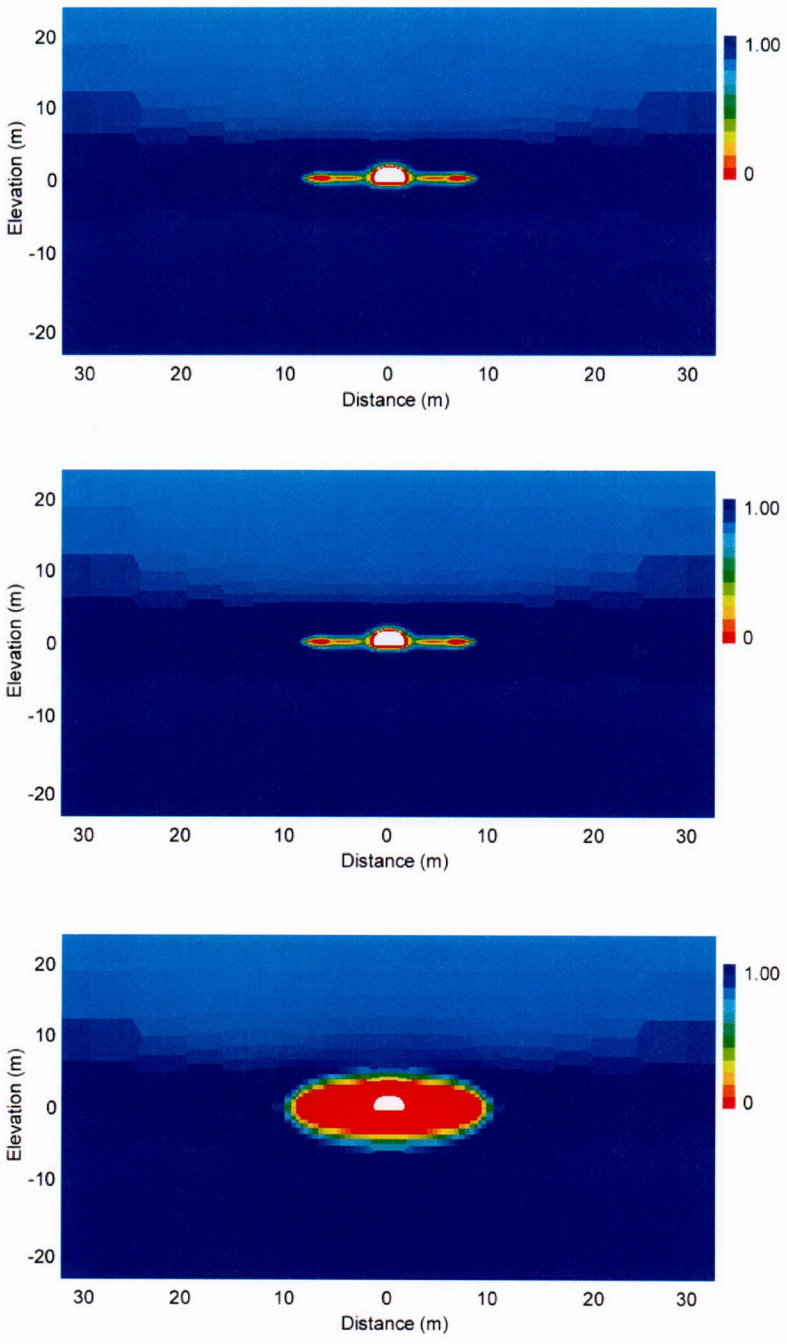

Figure 6-19. Contour Plot of Simulated Matrix Saturation for the Field-Scale Experiment with Drift-Wall Heat Source Reduced by 30 Percent (ds112) After 3 Months (Top), 1 Year (Middle), and 4 Years (Bottom) of Heating [1 m = 3.28 ft]

C04

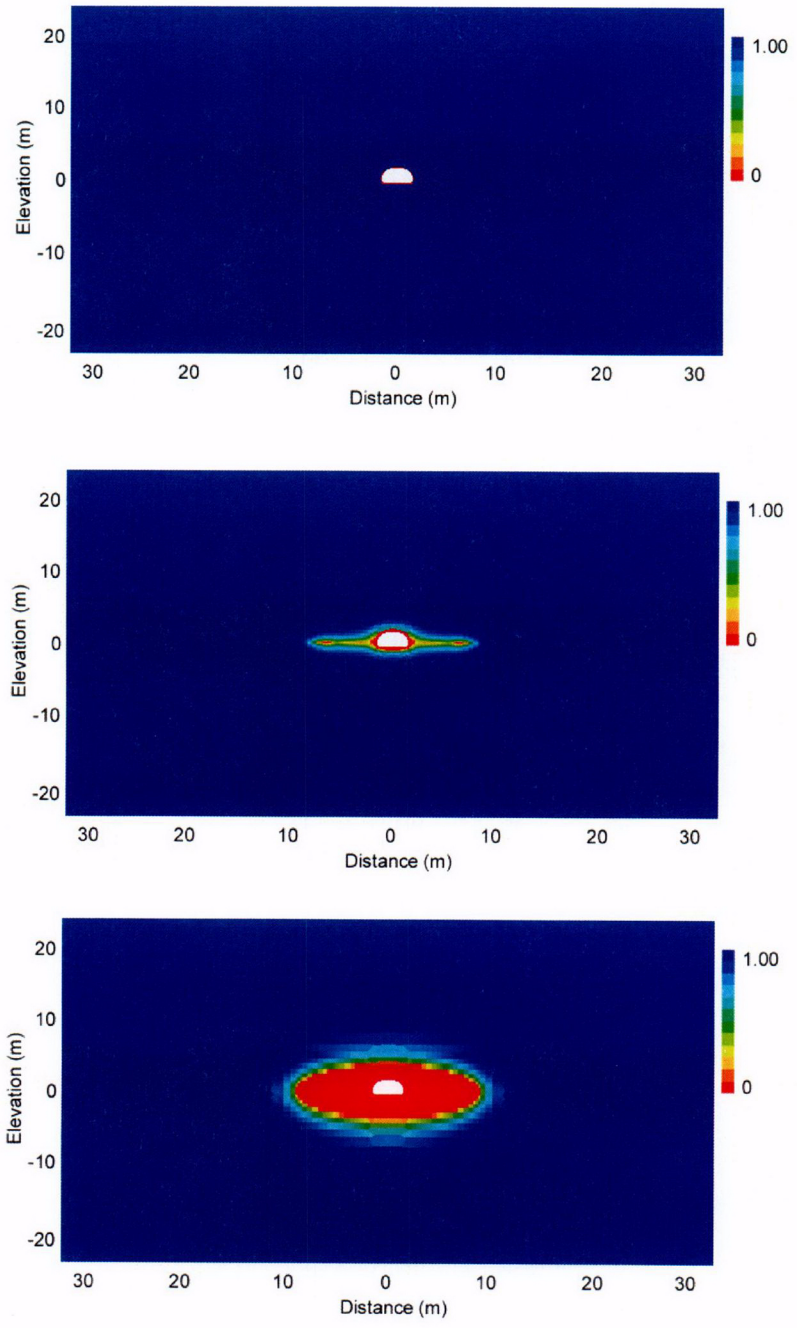

Figure 6-20. Contour Plot of Simulated Matrix Saturation for the Field-Scale Experiment with the van Genuchten α Decreased by 10 Times (ds124) After 3 Months (Top), 1 Year (Middle), and 4 Years (Bottom) of Heating [1 m = 3.28 ft]

C05

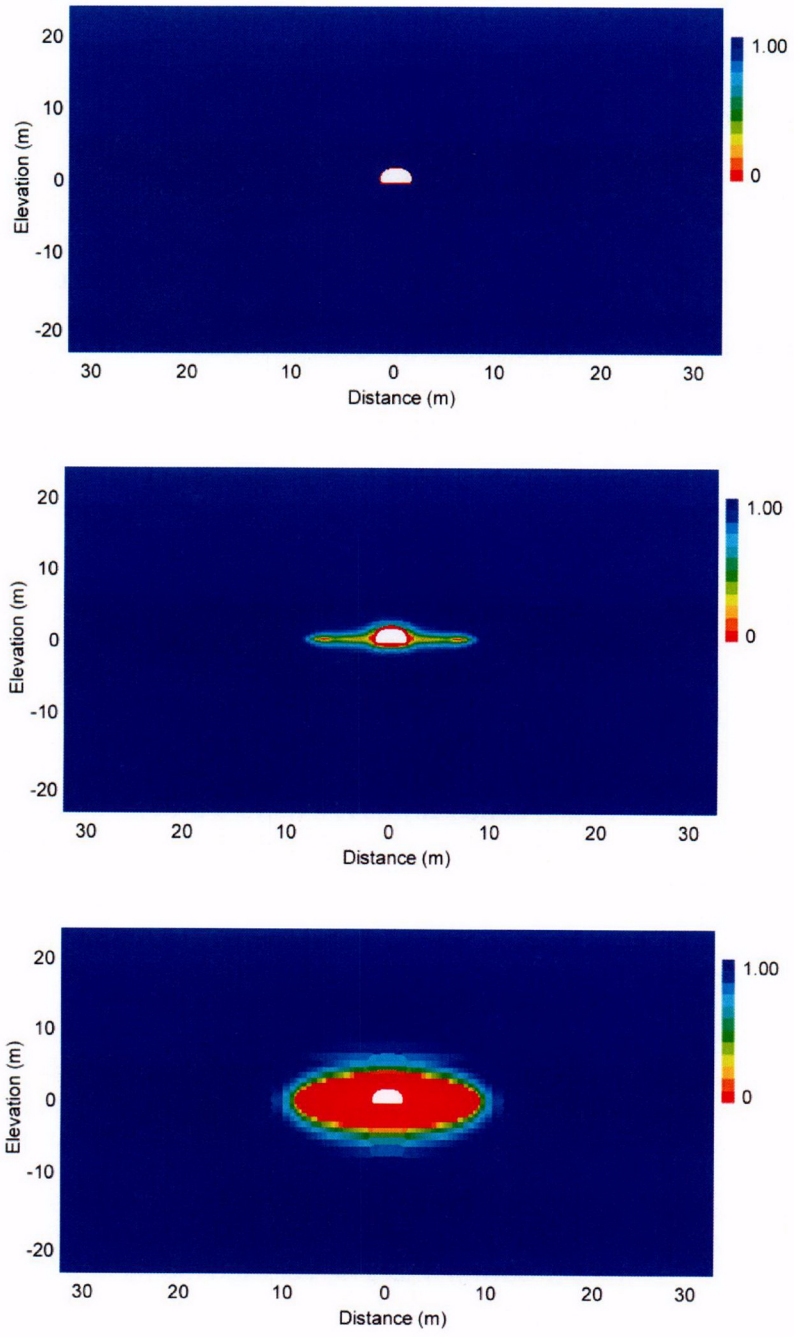

Figure 6-21. Contour Plot of Simulated Matrix Saturation for the Field-Scale Experiment with Matrix Permeability Increased by 10 Times (ds113) After 3 Months (Top), 1 Year (Middle), and 4 Years (Bottom) of Heating [1 m = 3.28 ft]

C06

development of the dryout zone are ds118 (Figure 6-22), with thermal conductivity decreased by 20 percent, and ds123 (Figure 6-23), with the van Genuchten α increased by 10 times.

There were greater differences in simulated fracture saturations than either matrix temperature or saturation. These differences in fracture flow are noteworthy because of the importance of liquid flow into emplacement drifts and the potential for this flow to occur as fracture flow. All simulations, however, demonstrated some level of similarity in the evolution of fracture flow. All demonstrated dryout around the heaters, which started as segmented dryout zones at 3 months and coalesced into one large dryout zone at 1 year of heating. Another similarity in fracture flow was that increased saturation first appeared beneath the wing heaters within 3 months of the onset on heating. In most simulations, elevated saturated was exhibited below the wing heaters approximately to the depth of the tsw34/tsw35 contact, approximately 6 m [19.4 ft] below the wing heaters. Exceptions to this were where the zone of increased fracture saturation did not reach the interface when infiltration was reduced [ds106 (Figure 6-24) and ds107 (Figure 6-25)]. Conversely, the zone of increased fracture saturation penetrated beyond the tsw34/tsw35 interface when matrix permeability was increased [Figure 6-26 (ds113)], thermal conductivity was decreased [ds118 (Figure 6-27)], the active fracture model γ was increased [ds121 (Figure 6-28) and ds122 (Figure 6-29)], or the van Genuchten α was decreased [ds124 (Figure 6-30)].

The simulations demonstrated a similarity in the manner water was shed off the sides of the boiling isotherm and the dryout zones. This shedding was apparent in all simulations at 1 year after heating started, although the degree to which saturation and drainage increased below the test horizon varied significantly. Reduced drainage below the test horizon was experienced when infiltration was decreased [ds106 (Figure 6-24) and ds107 (Figure 6-25)], the active fracture model γ was decreased [ds120 (Figure 6-31)], or when the area modifier A_{mod} was decreased [ds126 (Figure 6-32) and especially ds127 (Figure 6-33)]. Most simulations demonstrated a prominent thin layer of increased saturation immediately above the dryout zone and a less prominent layer of increased saturation immediately below the dryout zone. The zone of increased saturation below the dryout zone was most prominent at 1 year of heating and less prominent at 4 years of heating, although the size of the zone of increased fracture saturation was expanded and better defined at 4 years compared with at 1 year of heating. In addition, although the layer of increased saturation below the dryout zone was less defined than the layer above, the lower layer transitioned into a broad, extensive zone of increased saturation that continued downward for some distance. Both the upper and lower zones of increased fracture saturation are of potential interest because they could lead to increased flow of water into the drift from above and increased solute transport from the drift through fractures below.

The ability of the simulations to replicate the observed temperatures is more easily evaluated using graphical comparisons of temperature measured in Boreholes 158 (vertically up), 160 (horizontal), and 162 (vertically down). Plots for selected matrix and fracture temperature are compared with measured temperatures at 3 months, 1 year, and 4 years after the onset of heating. Matrix- and fracture-simulated temperatures are the same except when the area modifier was less than 1.0. Plots of temperature at the three boreholes for the basecase, ds108, are illustrated in Figure 6-34. Several key features are apparent. The simulation was more successful in matching temperatures away from the heated drift than near it. This closer simulation was particularly true in Borehole 160, oriented horizontally above the wing heaters with simulated temperatures considerably greater than those observed.

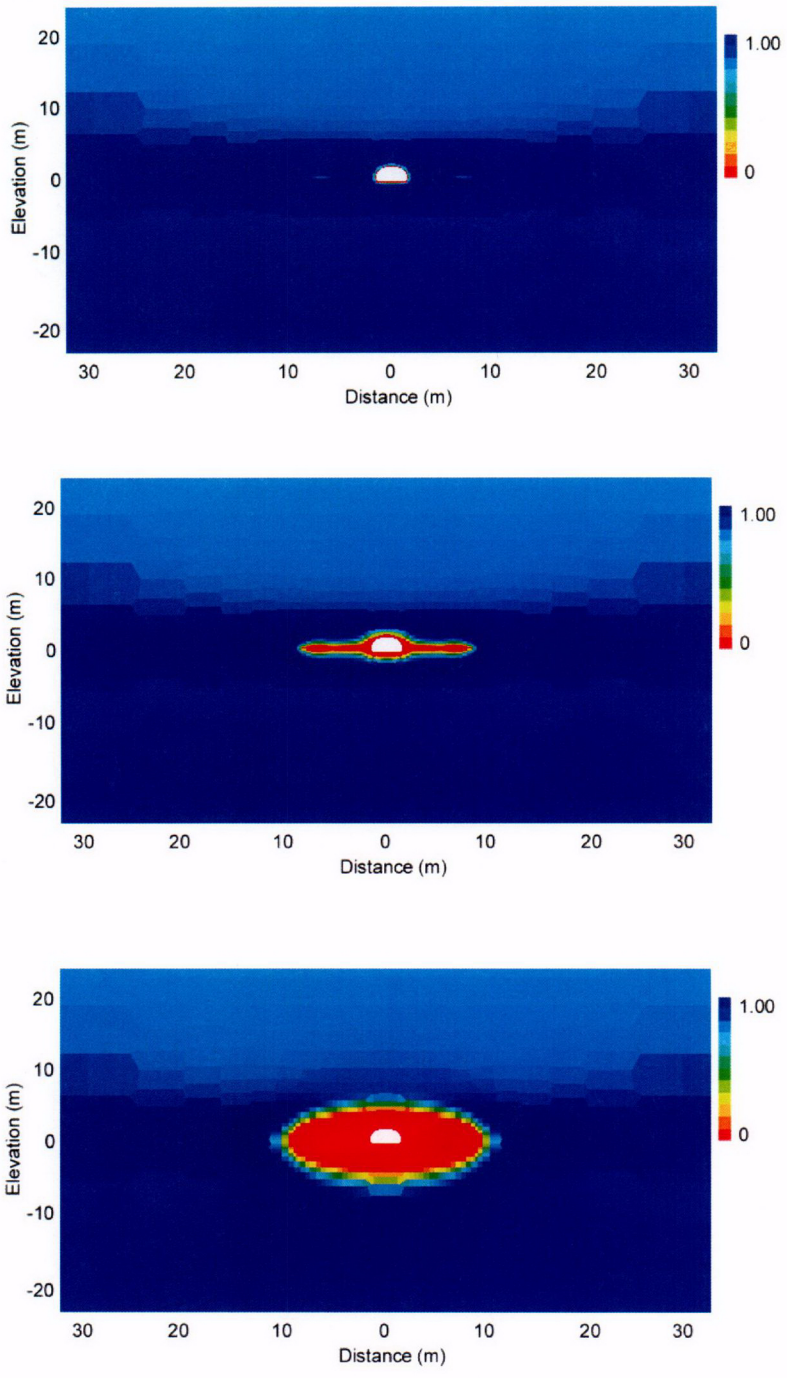

Figure 6-22. Contour Plot of Simulated Matrix Saturation for the Field-Scale Experiment with Thermal Conductivity Decreased by 20 Percent (ds118) After 3 Months (Top), 1 Year (Middle), and 4 Years (Bottom) of Heating [1 m = 3.28 ft]

C07

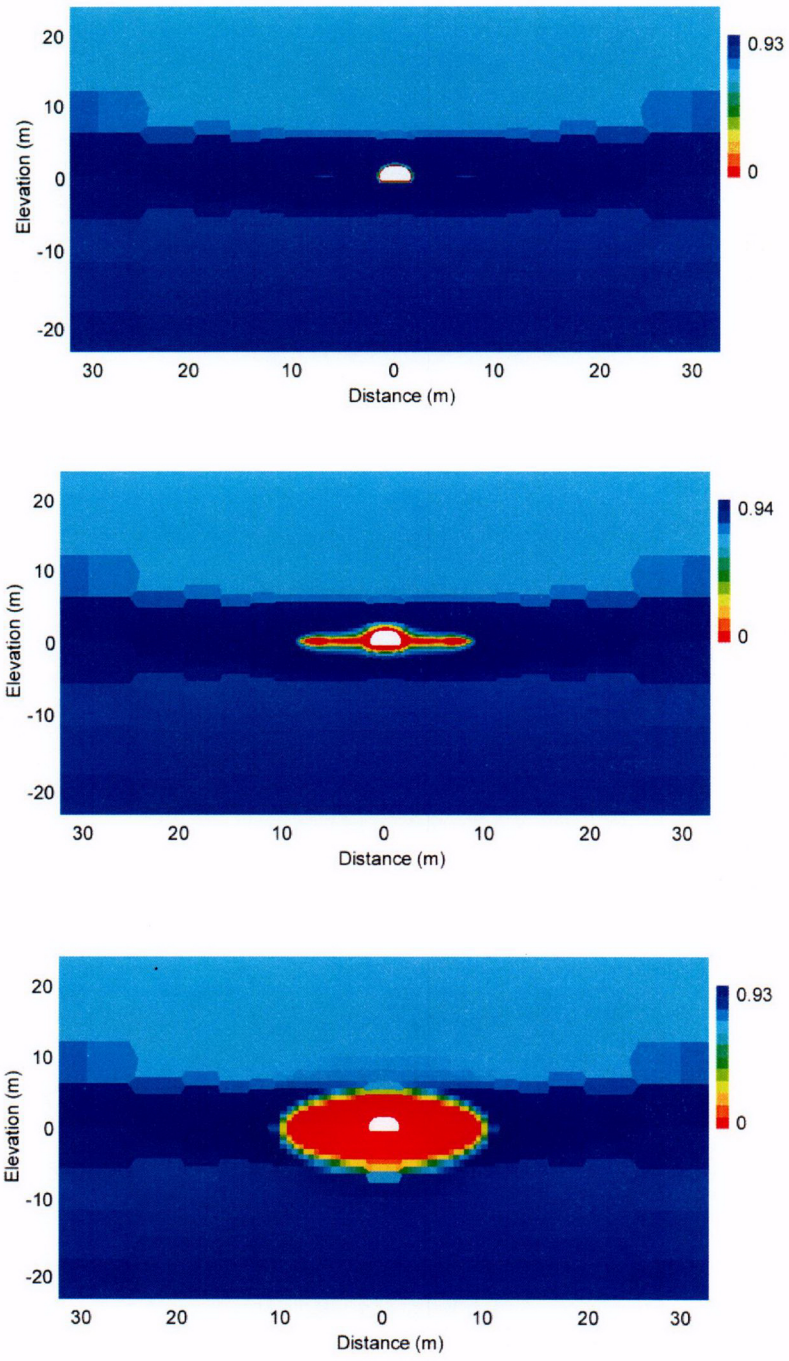

Figure 6-23. Contour Plot of Simulated Matrix Saturation for the Field-Scale Experiment with A_{mod} = 0.1 (ds123) After 3 Months (Top), 1 Year (Middle), and 4 Years (Bottom) of Heating [1 m = 3.28 ft]

C08

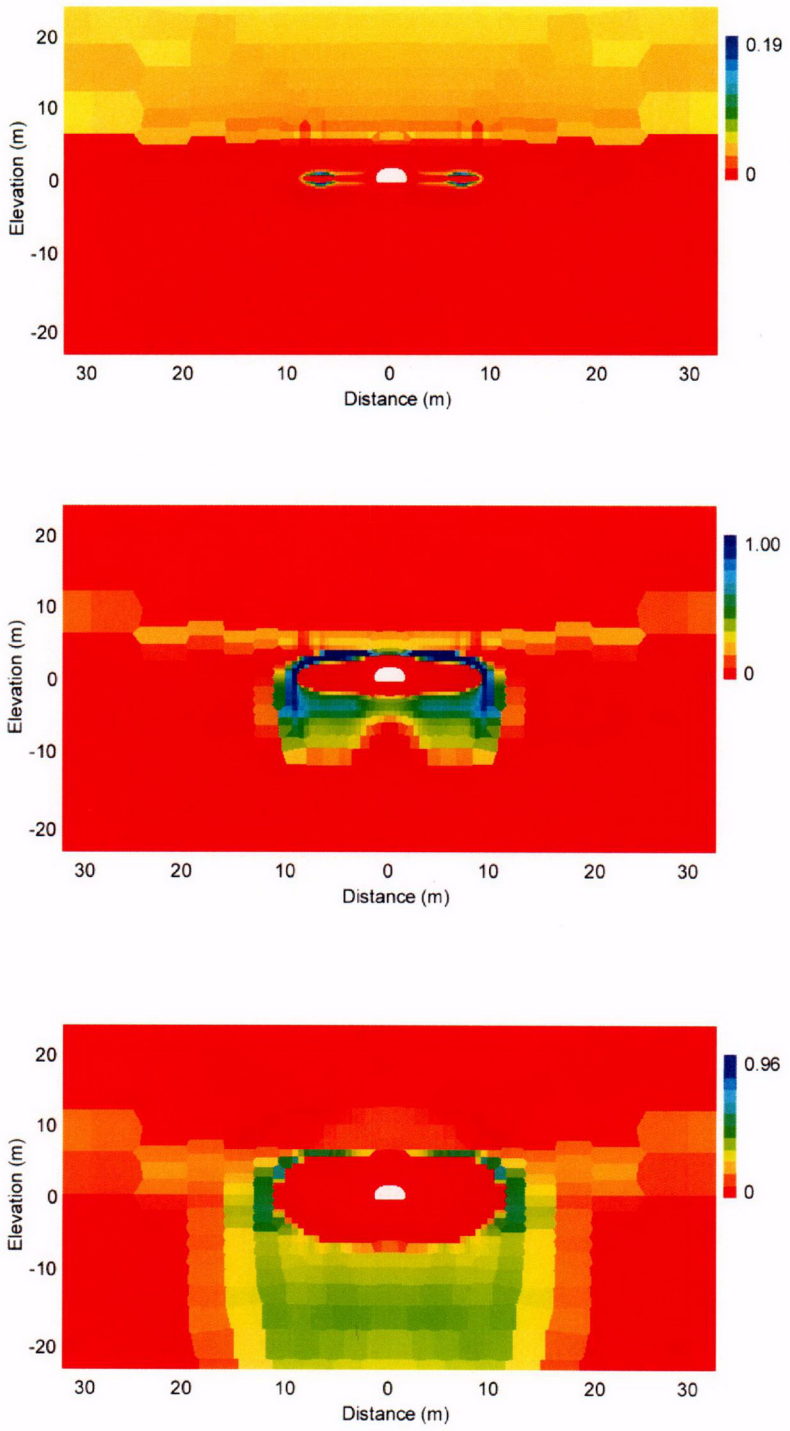

Figure 6-24. Contour Plot of Simulated Fracture Saturation for the Field-Scale Experiment with Fracture Permeability Decreased by 100 Times and Infiltration Decreased to 0.3 mm/yr [0.01181 in/yr] (ds106) after 3 Months (Top), 1 Year (Middle), and 4 Years (Bottom) of Heating [1 m = 3.28 ft]

C09

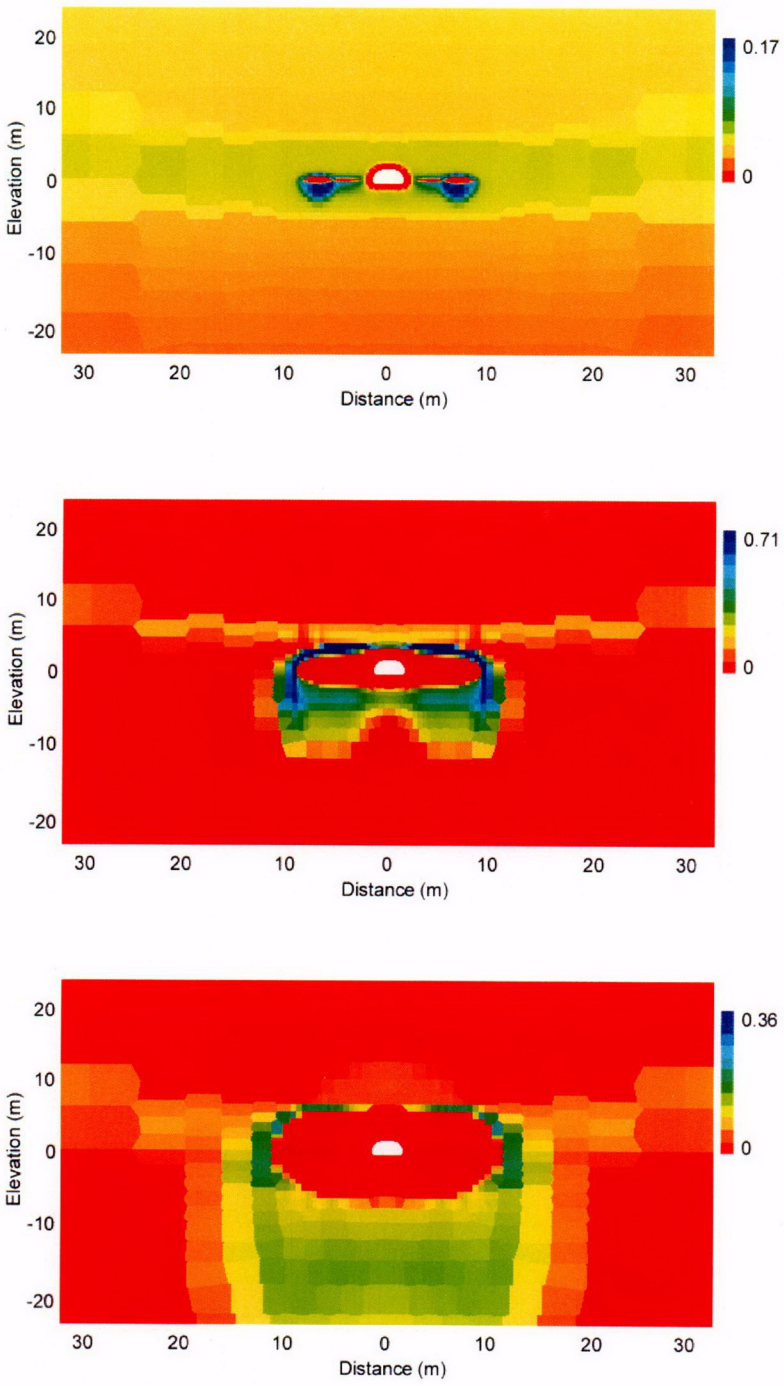

Figure 6-25. Contour Plot of Simulated Fracture Saturation for the Field-Scale Experiment with Fracture Permeability Decreased by 10 Times and Infiltration Decreased by 1.0 mm/yr [0.03937 in/yr] (ds107) after 3 Months (Top), 1 Year (Middle), and 4 Years (Bottom) of Heating [1 m = 3.28 ft]

C10

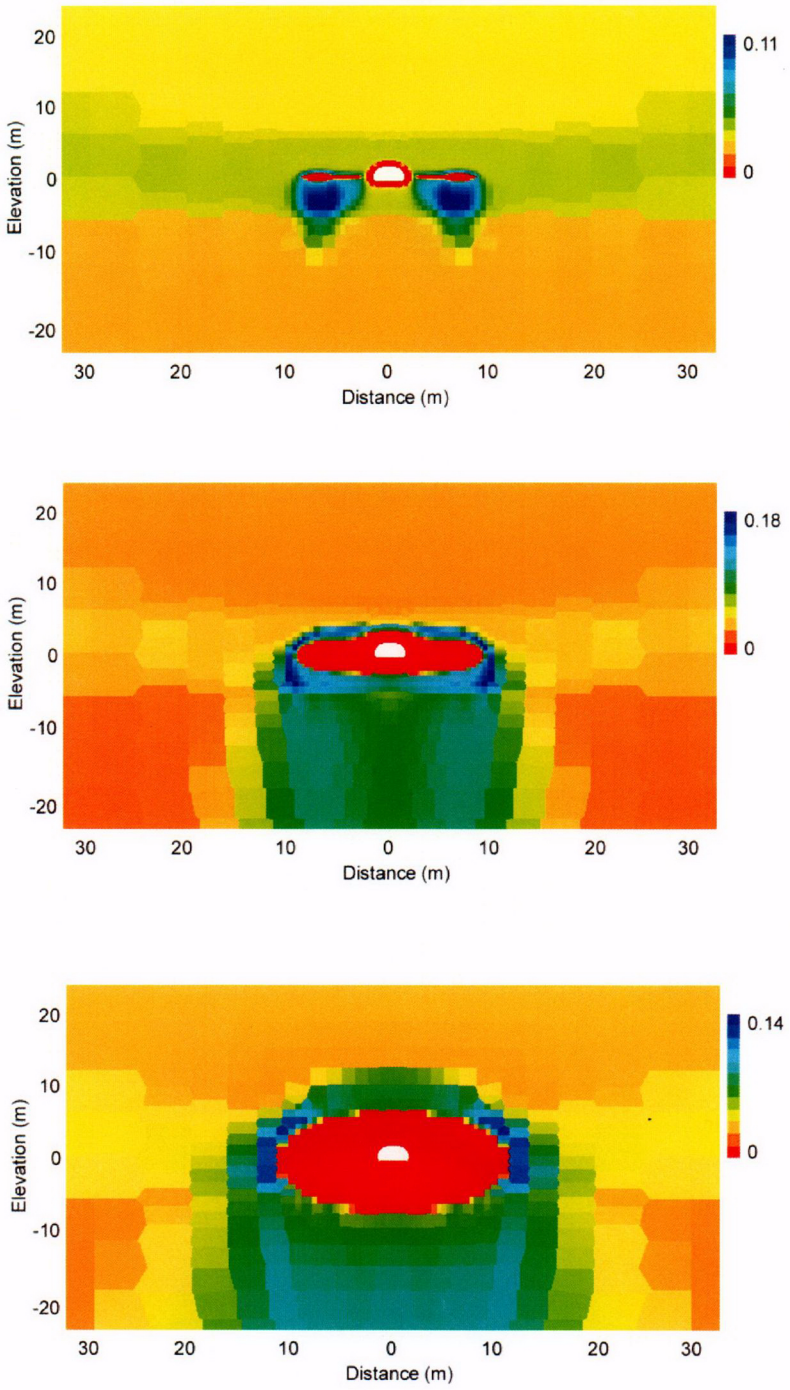

Figure 6-26. Contour Plot of Simulated Fracture Saturation for the Field-Scale Experiment with Matrix Permeability Increased by 10 Times (ds113) after 3 Months (Top), 1 Year (Middle), and 4 Years (Bottom) of Heating [1 m = 3.28 ft]

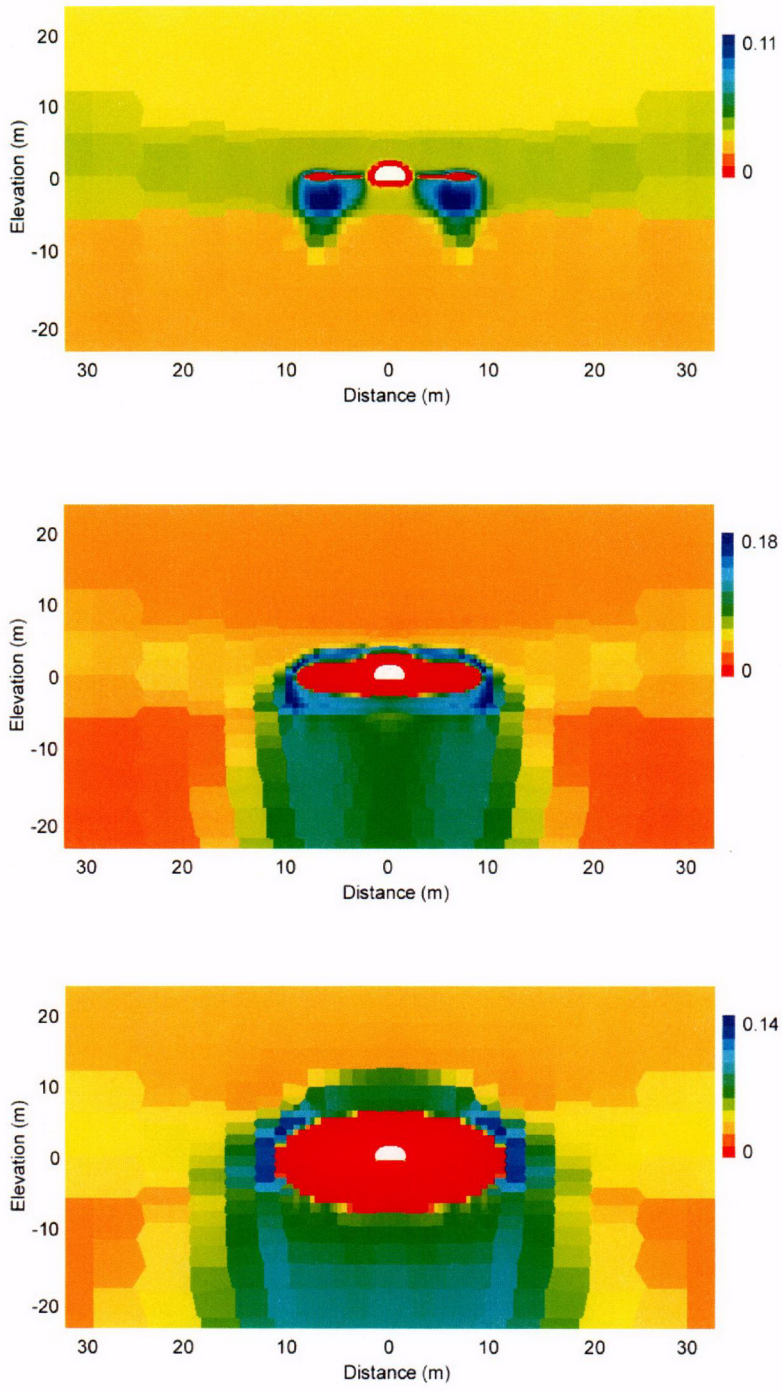

Figure 6-27. Contour Plot of Simulated Fracture Saturation for the Field-Scale Experiment with Thermal Conductivity Decreased by 10 Times (ds118) after 3 Months (Top), 1 Year (Middle), and 4 Years (Bottom) of Heating [1 m = 3.28 ft]

C12

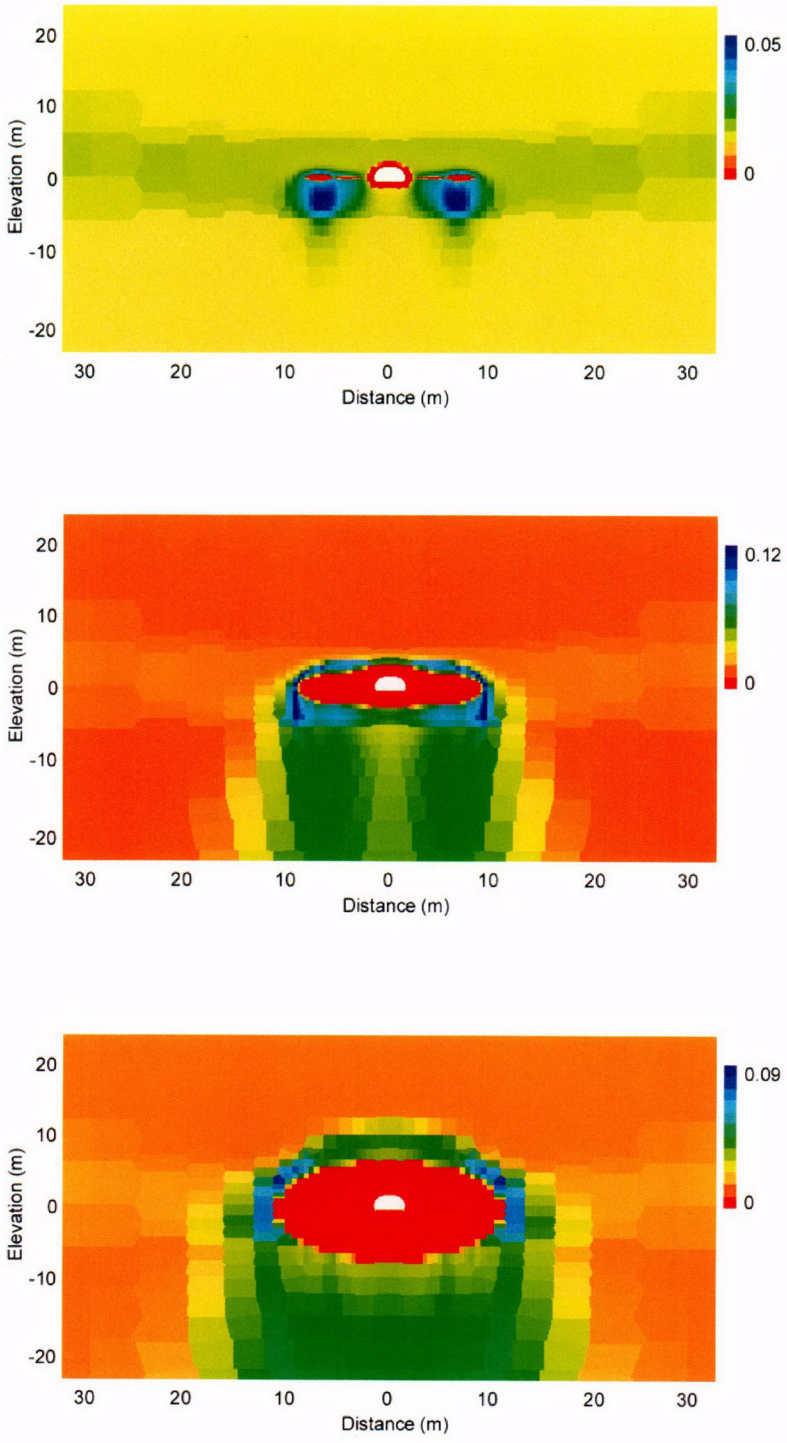

Figure 6-28. Contour Plot of Simulated Fracture Saturation for the Field-Scale Experiment with the Active Fracture Model γ = 0.6 (ds121) after 3 Months (Top), 1 Year (Middle), and 4 Years (Bottom) of Heating [1 m = 3.28 ft]

C13

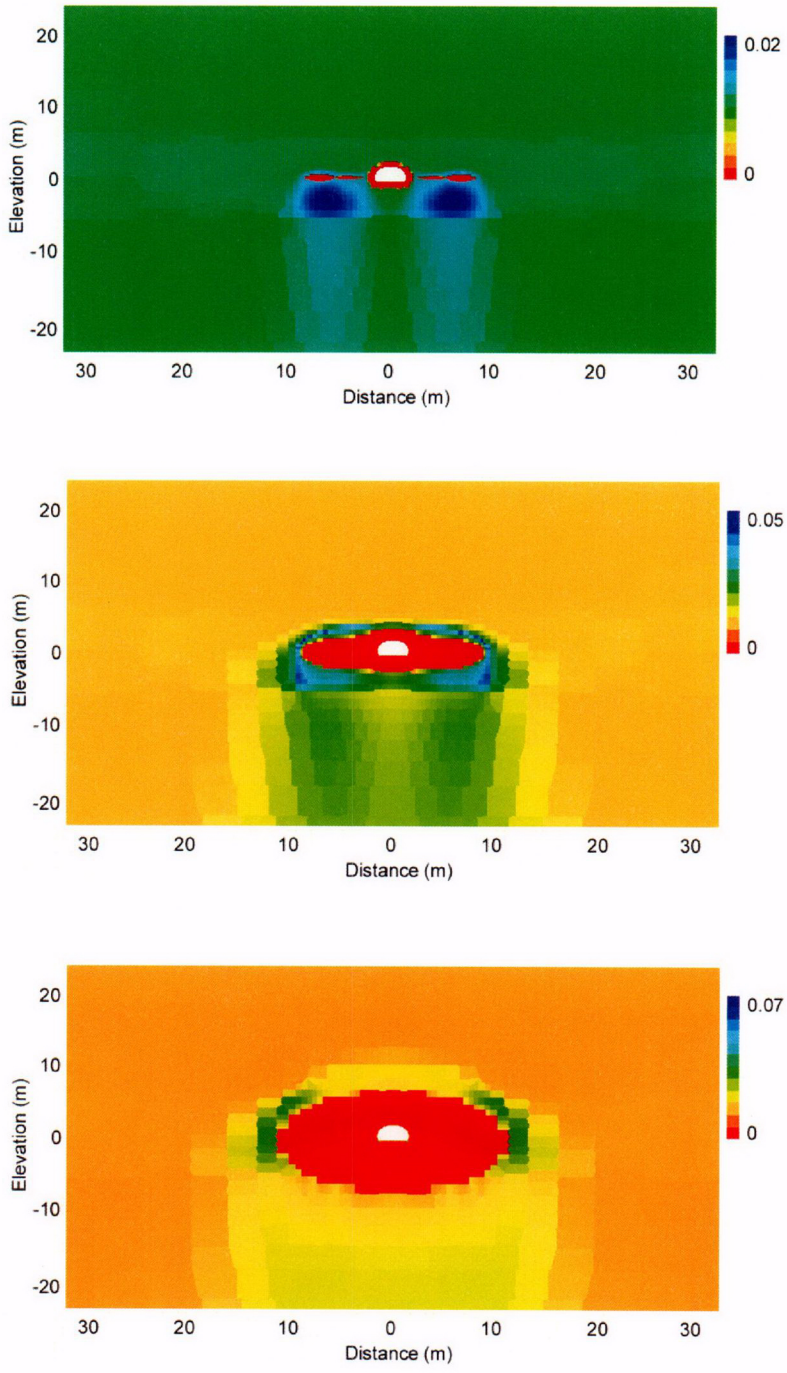

Figure 6-29. Contour Plot of Simulated Fracture Saturation for the Field-Scale Experiment with the Active Fracture Model γ = 0.8 (ds122) after 3 Months (Top), 1 Year (Middle), and 4 Years (Bottom) of Heating [1 m = 3.28 ft]

C14

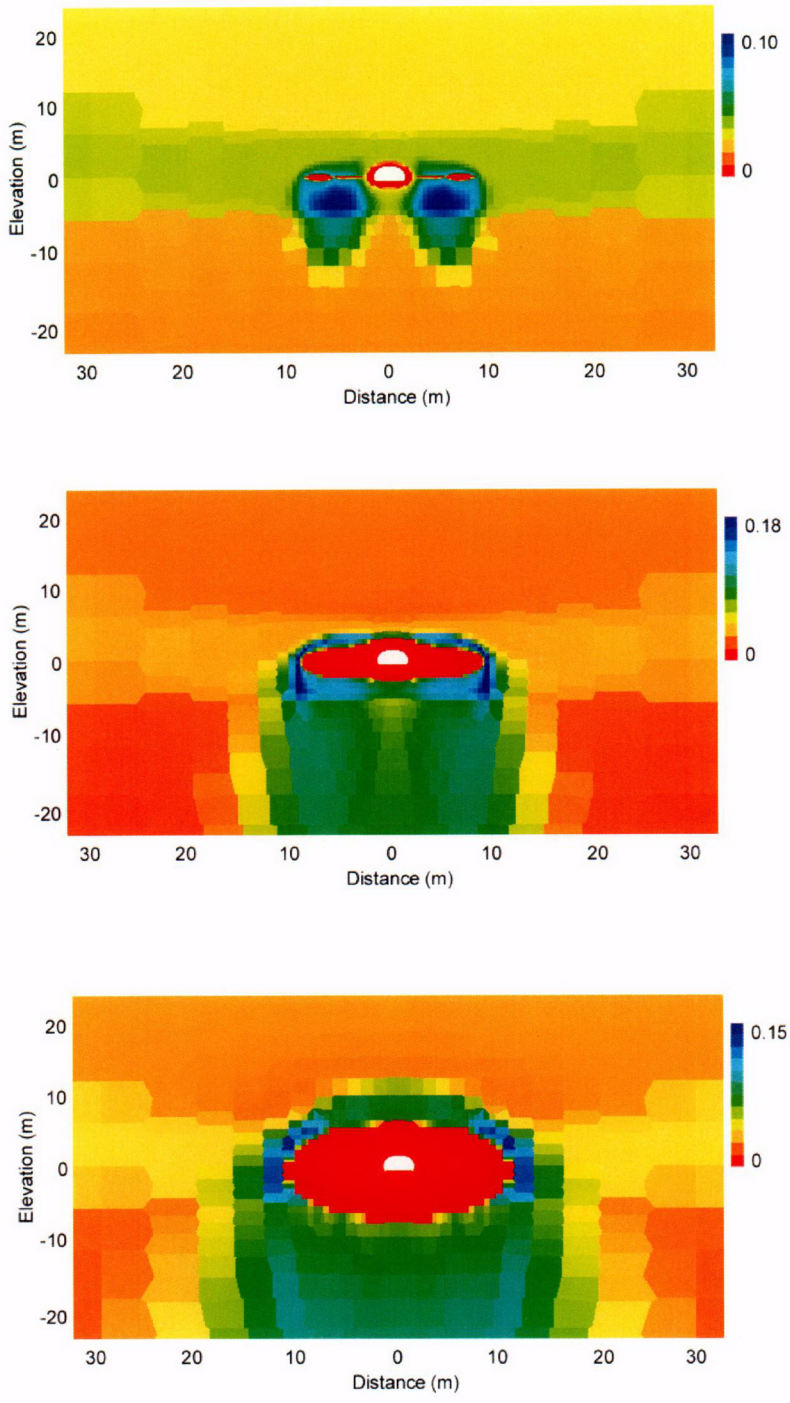

Figure 6-30. Contour Plot of Simulated Fracture Saturation for the Field-Scale Experiment with the van Genuchten α Decreased by 10 Times (ds124) after 3 Months (Top), 1 Year (Middle), and 4 Years (Bottom) of Heating [1 m = 3.28 ft]

C15

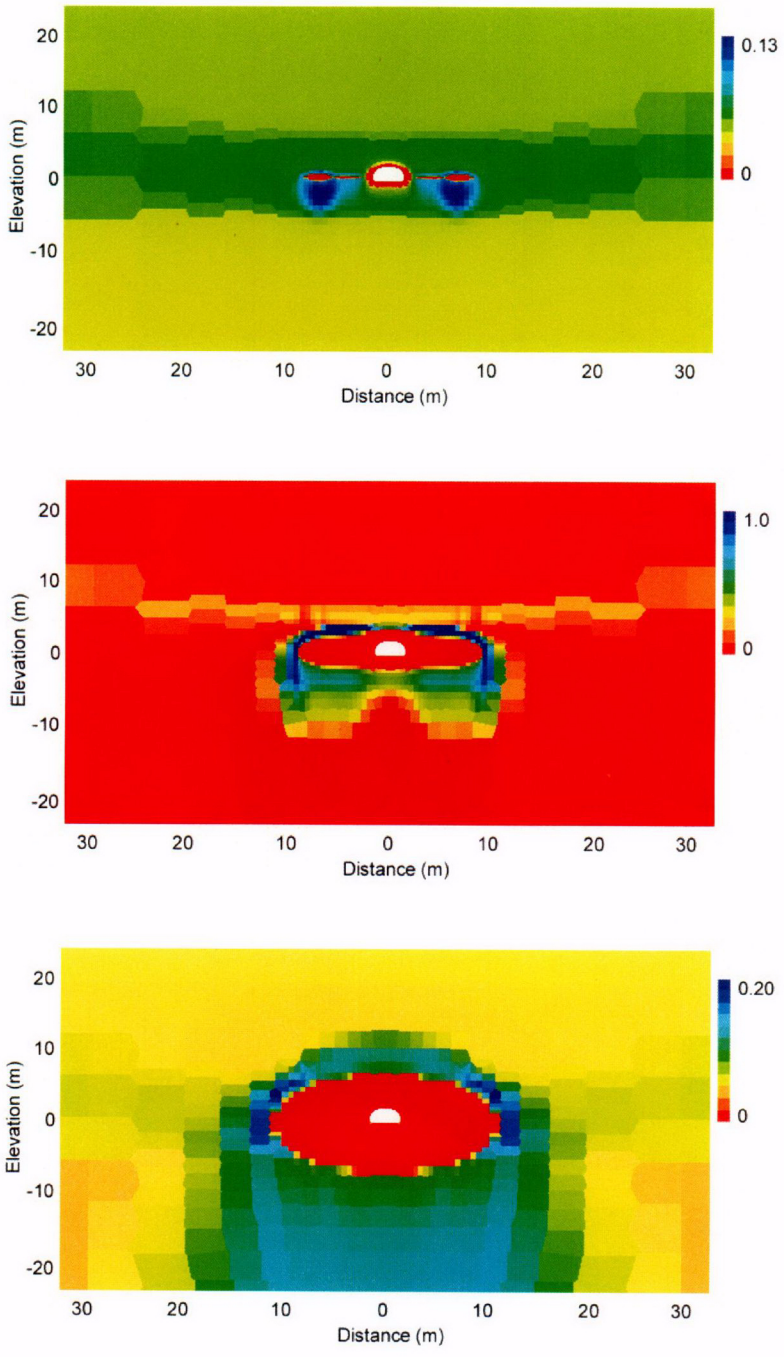

Figure 6-31. Contour Plot of Simulated Fracture Saturation for the Field-Scale Experiment with the Active Fracture Model γ = 0.2 (ds120) after 3 Months (Top), 1 Year (Middle), and 4 Years (Bottom) of Heating [1 m = 3.28 ft]

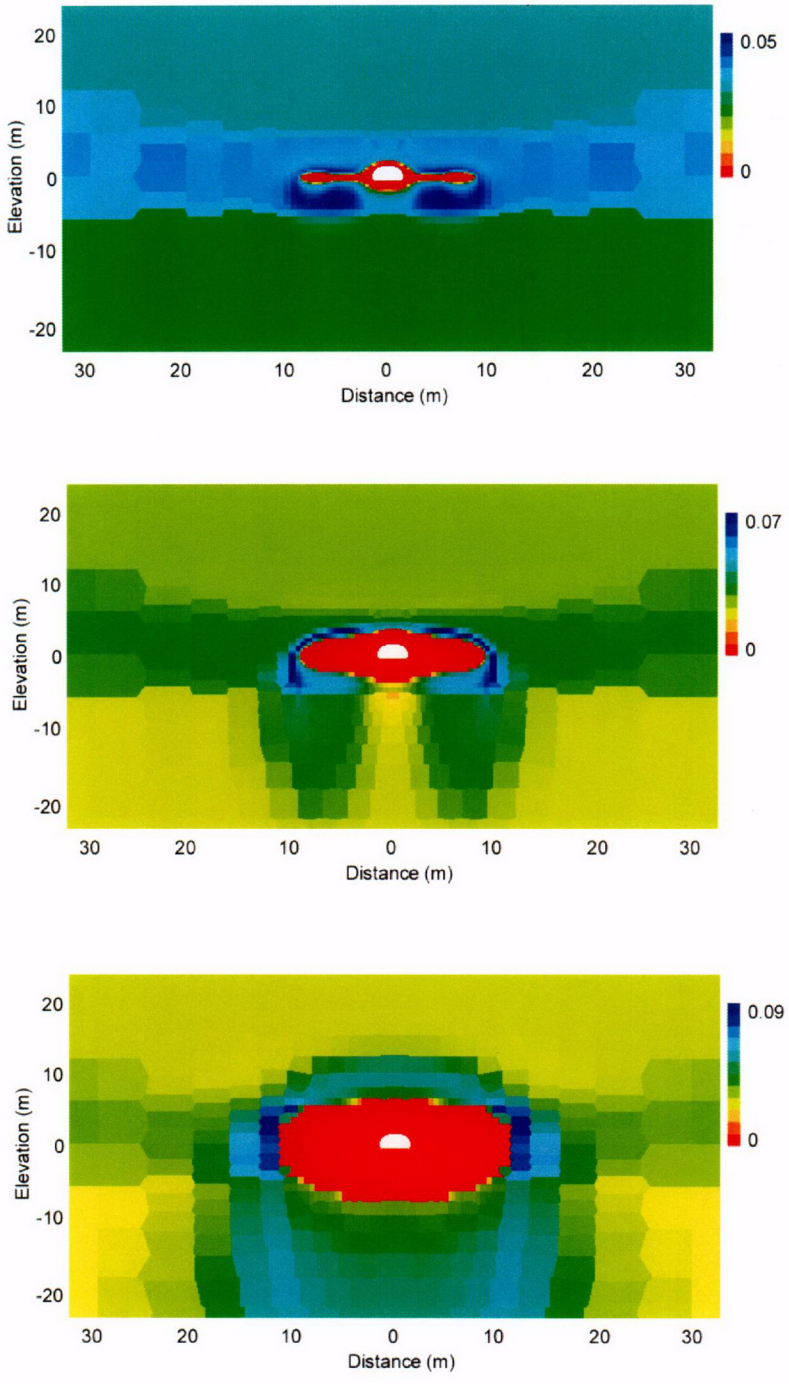

Figure 6-32. Contour Plot of Simulated Fracture Saturation for the Field-Scale Experiment with the Area Modifier A_{mod} = 0.01 (ds126) after 3 Months (Top), 1 Year (Middle), and 4 Years (Bottom) of Heating [1 m = 3.28 ft]

C17

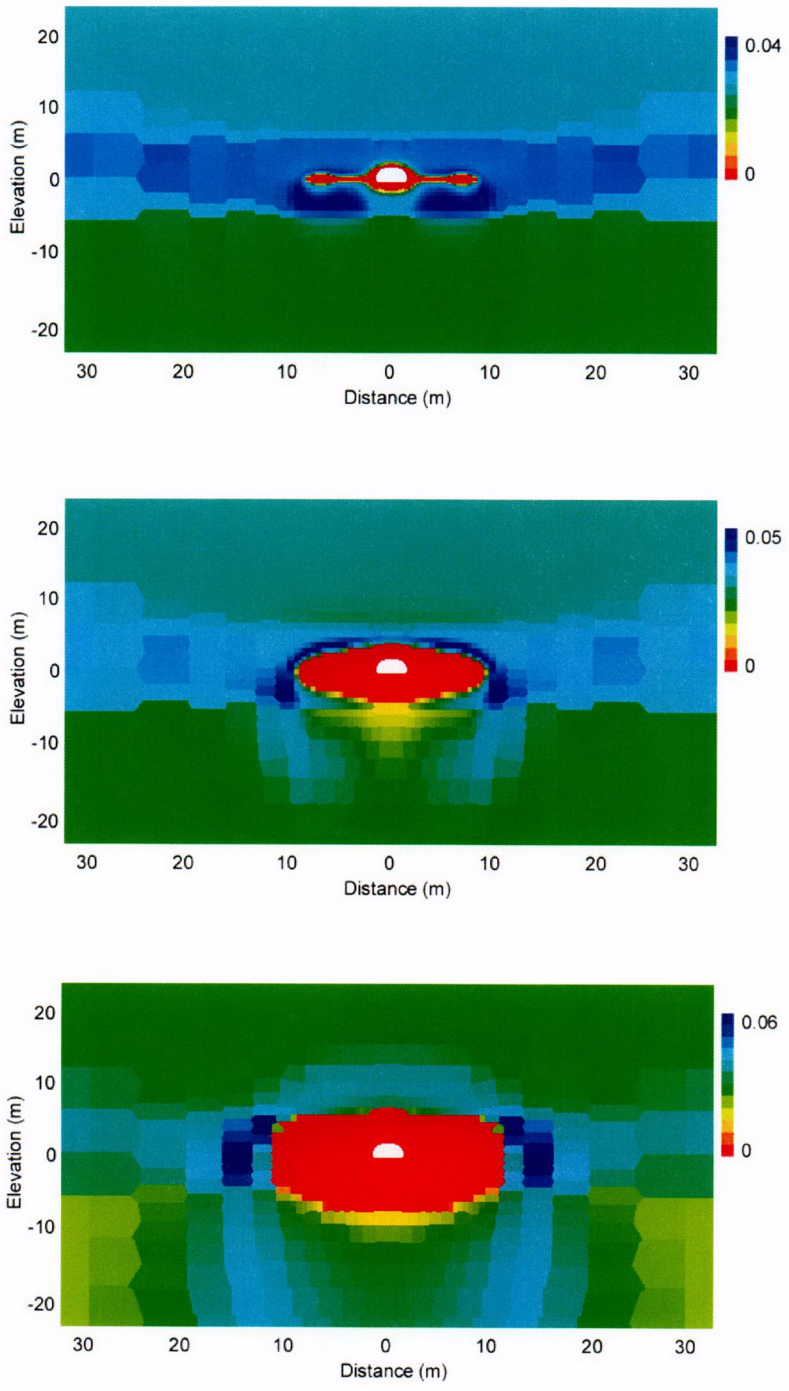

Figure 6-33. Contour Plot of Simulated Fracture Saturation for the Field-Scale Experiment with the Area Modifier A_{mod} = 0.001 (ds127) after 3 Months (Top), 1 Year (Middle), and 4 Years (Bottom) of Heating [1 m = 3.28 ft]

C18

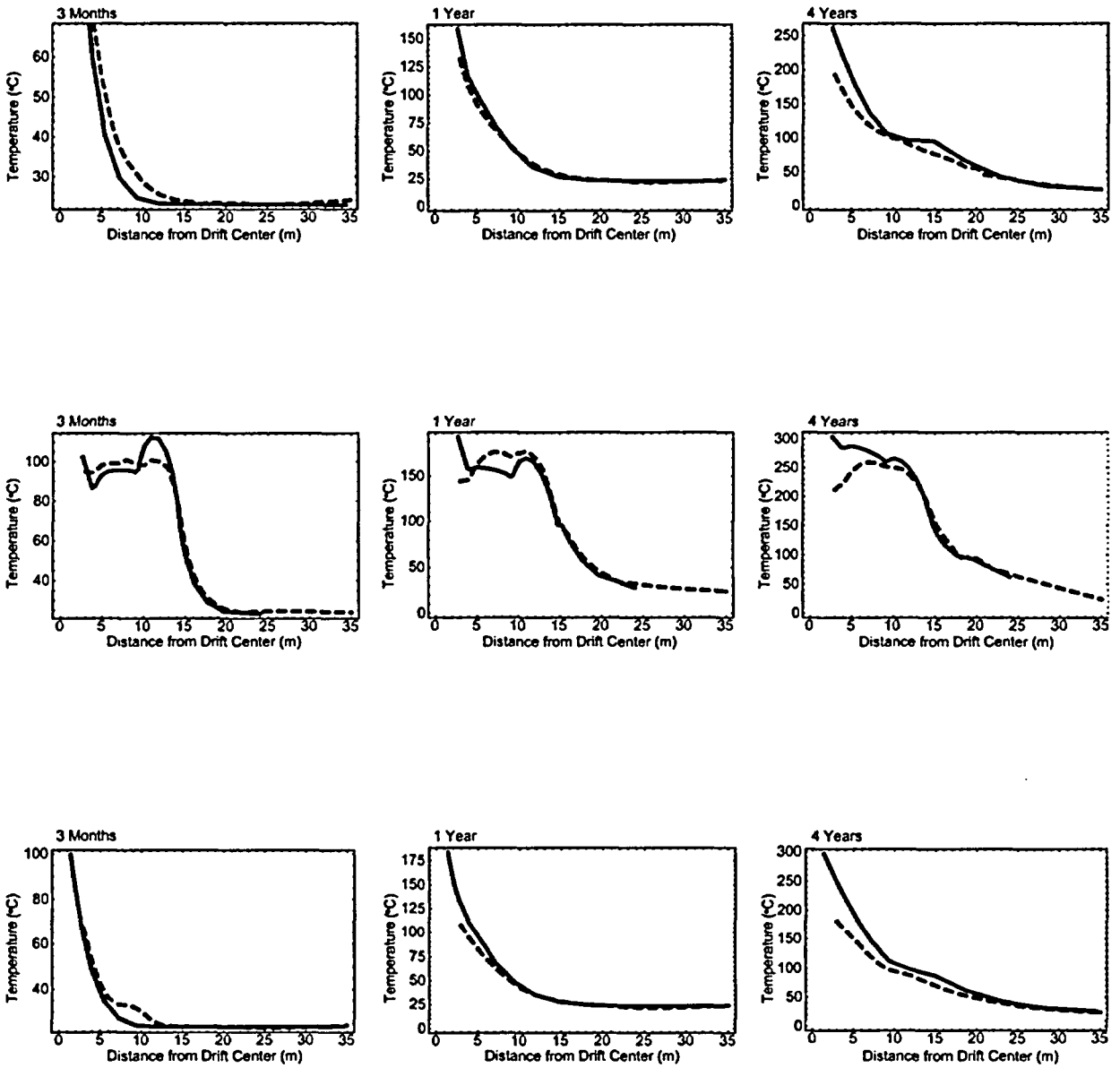

Figure 6-34. Comparison of Measured Temperature Versus Simulated Matrix Temperature at 3 Months (Left), 1 Year (Center), and 4 Years (Right) for Boreholes 158 (Top), 160 (Middle), and 162 (Bottom) for the Basecase (ds108). Temperature Is Provided in °C. [1 m = 3.28 ft]

Loss of heat through the bulkhead at the end of the heated drift was estimated by Wagner[1] to be 6 kW through conduction and radiation and 22 kW through convection. Wagner noted the high level of uncertainty in these estimates is caused by the difficulty in making reasonable measurements. Heat loss through the bulkhead was probably not constant at 28 kW and, in fact, could be quite variable, particularly in view of the complex effects of ventilation modifications in the connecting drift and barometric pumping (Chestnut, et al., 1998). The boundary condition at the drift wall for all these simulations was constant pressure. This boundary condition allowed for the removal of sensible heat from the drift wall, presumably to account for the loss of enthalpy caused by water vapor loss through the bulkhead. This boundary condition, however, did not account for heat loss caused by conduction and radiation. If heat loss by conduction and radiation did, in fact, sum to 6 kW, then the percentage of heat reduction would be 12 percent when the canister heat load was 52 kW, increasing to 16 percent at the end of the test. Inspection of simulations ds110 (10-percent reduction in canister heat load) (Figure 6-35) and ds111 (20-percent reduction in canister heat load) (Figure 6-36) indicate that the canister heat loads are still excessive based on the elevated temperature near the drift wall at all three boreholes. Obviously, removal of more than 6 kW from the canister heat source is required.

Removal of additional heat from the canister yielded a better match with observed temperatures. A 30-percent reduction in the canister heat load equated to 15.6 kW from the initial heat load and 11.4 kW reduction at the end of the test. A reduction of 30 percent of the cannister heat applied to the drift wall (ds112) decreased, but did not eliminate this discrepancy at 4 years of heating (Figure 6-37). Examination of all nine images in Figure 6-35, however, indicates that most main features in the thermal evolution measured at the three boreholes are captured in the simulations. The subtle heat pipes observed below the drift in Borehole 162 and beyond the end of the wing heaters have been reasonably, although not exactly, replicated in simulation ds112 (Figure 6-37). A heat pipe is still simulated above the drift, even though no heat pipe was observed in that region.

None of the modifications included in the other simulations was successful at reducing temperature near the drift to values consistent with those measured. Heat and mass transfer near the heater drift must either be different from that captured by the physics of the simulation, a mechanism for heat removal from the drift during the experiment that is not incorporated in the model, or heat loss by conduction and radiation exceeded the levels estimated by Wagner (CRWMS M&O, 1999c). In addition, discrepancies in temperature that vary in time (i.e., simulated temperatures may have exceeded the observed temperatures at particular locations while the measured temperatures may have exceeded the simulated temperatures at the same locations, but at different times) suggest that the canister heat load varied with time. No attempt was made to replicate these additional transients into the canister heat load applied to the drift wall.

A second discrepancy between observed temperatures and those temperatures predicted by the basecase model was that a heat pipe is simulated above, and, to a lesser degree, below the heated drift at 4 years of heating. The heat pipes are not evidenced in the observed temperatures. No model modification attempted in these analyses, including reduction of

[1]Wagner, R.A. "Assessment of Heat Loss through the Drift-Scale Heater Test Bulkhead." Memorandum (October 21) to M.T. Peters. Las Vegas, Nevada: CRWMS M&O. 1999.

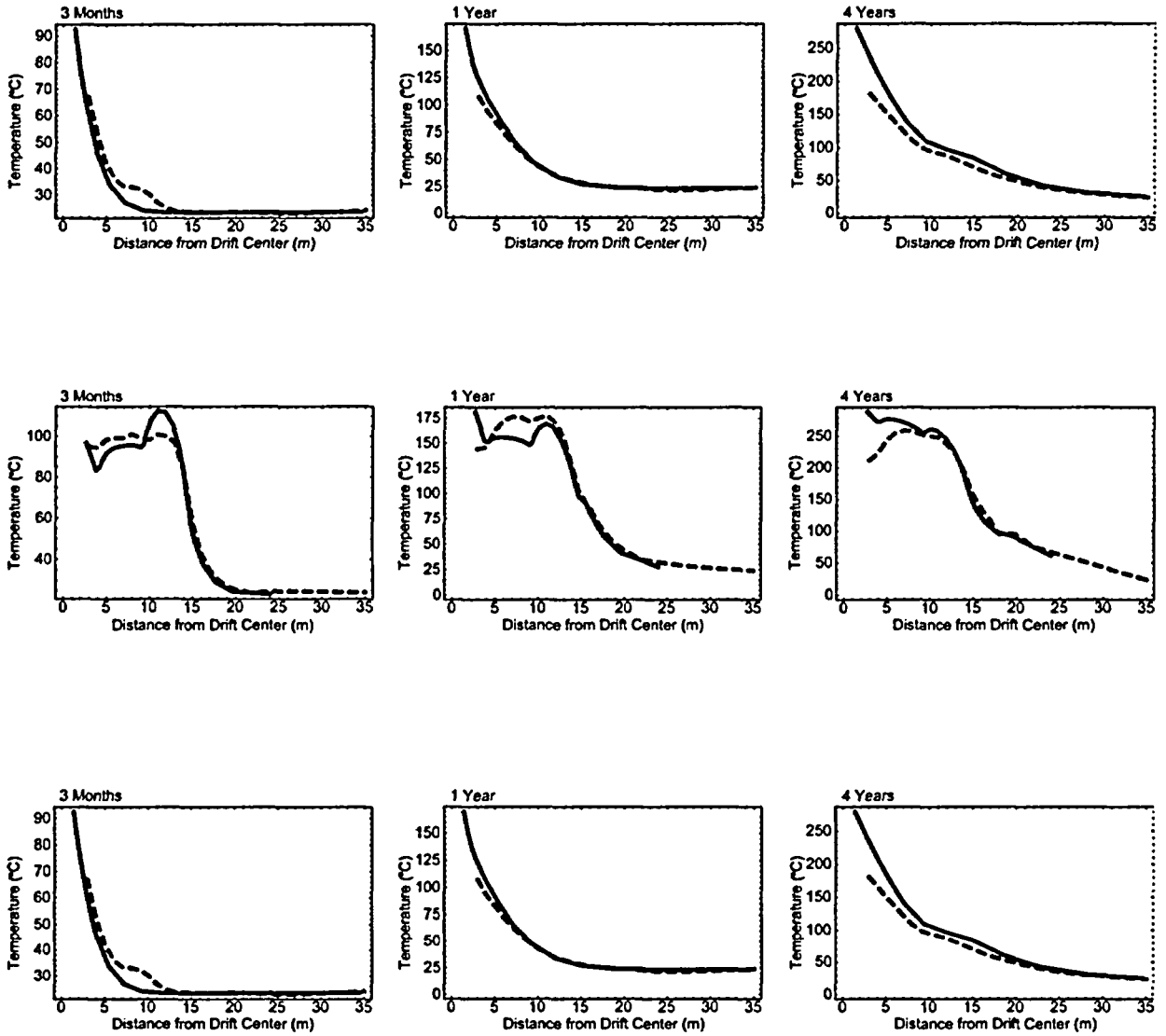

Figure 6-35. Comparison of Measured Temperature Versus Simulated Matrix Temperature at 3 Months (Left), 1 Year (Center), and 4 Years (Right) for Boreholes 158 (Top), 160 (Middle), and 162 (Bottom) with Drift-Wall Heat Load Decreased by 10 Percent (ds110). Temperature Is Provided in °C. [1 m = 3.28 ft]

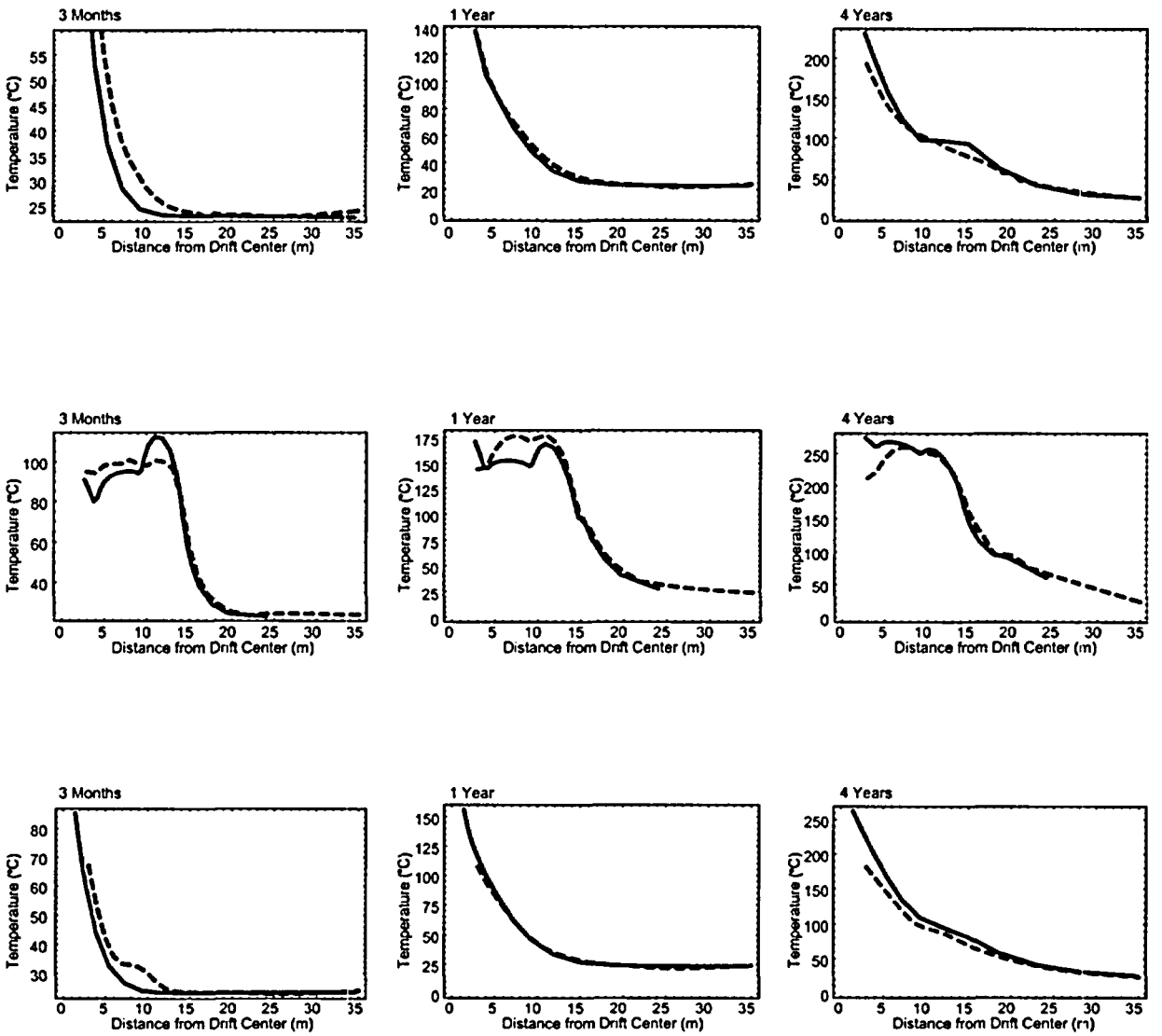

Figure 6-36. Comparison of Measured Temperature Versus Simulated Matrix Temperature at 3 Months (Left), 1 Year (Center), and 4 Years (Right) for Boreholes 158 (Top), 160 (Middle), and 162 (Bottom) with Drift-Wall Heat Load Decreased by 20 Percent (ds111). Temperature Is Provided in °C. [1 m = 3.28 ft]

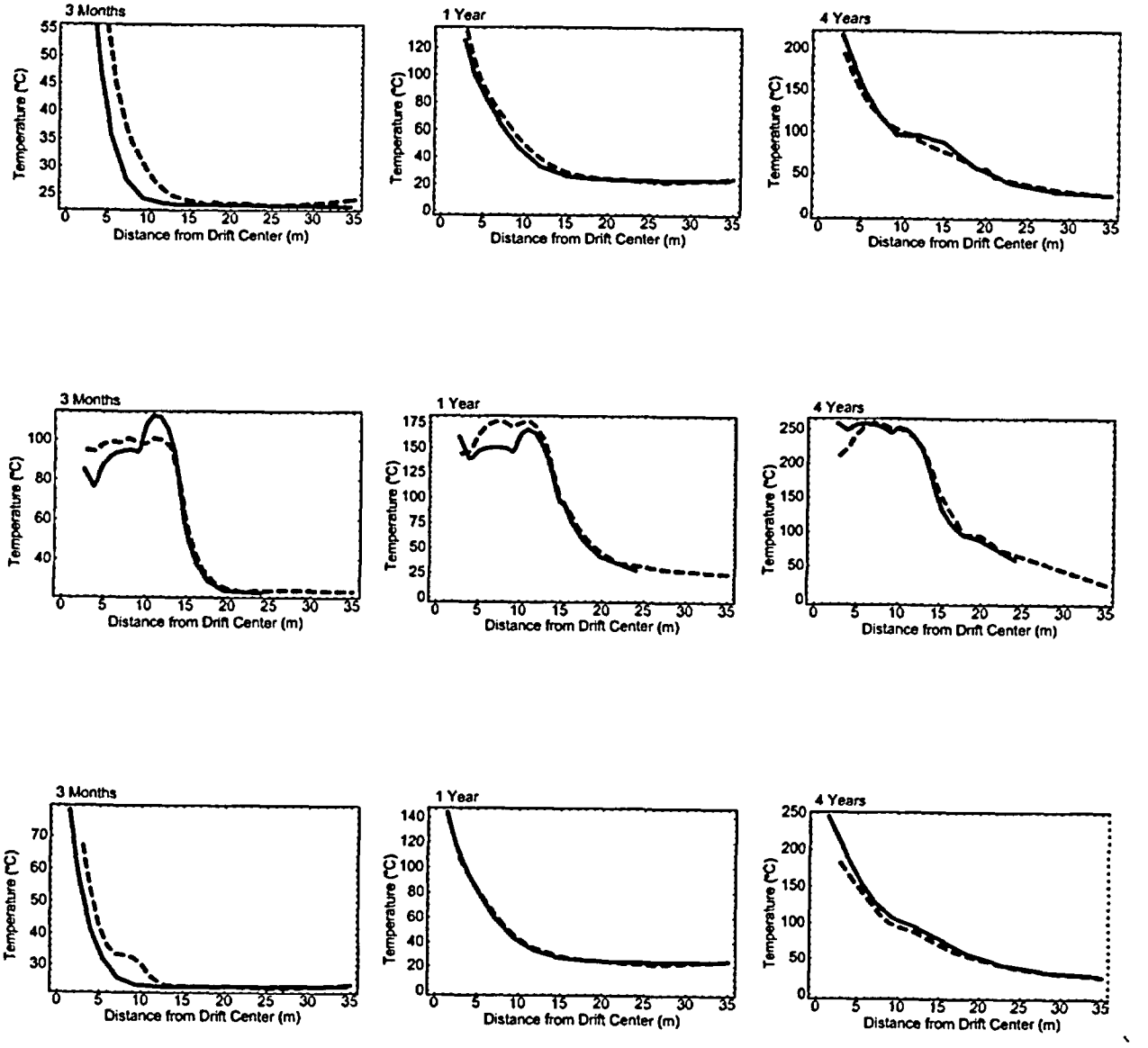

Figure 6-37. Comparison of Measured Temperature Versus Simulated Matrix Temperature at 3 Months (Left), 1 Year (Center), and 4 Years (Right) for Boreholes 158 (Top), 160 (Middle), and 162 (Bottom) with Drift-Wall Heat Load Decreased by 30 Percent (ds112). Temperature Is Provided in °C. [1 m = 3.28 ft]

fracture permeability (ds115) successfully reduced evidence of the heat pipe (Figure 6-38). This result is not fully consistent with earlier analyses (Green and Painter, 2002a,b; Green, et al., 2001) where reductions in fracture permeability were successful in minimizing the presence of heat pipes. A major difference between the earlier analyses and these results is that these simulations predict the formation of a heat pipe at late time (4 years) at a distance of 7 to 15 m [23 to 49 ft] above and 10 to 16 m [33 to 52 ft] below the center of the drift. Previous analyses predicted the formation of a heat pipe at early times (i.e., 1 year), a feature not replicated in the current analyses.

One modification that exacerbated the presence of a heat pipe at late time was the reduction of the area modification factor, A_{mod}, was reduced below 1.0. As illustrated in Figure 6-39 (ds127), an A_{mod} of 0.001 increases the thickness of the heat pipe in the fracture continuum to more than 10 m [33 ft], although the matrix heat pipe effect was essentially removed. Interestingly, this modification removed evidence of a heat pipe from both the matrix and fracture continua below the drift. Removal of the heat pipe from below the drift decreased the simulated temperature at the invert from the basecase simulation of 300 °C [572 °F] to approximately 275 °C [527 °F], still considerably greater than the observed temperature of 180 °C [356 °F].

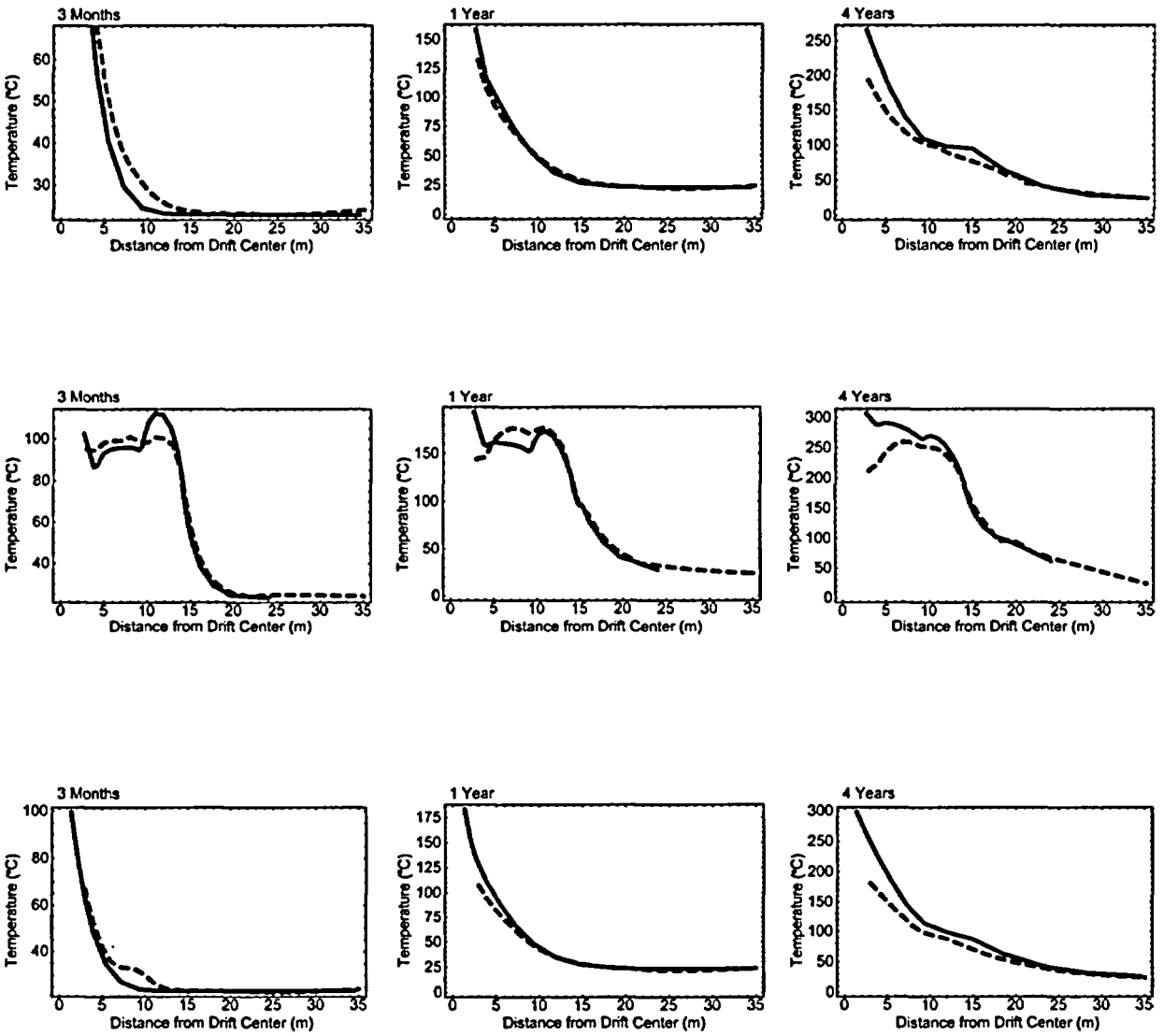

Figure 6-38. Comparison of Measured Temperature Versus Simulated Matrix Temperature at 3 Months (Left), 1 Year (Center), and 4 Years (Right) for Boreholes 158 (Top), 160 (Middle), and 162 (Bottom) with Fracture Permeability Decreased by 10 Times (ds115). Temperature Is Provided in °C. [1 m = 3.28 ft]

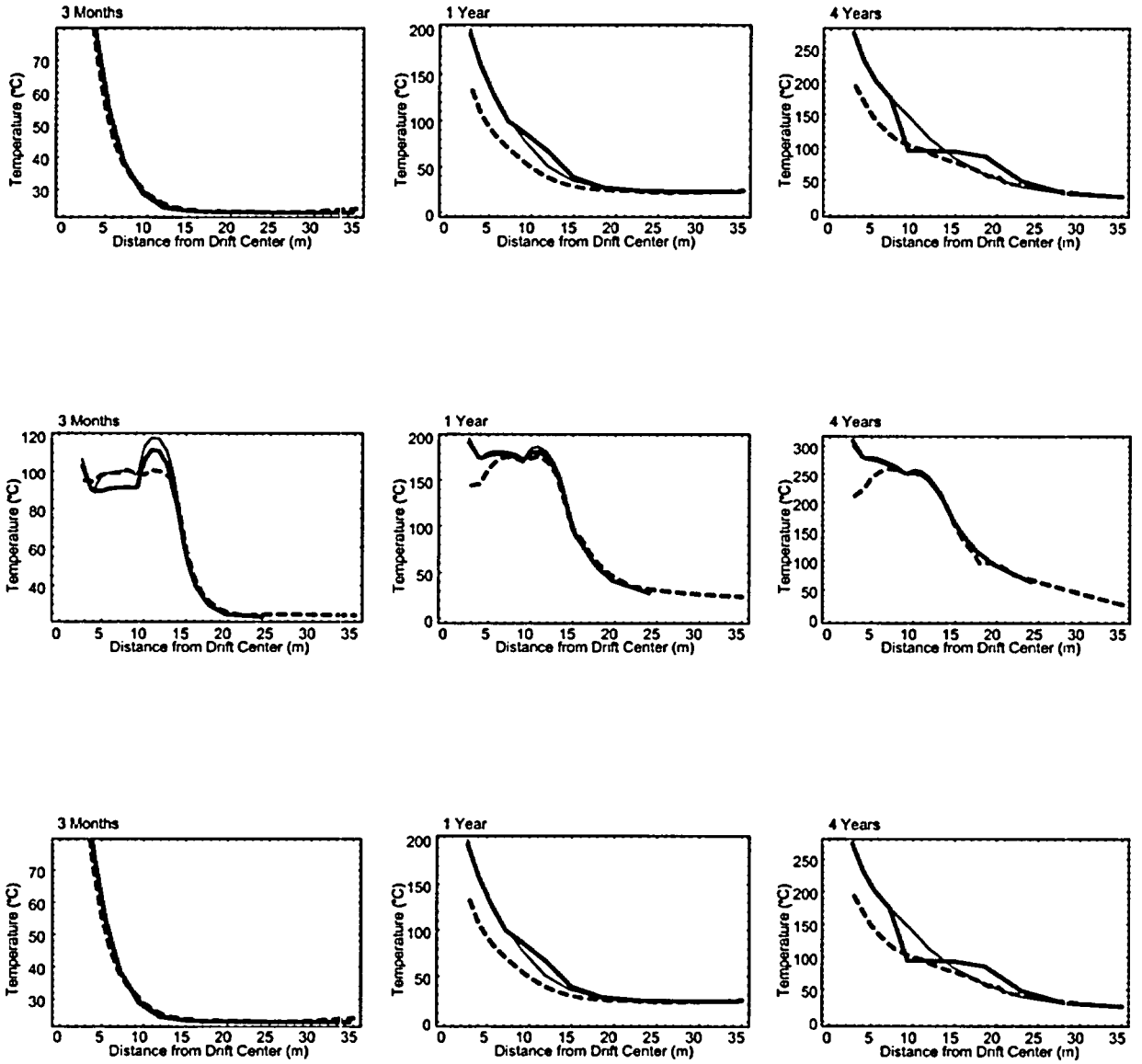

Figure 6-39. Comparison of Measured Temperature Versus Simulated Matrix Temperature at 3 Months (Left), 1 Year (Center), and 4 Years (Right) for Boreholes 158 (Top), 160 (Middle), and 162 (Bottom) with Area Modifier A_{mod} = 0.001 (dsl127). Temperature Is Provided in °C. [1 m = 3.28 ft]

7 DISCUSSION

Modeling is an important part of assessing and developing confidence in the safety case for the proposed geologic repository at Yucca Mountain. Sensitivity analysis results performed on heater experiments conducted at two scales (laboratory and field) provide insights into which properties and conceptual models are most appropriate for representing heat and mass transfer through partially saturated fractured porous media.

7.1 Laboratory-Scale Experiment

The laboratory-scale experiment was, in some ways, better characterized and controlled than the field-scale experiment. For example, the matrix and system of fractures of the laboratory-scale test medium were more uniform and better characterized than the field site. Boundary conditions for the laboratory-scale test were controlled (i.e., infiltration rate was known). However, the limited size of the laboratory-scale test resulted in heat loss through the side walls of the test cell introducing modeling uncertainty. Sensitivity modeling analyses helped evaluate this uncertainty, but complete characterization of the test cell thermal boundary conditions was not possible.

Inspection of the fracture surfaces after the first laboratory-scale test and measurement of the matrix saturation at the conclusion of the second test allowed for greater insight on fluid flow than possible in the field-scale experiment. This information on saturation, when coupled with temperature measurements, provided a broader foundation for comparison than for the field-scale experiment, which relied on geophysical measurements (neutron probe, ground-penetrating radar, and electrical resistivity tomography) for indirect measurement of liquid saturation.

Examination of the results of the laboratory-scale sensitivity analyses indicated that selection of different parameter values and conceptual models captured different features observed during the laboratory-scale experimental results. Key features observed during the laboratory-scale experiment were (i) zones of high matrix saturation above and low matrix saturation below the heated drift at both the mid-plane and the edge plane of the test cell, (ii) focused flow through fracture continuum, and (iii) penetration of fracture flow into the crown of the heated drift. The consensus of simulations of the laboratory-scale experiment indicated that improved simulation of these features was achieved with a smaller van Genuchten α ($1.0 \times 10^{-4}\,Pa^{-1}$), decreased matrix permeability, possible increased fracture permeability, and a reduction in matrix-fracture interactions, although a specific matrix-fracture interaction conceptual model was not clearly identified. A possible exception to this broadly defined model was the successful simulation of decreased saturation below the heated drift, which was replicated in simulations with larger values for the fracture van Genuchten α parameter ($1.0 \times 10^{-3}\,Pa^{-1}$). Some of the best discriminating evidence from the laboratory-scale experiment was the unambiguous zones of increased saturation above and decreased saturation below the heated drift. The models that captured both of these features were (i) active fracture model with large van Genuchten α and matrix permeability decreased by 10 times, (ii) large van Genuchten α with A_{mod} set to 0.001, and (iii) matrix permeability decreased by 10 times.

7.2 Field-Scale Experiment

Temperatures measured during the field-scale experiment provided clearer evidence of the evolution of the thermal-hydrological regime than did indirect measurements of saturation. Only directly measured temperatures were used in these analyses. The basecase consisted of infiltration at 3.0 mm/yr [0.12 in/yr], the active fracture model (Liu, et al., 1998) with $\gamma = 0.41$, and the property values listed in Table 5-2. Based on replication of temperatures measured at three boreholes (158, 160, and 162), the basecase simulation with a canister heat load reduced by 30 percent [ds112 (Figure 6-37)] provided the best match. This simulation did not capture all salient features in the measured temperatures. In particular, simulated temperatures closest to the drift did not reflect all features exhibited in the measured temperatures. Additional adjustment of the canister heat load could reduce these differences. Also, a heat pipe simulated above the drift wall (Borehole 158) at 4 years of heating was not seen in the measured data. Reduction of the heat pipe could be achieved by decreasing the fracture permeability of the simulation that included the 30-percent reduction in drift-wall heat load.

Saturation contour plots for the matrix and fracture continua for simulation ds112 are illustrated in Figures 7-1 and 7-2. The fracture saturation plots indicated that zones of increased saturation form below the outer wing heaters at 3 months. By 1 year of heating, these zones increased in size and were found both above and below the wing heaters and a prominent dryout zone had developed, encompassing the combined drift-wing heater region. In addition, a prominent zone of increased fracture saturation had formed beneath the full footprint of the field-scale experiment at 1 year of heating.

The dryout zone thickness in the fracture continuum illustrated in Figure 7-2 approached 13 m [42.6 ft] at the end of the 4-year heating phase. The zone of greatest fracture saturation was slightly diminished in extent at this time, appearing mostly near the ends of the wing heaters, although the thickness of these increased saturation zones increased. These results suggest that increased saturation would be available for fracture flow near the edges of the boiling isotherm and the dryout zones. This tendency could become important if the increased fracture saturation led to focused seepage into emplacement drifts, possibly resulting in an environment that enhanced corrosion by causing increased relative humidity and liquid saturation.

7.3 General Conclusions

General observations can be drawn from the ensemble of the sensitivity analyses of the two experiments conducted at different scales. The laboratory-scale analyses highlight the importance of assigning appropriate property values to several key parameters: matrix permeability, the van Genuchten α (related to the air-entry value), and, most importantly, fracture permeability. The choice of conceptual model for matrix-fracture interactions had an important effect on evolution of temperature and saturation in the laboratory-scale test; however, all three choices for conceptual models had some success in capturing key features observed during the tests. Analyses of the field-scale test provided greater insight on the choice of the matrix-fracture interaction conceptual model. Replication of temperatures measured at three boreholes was most successful when the active fracture conceptual model was selected. Finally, both sets of sensitivity analyses confirmed that partial success, in terms of agreement between selected observations and model results, could be achieved for almost any choice of property values or conceptual model. It is important to compare the model results

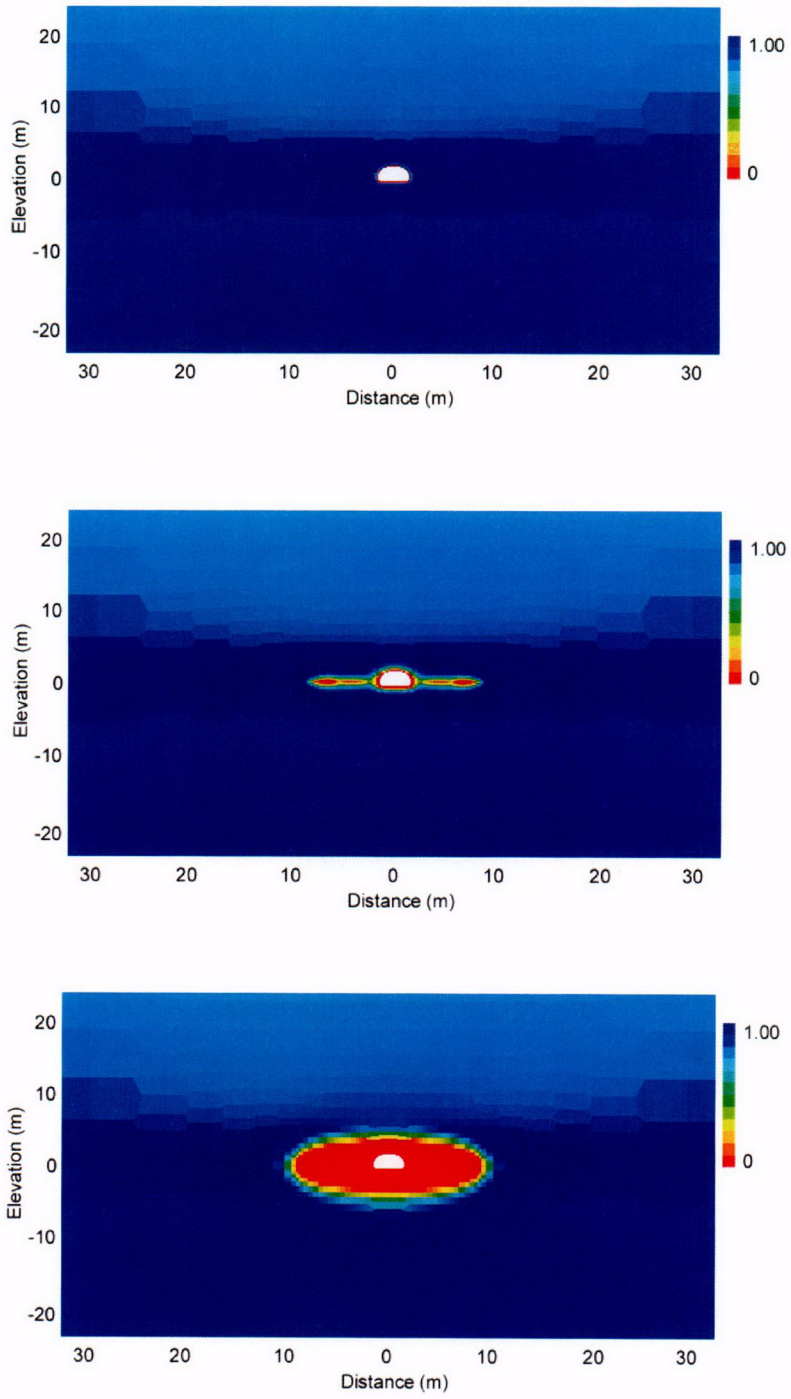

Figure 7-1. Contour Plots of Simulated Matrix Saturation at 3 Months (Top), 1 Year (Middle), and 4 Year (Bottom) for the Basecase with Drift-Wall Heat Load Decreased by 30 Percent (ds112) [1 m = 3.28 ft]

C19

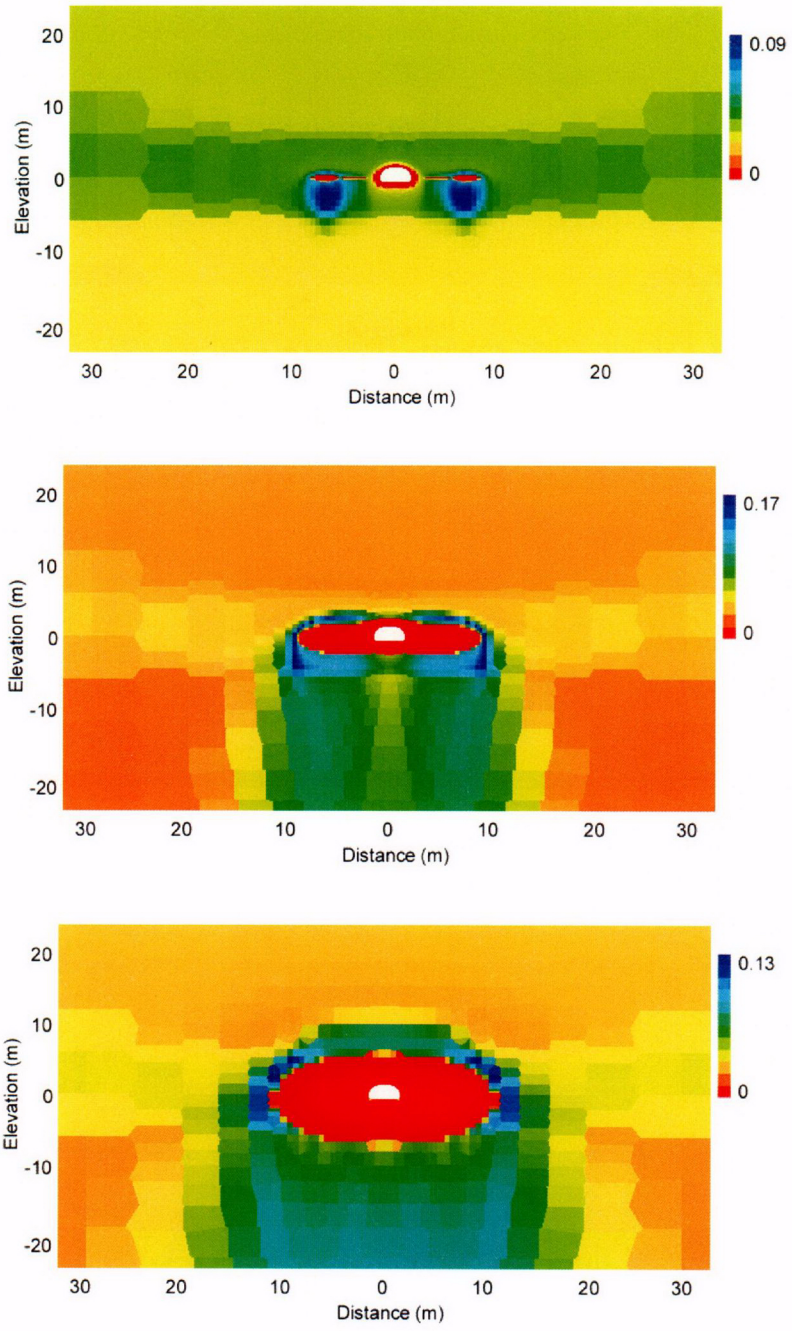

Figure 7-2. Contour Plots of Simulated Fracture Saturation at 3 Months (Top), 1 Year (Middle), and 4 Years (Bottom) for the Basecase with Drift-Wall Heat Load Decreased by 30 Percent (ds112) [1 m = 3.28 ft]

CZO

with the complete suite of experimental results to determine the true merit of the values and conceptual models selected for representative multiphase models.

7.4 Future Analyses

Results documented in this status report include a broad range of conceptual models for matrix-fracture interactions and property assignments. Further enhancements to the matrix-fracture conceptual models will help clarify this challenging technical area, particularly in the presence of heat sources and large variations in fracture saturations. Results from the cooling phase of the Drift-Scale Heater Test will provide additional basis to evaluate the appropriateness of the conceptual models and property value assignments. Results presented in this report can serve as a foundation for these anticipated analyses.

8 REFERENCES

Birkholzer, J.T. and Y.W. Tsang. "Modeling the Thermal-Hydrologic Processes in a Large-Scale Underground Heater Test in Partially Saturated Fractured Tuff." *Water Resources Research.* Vol. 36, No. 6. pp. 1,431–1,447. 2000.

Birkholzer, J.T. and Y.W. Tsang. "Pretest Analysis of the Thermal-Hydrological Conditions of the Exploratory Studies Facility Drift-Scale Test." Earth Sciences Division Level 4 Milestone Report SP9322M4. Berkeley, California: Lawrence Berkeley National Laboratory. 1997.

Blair, S., T. Buscheck, L. DeLoach, W. Lin, and A. Ramirez. "Single Heater Test Final Report." UCRL–ID–131491. Livermore, California: Lawrence Livermore National Laboratory. 1998.

Bodvarsson, G.S., T.M. Bandurraga, and Y.S. Wu, eds. "The Site-Scale Unsaturated Zone Model of Yucca Mountain, Nevada, for the Viability Assessment." LBNL–40376. Berkeley, California: Lawrence Berkeley National Laboratory. 1997.

Brechtel, C.E., G. Lin, E. Martin, and D.S. Kessel. "Geochemical Characterization of the North Ramp of the Exploratory Studies Area." SAND95–0488. Albuquerque, New Mexico: Sandia National Laboratories. 1995.

Brooks, R.H. and A.T. Corey. "Properties of Porous Media Affecting Fluid Flow." *Journal of Irrigation and Drainage Engineering.* Vol. 92. pp. 61–88. 1966.

Chestnut, D.A., M.J. Peters, T.A. Buscheck, and R.N. Datta. "Relative Humidity Response to Barometric Pressure Change in an Underground Heated Drift at Yucca Mountain." Geological Society of America Abstract with Programs—1998 Annual Meeting. Boulder, Colorado: Geological Society of America. p. A–362. 1998.

CRWMS M&O. "Analysis of Hydrologic Properties." ANL–NBS–HS–000002. Rev. 00. Las Vegas, Nevada: CRWMS M&O. 2000a

———. "Calibrated Properties Model." MDL–NBS–HS–000003. Rev. 00. Las Vegas, Nevada: CRWMS M&O. 2000b.

———. "Thermal Tests Thermal-Hydrological Analyses/Model Report." ANL–NBS–TH–000001. Rev. 00 ICN 01. Las Vegas, Nevada: CRWMS M&O. 2000c.

———. "Thermal Test Progress Report #4." Las Vegas, Nevada: CRWMS M&O. 1999a.

———. "Thermal Test Progress Report #3." Las Vegas, Nevada: CRWMS M&O. 1999b.

———. "Total System Performance Assessment—Viability Assessment (TSPA-VA) Analyses Technical Basis Document." B00000000–01717–4301–00001. Rev. 01. Las Vegas, Nevada: TRW Environmental Safety Systems, Inc. 1998a.

———. "Thermal Test Progress Report #1." Las Vegas, Nevada: CRWMS M&O. 1998b.

———. "Thermal Test Progress Report #2." Las Vegas, Nevada: CRWMS M&O. 1998c.

———. "Drift-Scale Test As-Built Report." BAB00000–01717–5700–0003. Rev. 01. Las Vegas, Nevada: CRWMS M&O. 1998d.

———. "Ambient Characterization of the Drift-Scale Test Block." DD00000–01717–5705–00001. Rev. 01. Las Vegas, Nevada: CRWMS M&O. 1997a.

———. "Drift-Scale Test Design and Forecast Results." B00000000–01717–4600–00007. Rev. 00. Las Vegas, Nevada: CRWMS M&O. 1997b.

Green, R.T. and S. Painter. "Final Report for DECOVALEX III Task 2A: Numerical Simulation of the Drift-Scale Heater Test at Yucca Mountain." San Antonio, Texas: CNWRA. 2002a.

Green, R.T. and S. Painter. "Status Report for Numerical Simulation of the Drift-Scale Heater Test at Yucca Mountain." San Antonio, Texas: CNWRA. 2002b.

Green, R.T., M.E. Hill, and S. Painter. "Progress Report for DECOVALEX III Task 2: Numerical Simulation of the Drift-Scale Heater Test at Yucca Mountain." San Antonio, Texas: CNWRA. 2001.

Green, R.T., F.T. Dodge, S.J. Svedeman, R.D. Manteufel, G. Rice, K.A. Meyer, and R.G. Baca. NUREG/CR–6348, "Thermally Driven Moisture Redistribution in Partially Saturated Porous Media." Washington DC: NRC. 1995.

Klavetter, E.A. and R.R. Peters. "Estimation of Hydrologic Properties of an Unsaturated, Fractured Rock Mass." SAND84–2642. Albuquerque, New Mexico: Sandia National Laboratories. 1986.

Lichtner, P.C. and M.S. Seth. "Multiphase-Multicomponent Nonisothermal Reactive Transport in Partially Saturated Porous Media." Proceedings of the International Conference on Deep Geological Disposal of Radioactive Waste, Winnipeg, Manitoba, Canada, September 16–19, 1996. Toronto, Ontario, Canada: Canadian Nuclear Society. pp. 133–142. 1996.

Liu, H.H., C. Doughty, and G.S. Bodvarsson. "An Active Fracture Model for Unsaturated Flow and Transport in Fractured Rock." *Water Resources Research.* Vol. 34, No. 10. pp. 2,633–2,646. 1998.

Mualem, Y. "A New Model for Predicting Hydraulic Conductivity of Unsaturated Porous Media." *Water Resources Research.* Vol. 12. pp. 513–522. 1976.

Nitao, J. "Reference Manual for the NUFT Flow and Transport Code. Version 2.0." UCRL–MA–130651. Livermore, California: Livermore National Laboratory. 1998.

NRC. NUREG–1762, "Integrated Issue Resolution Status Report." Washington, DC: NRC. July 2002.

Painter, S., P.C. Lichtner, and M.S. Seth. "MULTIFLO User's Manual." MULTIFLO, Version 1.5: Two-Phase Nonisothermal Coupled Thermal-Hydrologic-Chemical Flow Simulator. Rev. 3. San Antonio, Texas: CNWRA. 2001.

Phillips, O.M. "Infiltration of a Liquid Finger Down a Fracture into Superheated Rock." *Water Resources Research.* Vol. 32, No. 6. pp. 1665–1670. 1996.

Pruess, K. and T.N. Narasimhan. "A Practical Method for Modeling Fluid and Heat Flow in Fractured Porous Media." *Society of Petroleum Engineers Journal.* Vol. 25, No. 1. pp. 14–26. 1985.

Pruess, K., C. Oldenburg, and G. Moridis. "TOUGH2 User's Guide. Version 2.0." LBNL–43134. Berkeley, California: Lawrence Berkeley National Laboratory. 1999.

Tsang, Y.W. and J.T. Birkholzer. "Predictions and Observations of the Thermal-Hydrological Conditions in the Single Heater Test." *Journal of Contaminant Hydrology.* Vol. 38. pp. 385–425. 1999.

Tsang, Y.W., J. Apps, J.T. Birkholzer, B. Freifeld, M.Q. Hu, J. Peterson, E. Sonnenthal, and N. Spycher. "Yucca Mountain Single Heater Test Final Report." LBNL–42537. Berkeley, California: Lawrence Berkeley National Laboratory. 1999.

van der Kwaak, J.E., P.A. Forsyth, K.T.B. MacQuanie, and E.A. Sudicky. "WATSOLV, Sparse Matrix Iterative Solver Package, User's Guide." Waterloo, Ontario, Canada: Waterloo Centre for Groundwater Research, University of Waterloo. 1995.

van Genuchten, M.Th. "A Closed-Form Equation for Predicting the Hydraulic Conductivity of Unsaturated Soils." *Soil Science Society of American Journal.* Vol. 44. pp. 892–898. 1980.

Wilder, D.G., W. Lin, S.C. Blair, T. Buscheck, R.C. Carlson, K. Lee, A. Meike, A.L. Ramirez, J. L. Wagoner, and J. Wang. "Large Block Test Status Report." UCRL–ID–128776. Livermore, California: Lawrence Livermore National Laboratory. 1998.

Zyvoloski, G.A., B.A. Robinson, Z.V. Dash, and L.L. Trease. "Users Manual for the FEHM Application—A Finite-Element Heat- and Mass-Transfer Code." LA–13306–M. Los Alamos, New Mexico: Los Alamos National Laboratory. 1999.

APPENDIX A: Simulated matrix temperature for the laboratory-scale heater test in a vertical plane oriented perpendicular to the heated drift (left figure) and in a vertical plane oriented parallel to the heated drift (right figure). Only one-half the test cell is illustrated in the figures.

APPENDIX B

APPENDIX B: Simulated matrix saturation for the laboratory-scale heater test at the vertical mid-plane (left figure) and vertical plane at the edge (right figure) perpendicular to the heated drift. Only one-half the test cell is illustrated in the figures.

APPENDIX C

APPENDIX C: Simulated fracture saturation for the laboratory-scale heater test in four parallel vertical planes oriented perpendicular to the heated drift (left figure) and in a vertical plane oriented parallel to the heated drift (right figure) for simulations lst155 (top), lst156 (middle), and lst157 (bottom). The planes are located 0.01, 0.15, 0.23, and 0.25 m [0.033, 0.49, 0.75, and 0.82 ft] from the middle of the 0.30-m [1.0-ft] wide test cell. Only one-half the test cell is illustrated in the figures.

APPENDIX D

APPENDIX D: Contour plots of simulated matrix temperature for simulations for the field-scale Drift-Scale Heater Test after 3 months, 1 year, and 4 years of heating.

APPENDIX E

APPENDIX E: Contour plots of simulated matrix saturation for the field-scale Drift-Scale Heater Test for simulations for the field-scale Drift-Scale Heater Test after 3 months, 1 year, and 4 years of heating.

APPENDIX F

APPENDIX F: Contour plots of simulated fracture saturation for the field-scale Drift-Scale Heater Test for simulations after 3 months, 1 year, and 4 years of heating.

APPENDIX G

APPENDIX G: Graphs of simulated temperature for the field-scale Drift-Scale Heater Test. Each directory contains nine images. Simulated temperature is plotted versus measured temperature along three boreholes (158, vertical upward; 160, horizontal; and 162, vertical downward) at 3 times (3 months, 1 year, and 4 years after the onset of heating).